CAPITAL UNIVERSITY OF SCIENCE AND TECHNOLOGY, ISLAMABAD

Efficient Transmission of Giga-Watt Microwave Signal Using S-Band Slotted Waveguide Array Antenna

by

Asif Mehmood Khan

A dissertation submitted in partial fulfillment for the degree of Doctor of Philosophy

in the

Faculty of Engineering
Department of Electrical Engineering

2023

Efficient Transmission of Giga-Watt Microwave Signal Using S-Band Slotted Waveguide Array Antenna

By

Asif Mehmood Khan

(DEE151008)

Dr. Ian Robertson, Professor

University of Leeds, UK

(Foreign Evaluator 1)

Dr. Muhammad Arif Khan, Senior Lecturer

Charles Sturt University, Australia

(Foreign Evaluator 2)

Dr. Muhammad Mansoor Ahmed

(Research Supervisor)

Dr. Noor Muhammad Khan

(Head, Department of Electrical Engineering)

Dr. Imtiaz Ahmad Taj

(Dean, Faculty of Engineering)

DEPARTMENT OF ELECTRICAL ENGINEERING

CAPITAL UNIVERSITY OF SCIENCE AND TECHNOLOGY

ISLAMABAD

2023

Dedicated to my family

CAPITAL UNIVERSITY OF SCIENCE & TECHNOLOGY
ISLAMABAD

Expressway, Kahuta Road, Zone-V, Islamabad
Phone:+92-51-111-555-666 Fax: +92-51-4486705
Email: info@cust.edu.pk Website: https://www.cust.edu.pk

CERTIFICATE OF APPROVAL

This is to certify that the research work presented in the dissertation, entitled "**Efficient Transmission of Giga-Watt Microwave Signal Using S-Band Slotted Waveguide Array Antenna**" was conducted under the supervision of **Dr. Muhammad Mansoor Ahmed**. No part of this dissertation has been submitted anywhere else for any other degree. This dissertation is submitted to the **Department of Electrical Engineering, Capital University of Science and Technology** in partial fulfillment of the requirements for the degree of Doctor in Philosophy in the field of **Electrical Engineering.** The open defence of the dissertation was conducted on **October 13, 2023**.

Student Name : Asif Mehmood Khan (DEE151008)

The Examination Committee unanimously agrees to award PhD degree in the mentioned field.

Examination Committee :

(a) External Examiner 1: Dr. Junaid Mughal
Professor
CUI, Attock Campus

(b) External Examiner 2: Dr. Qaisar Abbas Naqvi
Professor
QAU, Islamabad

(c) Internal Examiner : Dr. Muhammad Riaz
Associate Professor
CUST, Islamabad

Supervisor Name : Dr. Muhammad Mansoor Ahmed
Professor
CUST, Islamabad

Name of HoD : Dr. Noor Muhammad Khan
Professor
CUST, Islamabad

Name of Dean : Dr. Imtiaz Ahmad Taj
Professor
CUST, Islamabad

AUTHOR'S DECLARATION

I, **Asif Mehmood Khan (Registration No. DEE151008)**, hereby state that my dissertation titled, "**Efficient Transmission of Giga-Watt Microwave Signal Using S-Band Slotted Waveguide Array Antenna**" is my own work and has not been submitted previously by me for taking any degree from Capital University of Science and Technology, Islamabad or anywhere else in the country/ world.

At any time, if my statement is found to be incorrect even after my graduation, the University has the right to withdraw my PhD Degree.

(Asif Mehmood Khan)

Dated: 13 October, 2023

Registration No : DEE151008

PLAGIARISM UNDERTAKING

I solemnly declare that research work presented in the dissertation titled "**Efficient Transmission of Giga-Watt Microwave Signal Using S-Band Slotted Waveguide Array Antenna**" is solely my research work with no significant contribution from any other person. Small contribution/ help wherever taken has been duly acknowledged and that complete dissertation has been written by me.

I understand the zero-tolerance policy of the HEC and Capital University of Science and Technology towards plagiarism. Therefore, I as an author of the above titled dissertation declare that no portion of my dissertation has been plagiarized and any material used as reference is properly referred/ cited.

I undertake that if I am found guilty of any formal plagiarism in the above titled dissertation even after award of PhD Degree, the University reserves the right to withdraw/ revoke my PhD degree and that HEC and the University have the right to publish my name on the HEC/ University Website on which names of students are placed who submitted plagiarized dissertation.

(**Asif Mehmood Khan**)

Dated: 13 October, 2023

Registration No : DEE151008

List of Publications

It is certified that following publication(s) have been made out of the research work that has been carried out for this dissertation:-

1. **A.M. Khan**, M.M. Ahmed, and U. Rafique, "Experimental Study of RF–Plasma Interaction Using a Low-Pressure DC Glow Discharge Tube for MPC," *Electronics*, vol. 12, no.3, pp. 551, 2023.

2. **A.M. Khan**, M.M. Ahmed, U. Rafique, A. Kiyani, and S.M. Abbas "An Efficient Slotted Waveguide Antenna System Integrated with Inside-Grooves and Modified Gaussian Slot Distribution," *Electronics*, vol. 11, no.18, pp. 2948, 2022.

3. **A.M. Khan**, M.M. Ahmed, U. Rafique, and S. Khan "Design, Analysis and Fabrication of an Inside-Grooved Slotted Waveguide Array Antenna for HP Applications," *IEEE Access*, vol. 11, pp. 50116-50129, 2023.

(Asif Mehmood Khan)
Registration No: DEE151008

Acknowledgement

All praise to **Almighty ALLAH**, the Most Gracious, and the Most Merciful for His blessing given to me during my study and in completing my Phd dissertation.

I would like to express my heartiest gratitude to my supervisor **Prof. Dr. Muhammad Mansoor Ahmed**, Vice Chancellor, Capital University of Science and Technology (CUST). It was a wonderful experience and learning opportunity to work with him as a PhD student. He supported me in every step of my studies in topic selection, experimental work, paper publications and dissertation writing. They also provided positive encouragement, knowledge and a warm spirit to complete my research objectives.

I am thankful to the administration of CUST for providing me with an excellent environment perfect for conducting my research. I would like to thank the Dean, Faculty of Engineering, **Prof. Dr. Imtiaz Ahmad Taj**, and Head of Electrical Engineering Department, **Prof. Dr. Noor M. Khan** for their continuous encouragement and support during the entire span of my studies at CUST.

Furthermore, I would also like to express my sincere gratitude to all the members of **Microelectronics and RF Engineering** research group, especially **Mr. Umair Rafique** and **Mr. Suleman Khan** for their kind support.

Finally, I would like to express my feelings of gratitude to my parents, family and friends for their exceptional love and encouragement throughout of my life and eventually to achieve my goals that would not have been possible without their sincere co-operation and love.

(Asif Mehmood Khan)

Abstract

In this dissertation, the design and fabrication of an S-band slotted waveguide array antenna (SWAA) was discussed for high-power microwave applications. The aim of this research is to obtain high peak power microwave radiations and their efficient transmission using low power electrical and RF input systems. Microwave Pulse Compression (MPC) techniques have been used which consist of an RF polarizer, a spherical cavity and a gas-based plasma switch. In the past, the Klystron device was commonly used in MPC as phase inversion can easily be achieved by using a low-power phase shifter on the input side of the Klystron to discharge the cavity. The major problem for using a magnetron device as an input for MPC is the rapid phase inversion at a particular instant which is resolved by using a plasma gas switch in an RF polarizer. In addition, different cavity designs have been studied to further improve storage time. The MPC cold test is in good agreement with the simulation results.

After achieving high peak power using MPC, the signal was transmitted using a slotted waveguide antenna. To this purpose, an efficient SWAA with feed networks has been designed, fabricated and tested. The single element of the array consists of ten Gaussian distributed slots on the broad-side wall of the waveguide, embedded with interior grooves. A 4-element SWAA configuration is designed to achieve relatively high gain (24.6 dB) with highly isolated radiating elements (-24 dB). Gain enhancement and mutual coupling (MC) reduction are achieved by optimizing the inside-grooved regions. A 1×4 power divider (PD) of identical phase and amplitude (-6 dB) at its output ports is designed to supply the elements of the array. SWAA's radiation performance is further enhanced by developing a dielectric radome. The radiation performance of SWAA is further improved by developing a dielectric radome.

The proposed design having dimensions $8.46\lambda_0 \times 4.3\lambda_0 \times 1.47\lambda_0$ provides return loss (RL) better than -25 dB with side level lobe (SLL) of -15 dB and -20 dB in the E and H planes, respectively, and a power handling capacity of more than 1.0 GW. It has been demonstrated that the developed system, due to the effective

suppression of the unwanted surface current, allows an efficient beam scanning without causing a significant reduction in its gain. The measured results of the developed design are in good agreement with the simulation results and found to be the most suitable for HPM systems.

Contents

List of Figures

List of Tables

Abbreviations

1D	One Dimensional
3D	Three Dimensional
ADS	Active Denial System
AMC	Artificial Magnetic Conductor
BOC	Barrel type Open Cavity
BWO	Backward Wave Oscillator
CA-RLSA	Concentric Array Radial Line Slot Antenna
DC	Direct Current
DNG	Double Negative
EBG	Electromagnetic Band Gap
EM	Electromagnetic
FPRC	Fabry Parot Resonating Cavity
FSS	Frequency Selective Surface
GW	Giga Watt
HDPE	High Density Polyehtylene
HPBW	Half Power Beam-width
HPM	High Power Microwave
ID	Inside Diameter
IG	Inside Groove
MC	Mutual Coupling
MGD	Modified Gaussian Slot Distribution
MILO	Magnetically Insulated Line Oscillator
MPC	Microwave Pulse Compressor

MTM	Metamaterial
MW	Mega Watt
NRI	Negative Reference Index
OD	Outside Diameter
PD	Power Divider
PEC	Perfect Electric Conductor
PPS	Progressive Phase Shift
PRS	Partially Reflecting Surface
RA	Roughness Average
RADAR	Radio Detection And Ranging
RF	Radio Frequency
SLED	SLAC Energy Doubler
SLL	Side Lobe Level
SRR	Split Ring Resonator
SWA	Slotted Waveguide Antenna
SWAA	Slotted Waveguide Antenna Array
TE	Transverse Electric
TM	Transverse Magnetic
TWTA	Travelling Wave Tube Amplifier
UAV	Unmanned areal vehicle
VCO	Voltage Controlled Oscillator
VED	Vacuum Electron Device
VNA	Vector Network Analyzer

Symbols

Ar	Argon
a	Width of waveguide
c	Speed of Light
c_n	Beam Distribution Coefficient
E_0	Maximum E field intensity
E_{AB}	Air breakdown field
E_{GB}	Waveguide breakdown field
$E_{(Bd)}$	Vacuum breakdown threshold
F_r	Spherical Bessel Function
f_0	Central frequency
f_c	Frequency of Collision
f_p	Plasma frequency
G	Gain
g_m	Normalized Conductance
h	Height of the dielectric enclosure
k_B	Boltzmann constant
m_e	Mass of electron
N_e	Electron density
n_e	Number of ionized particles
O_2	Oxygen
P_A	Aperture power
P_{in}	Input power
P_R	Power handling capacity

q	Charge of electron
R	Radius of the circular coupler
S_A	Antenna surface area
T_e	Electron temperature
T_i	Ion temperature
T_g	Neutral gas temperature
t	Time
W_f	Work function
α	Distribution Controlling Parameter
η	Aperture efficiency
ζ	Beam shaping parameter
Ω_A	Solid Angle
ω	Angular frequency
ω_p	Plasma angular frequency
λ	Wavelength
λ_g	Guided Wavelength
λ_0	Operating Wavelength
λ_c	Cut-off Wavelength
ϵ_0	Permittivity of free space
ϵ_e	Effective permittivity
μ_0	Permeability of free space

Chapter 1

Introduction

1.1 Background

High-power microwave (HPM) devices are used in multiple scientific and industrial applications, including particle accelerators, communications, and defense technology [1, 2]. Microwave tubes are the main basis of HPM devices and can be divided into two subcategories: O-type devices and M-type devices. In O-type devices, the electron interacts with the electric field alone, while in M-type, the interaction of electrons occurs with crossed fields, i.e. mutually perpendicular electric and magnetic fields. A classification of microwave devices is shown in Fig. 1.1.

The choice of a device depends on its frequency of operation, its power requirements and the environment in which it will be deployed. Each device has its own characteristics, for example, the output power of a multi-cavity klystron expressed in kilowatts (kW) with a gain of 50 to 80 dB, but with a limited bandwidth (MHz). The traveling wave tube amplifier (TWTA) is a broadband amplifier but with an output power of several watts. Similarly, the back wave oscillator (BWO) is the best choice for modern warfare with high output power and bandwidth. Typically, the klystron amplifier is used in linear accelerators for medical applications. There are many HPM systems in the world, such as the active denial system (ADS), which are used as non-lethal weapons to strengthen the defense

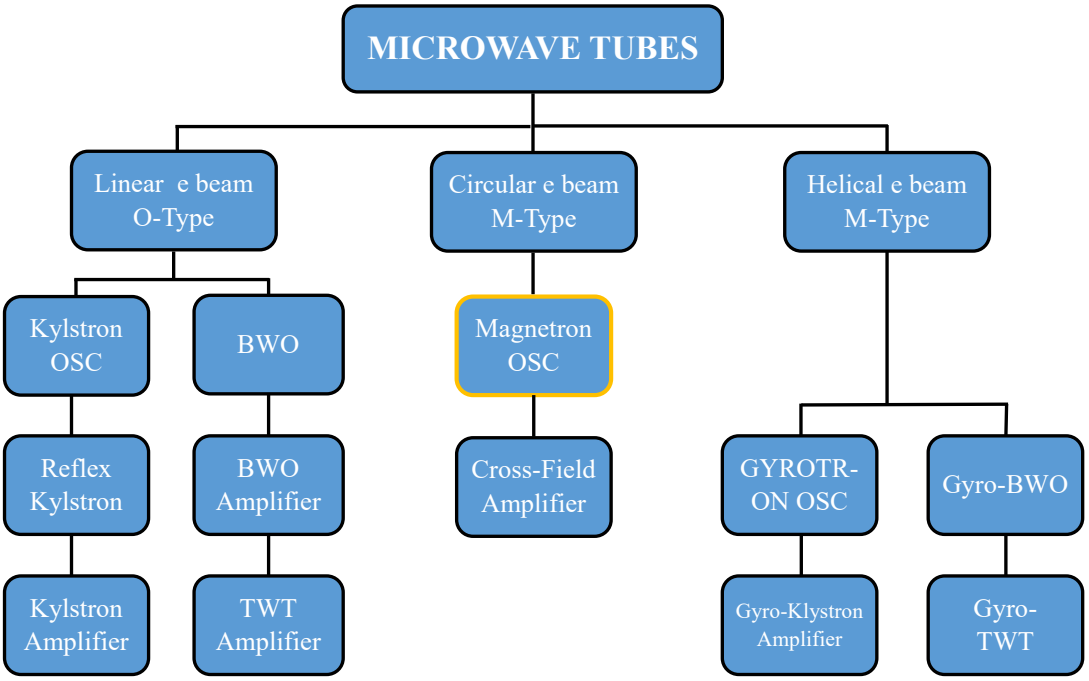

FIGURE 1.1: Classification of Microwave devices.

of a country. The realization of a modern HPM system requires electro-vacuum devices with an output pulse power greater than 100 MW. It should be noted that at such power, when the structure is comparable to the wavelength, energy can be imparted to bring an electron into the relativistic velocity domain. Multi-GW power can be achieved with particle energies greater than 1 MV at currents of tens of kA for longer wavelengths [3].

The device of interest for this research is the magnetron. However, in magnetrons, a pulse power of this order is obtained with an anode voltage of several hundred kilovolts (320 - 450 kV). Therefore, the application of such devices is often limited by the size and bulk of their power sources, and large device geometries. It is therefore advantageous not only to improve the efficiency of the device but also to take into account the electrical properties of the device. A lower anode voltage is preferable because it reduces power supply stresses and heating problems. It also improves the reliability of the device, as the low anode voltages lead to reduced electrical stresses on the dielectric and, therefore, give greater reliability during operation [4].

Electrically sensitive devices; such as particle accelerators and X-ray generators, use high frequency microwave pulses, of the order of hundreds of MW with precise control upon signal amplitude and phase. The stringent requirements of these applications translate directly into requirements for RF source parameters, which increases the cost and complexity of the device. RF pulse compression is often used to reduce this cost by transforming a wider, lower power pulse into a shorter, higher power pulse. This process reduces the required output power of the source; therefore, resulting in an economical and efficient device. RF pulse compression is a mature technology that can be used by various methods reported in the literature [5–7]. A review of these methods is given in Chapter-2.

The efficiency of an HPM system depends on its radiating elements commonly called transmitting antenna. The antenna receives the HPM pulses from the source and transmits them through the air without reaching breakdown. The most popular antenna in the field of HPM is the horn antenna. It is widely used due to its simple design. However, its directivity and beam scanning capabilities are limited. Along with the development of HPM technologies, there is an increased interest in associated antennas; so they must have high gains, high power handling capabilities, and efficient beam steering. Since most of the HPM antennas have a narrow bandwidth, therefore, sweeping the beam over a wider range is considered a difficult task for these antennas. Conventionally, HPM antennas with reflectors, such as Vlasov and coaxial beam rotating antennas, have achieved high power handling capability; however, these antennas have an asymmetrical radiation pattern, which leads to low radiation efficiency. Controlled beam scanning capability with high power handling and low side lobe level (SLL) are considered crucial design parameters for an HPM transmission system.

In an HPM system, mechanical movement is not a preferred choice due to high power consumption and overshoot, which could potentially generate delay and/or ambiguity in the target location. In order to overcome these limitations, different HPM antenna array systems have been proposed in [1–3]. These designs are complex in nature and could not effectively handle high SLLs in the azimuth and elevation planes. Additionally, the gain achieved with these designs requires

even more research to improve its value with minimal additional complexity. To facilitate beam scanning, the complexity increases many folds due to the addition of a phase shifter which is an integral part of an array antenna.

1.2 Research Motivation

Contrary to the extensive published literature on plasma sources and their applications, there is little research on the use of plasma switches in pulse compression technology. Some conventional designs using waveguides in conjunction with trigatron switches exist, but are limited to long pulse duration. For higher energy systems with longer pulses (MW power range), usually amplifiers, such as klystrons, are used and the discharge process is initiated by phase inversion at low power. However, for high power sources, such as magnetrons, there is no high power phase inversion method. This was identified as one of the challenges of this research. The objective is to use a plasma confined tube as a switch to obtain the phase inversion of a megawatt signal generated by a magnetron.

HPM-based slotted waveguide antenna (SWA) is an emerging technology, used in military and defense applications. Although, some SWA designs are available in the literature for defense applications, but have limited beam sweep range, directionality, and power handling capability. Therefore, it is necessary to study HPM-SWA for GW applications. The major problem with a single SWA is that it suffers from a very wide elevation beam. This problem can be solved by modifying the top radiating surface of SWA.

Most of the developed SWA configurations, intended for HPM applications, exhibited significant gain degradation during beam scanning. Moreover, such systems involved a high degree of complexity, leading to manufacturing difficulties and high costs. Additionally, some of the published designs have very high SLL, also suffer from back and grating lobes. Therefore, there is a need for a well-designed SWA array to achieve high directivity, high power handling capability, tunable SLLs as

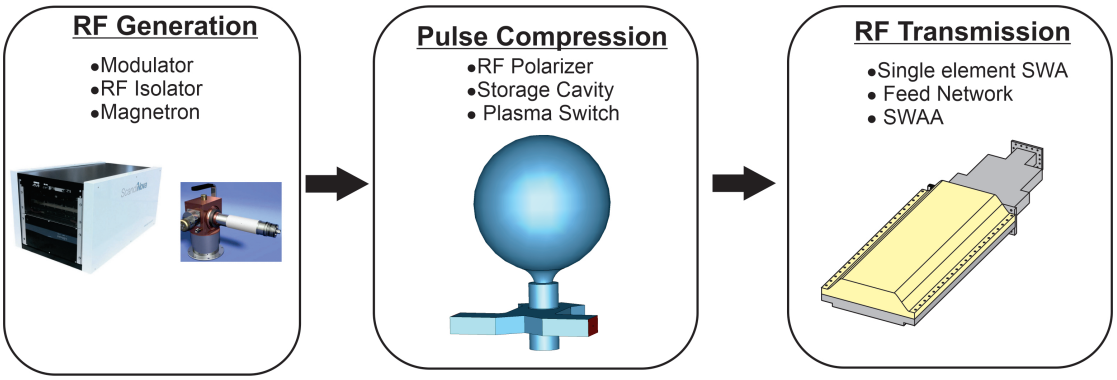

FIGURE 1.2: Block diagram illustrating gigawatts microwave generation and transmission.

well as wider beam scanning range. In addition, mutual coupling should be minimized in the target SWA array to avoid inter-element interference, to minimize radiation pattern distortion.

1.3 Contribution of Dissertation

The goal of this dissertation is to generate HPM pulses of relatively longer duration, and to compress them into shorter duration pulses having a high power (GW). These compressed pulses will then be transmitted using a highly directive array antenna designed for the purpose. The basic block diagram of the proposed idea is shown in Fig. 1.2. As shown in the figure, the overall project is divided into two main parts: a) microwave pulse compression and b) pulse transmission through a GW capacity array antenna.

1.3.1 Microwave Pulse Compression (MPC)

Microwave pulse compression is a method used to convert a longer pulse of low RF power to a shorter pulse with high RF power. A complete pulse compression system is a combination of an RF polarizer integrated with a storage cavity. The RF polarizer based pulse compressor uses a cavity to load the low power RF signal. The fundamental concept behind the cavity discharge is to achieve a phase

inversion (180°) on the input side at a particular instant. A new compact and effective technique aims to be developed to discharge the cavity by employing an appropriate technique. Pulse compression consists of three main components:

a. RF Polarizer;

b. cavity to store energy;

c. switch to define discharging.

1.3.1.1 RF Polarizer

The RF polarizer is a key component of an MPC system and must have efficient RF performance parameters, such as low reflections and high isolation at its input and output ports. In addition, it must be compact so that the system is economical from a space point of view. An efficient mode conversion mechanism is another main characteristic used to classify the quality of a polarizer. Based on these requirements, a polarizer can be divided into three sections: a) mode generation section; b) overmode section and c) dual mode section.

1.3.1.2 RF Storage Cavity

The output of the RF polarizer is fed into the storage cavity. Different types of RF storage cavities are used to store RF energy. Types of storage cavities are included, but not limited to: rectangular and spherical cavities. The basic constraint with a rectangular cavity is that it can store RF energy of shorter duration. Because the cavity size becomes very large when the signal is of longer wavelength. On the other hand, the spherical cavity offers the storage of longer RF pulses as well as a good perturbation $Q-$Factor, which has an important role in determining the RF energy storage capacity by the cavity.

1.3.1.3 RF Plasma Switch

An RF plasma switch can be applied to an HPM system by exploiting its ability to behave as a high frequency switch in MPC. RF plasma sources are capable of operating in both continuous, repetitive, or pulsed operating conditions; allowing the formation of narrow or wide charge particle beams. Due to the fast response time, a plasma switch can be used in MPC systems to reflect RF waves, allowing high power discharge. Different types of gas discharge can be used for plasma generation; such as cold cathode glow discharge, arc type discharge, triggered discharge and high frequency discharge. The required plasma characteristics depend on the need for an MPC system and its applications. Although it is possible to generate plasma at atmospheric pressure, most applications use a low vacuum ($1-1000$ Pa) for a plasma source. Some important parameters to consider are: conductivity; frequency; the collision rate and the permittivity in the longitudinal and radial directions. There are two ways to generate plasma: a) by using a tube filled with gas loaded with electrodes, b) or by energizing the gas using electromagnetic radiation. The first uses a voltage for excitation, and the second is generated by an RF source of appropriate energy. In this research, it is proposed that a suitable plasma switch be designed, optimizing all its design parameters, to meet the needs of high energy RF pulse compression and its subsequent transmission.

1.3.1.4 GW Array Antenna

In order to effectively transmit an HPM signal into the atmosphere, a proper array antenna system configuration would be required, which should have good directivity as well as accurate beam steering capabilities. There are a variety of antenna arrays that are used for HPM devices, but the most preferred design is a slotted waveguide (SWA) antenna. SWA offers symmetrical electric and magnetic fields with good controllability on SLLs. The realization of such an antenna array consists of the following steps:

a. development of a single element SWA;

b. design of SWA feed network and

c. design, fabrication and testing of slotted waveguide array antenna (SWAA).

Single Unit of SWA: The overall efficiency of an array antenna depends on the design of its unit element. The main task in the design process of a SWA is to control its SLLs and improve its directivity. To achieve the target directivity, it is necessary to improve the design of SWA by controlling its surface current. It is possible to obtain the same thing by modifying the distribution of the slots and the surface structure of the waveguide. To have additional control over the radiating environment of SWA and to improve high power capability, the radiator can be placed in a specific environment called a radome. This research also aims to design a suitable radome for the transmission of GW energy by controlling the radiator ambiance.

Feed Network for Array Antenna: In an array antenna, power is usually supplied to the input of the array for onward transmission. This power is generated from a single source, and in order to provide an equal amplitude signal to the input of each element, it is necessary to divide the signal by a mechanism, commonly known as a power divider (PD). A PD of an HPM system must offer minimum insertion loss and its output must have a signal of equal amplitude and identical phases. Also, as the proposed transmission is intended for GW applications, the PD should have the capability to support this requirement. Therefore, waveguide-based PD might be a logical choice, since waveguides have the ability to handle GW power comfortably.

SWAA: In the last part of this research, the objective is to design a Slotted Waveguide Array Antenna (SWAA) by extending the concept of SWA. Here, the goal is to design a phase array of improved directivity with a reasonable beam scanning (greater than ± 20). Keeping a realistic goal in mind, the proposed SWAA can be developed involving four SWA units that will be integrated together

to achieve a single system. Improved directivity can be achieved by exploring techniques such that the mutual coupling between elements should be as low as possible, to allow maximum energy to fall into the main lobe of the antenna. Additionally, the target SWAA should provide maximum beam scanning with minimum gain loss.

1.4 Research Objectives

Plasma switch-based pulse compressor: the proposed task can be accomplished by investigating the following:

a. Design, simulation, and fabrication of a plasma tube and RF polarizer for S-band applications.

b. Testing of argon plasma tube as switch for simulated parameters.

c. Cold test of RF polarizer for performance analysis.

d. Simulation and fabrication of cavity.

e. Cold test of cavity with RF polarizer.

f. Testing of plasma switch as a phase reversal switch with RF polarizer and cavity.

GW Transmit antenna: to accomplish this task following methodology has been proposed:

a. Design and simulation of an efficient SWA and its array with optimum number of elements to achieve desired directivity with no back and grating lobes.

b. Power handling capacity greater than 1 GW.

c. SLLs less than -20 dB, which may be achieved by appropriately modifying the slot distributions.

d. Reduction in mutual coupling (≤ -25dB) among the array elements to improve gain and beam scanning.

e. Designing of an efficient PD with low insertion losses.

f. Design and implementation of a dielectric radome to enhance the far-field characteristics without affecting performance parameters (impedance matching, SLL, isolation, gain).

1.5 Dissertation Outline

This chapter presents details about HPM systems, their basic building blocks and their use in industry. Possible avenues for establishing research targets were identified. It is discussed that an S-band GW system is intended to be developed involving pulse compression and transmission. The rest of the dissertation has the following organization:

Chapter 2 discusses the literature review that serves as the basis for the research of this dissertation. In this chapter, a historical perspective of high power microwave antennas, its types and capacity is presented. It has been discussed that traditionally a horn antenna with an appropriate feed structure was used, to transmit high power signals, whenever needed. The chapter further introduces the leaky waveguide array antenna and its performance degradation. It was discussed in this chapter that for a high power array configuration, a new technique is required to achieve high directivity and reduced mutual coupling.

Chapter 3 deals with the design, simulation and cold test verification of the developed RF polarizer. The design of an RF polarizer with a variable stroke length response is presented in this chapter, to achieve the desired phase inversion and reflection coefficients for successful compression of an RF pulse. A cold test is carried out with a piston by varying the stroke length.

Chapter 4 deals with plasma columns, uses of plasma as a switch, and RF-plasma interaction. This chapter discusses the importance of RF-plasma interaction and

its theoretical understanding. The plasma interaction behavior is observed in Magic3D and a simulation study of argon plasma generation with the required characteristics is performed in COMSOL and then verified experimentally.

Chapter 5 deals with resonant cavities and presents the results of the cold test of the spherical copper cavity. The chapter also presents the use of cavities for the energy storage of pulse compression systems. Simulation results for rectangular and spherical cavities show that adding a cavity structure to a waveguide reduces charging time.

Chapter 6 introduces the SWA-based HPM antenna system and its performance parameters. In this chapter, an improved SWA system is proposed for S-band HPM applications. To achieve -20 dB SLL, 10 slots with rounded edges are etched on the wide sidewall, and their displacement/shift around the center line is presented using a modified Gaussian distribution. The antenna design based on the Elliot slotted waveguide procedure is discussed. The chapter provides details of inside groove and dielectric radome which are developed to improve gain and high power transmission.

Chapter 7 features a slotted waveguide antenna (SWAA) array that was developed for S-band HPM applications. The array is developed using four slotted waveguide antennas of identical configuration. Electromagnetic modeling was performed in CST MWS. The array was made using rectangular waveguides capable of handling GW energy. A beam scanning of ± 22 is also demonstrated in this chapter.

Chapter 8 presents the conclusions drawn from this research. Additionally, recommendations on how existing work can be extended using the technology/understanding established in this dissertation were also mentioned.

Chapter 2

Literature Review

The main components of an HPM system are: (a) a pulse compression device with phase inversion/discharge and (b) an efficient antenna to transmit the energy. The goal of this research is the integration of these multiple devices and to this end, a detailed literature review was performed to uncover research gaps and the current state of technology. The following sections describe the literature related to plasma and its applications, RF pulse compression methods, resonant cavities and their structures, HPM antennas and antenna arrays.

2.1 Theory and Types of Plasma Switch

There is an extensive literature on plasma due to its wide applicability in many industrial, academic, and military applications. When the plasma density matches Epstein's profile, it has the ability to absorb or reflect microwave radiation. The absorption or reflection of incident waves by the plasma depends on its density and the associated characteristics [8, 9]. It is an established fact that the absorption amplitude of an incident microwave is mainly determined by the temperature of the plasma and its electron density. The main parameters that play a critical role in the interaction of the microwaves with the plasma are: the angle of incidence

of the microwaves; their polarization; density of electrons (N_e) inside the plasma and collision frequency (f_c) of the charges defining the plasma.

In [8], it was established that at low density, collisional plasma reflects less microwaves. It has been observed by Vidmar *et al.* that when the plasma density is low, it becomes less reflective to RF radiation and most of the incident waves propagate through it considering it as a transparent medium. In [10] different experiments were carried out to analyze the attenuation of microwaves during their propagation through a plasma, for the frequency range from 7 to 12 GHz. An attenuation of 4.5 dB in the injected microwave signal was observed during its propagation through a waveguide loaded with plasma. Yeh *et al.* studied the microwave-plasma interaction and for this purpose they assumed a parabolic plasma density profile, and the study used both anisotropic and inhomogeneous plasma columns [11]. Inhomogeneous dense plasma has also been studied in [12] to assess the reflection and absorption of microwave radiation. In these two studies, the results showed that a parabolic distribution of N_e is more efficient for the scattering of a MW microwave signal [12].

A number of studies have been conducted to investigate microwave discharge using plasma under atmospheric pressure. The common properties of plasma under atmospheric pressure are: a) a moderate neutral temperature, of the order of a few thousand Kelvin; b) a plasma density of the order of $N_e \sim 10^{14}$ cm^{-3} and c) an electron temperature as low as $1-2$ eV [13]. The applications of plasma under atmospheric pressure are numerous; such as the decomposition of a toxic gas, atomic spectrometry and the treatment of thermally resistant materials [14, 15].

Fewer attempts have been made in the literature to numerically model the plasma-microwave interaction. In this respect, different reactions involved in such an interaction are to be considered; such as charge particle motion under altered conditions, plasma perturbation with the presence of external fields, charge particle profile, etc. A plasma-microwave interaction can be modeled using a 2-D or 3-D framework, depending on the physical geometry of the system in which the interaction takes place. However, for accurate prediction of the results, especially in a

waveguide structure, a 3D model will be needed for an adequate understanding of the plasma-microwave interaction, but only a few such studies have been reported. In [16], the authors conducted experiments to observe the discharge of a 915 MHz RF signal using plasma in a glass tube. A microwave plasma model was developed in [17] where it was demonstrated that with a rapid influx of gas, used for plasma creation, there would be a reflection of the microwave signal due to the increase of N_e.

In order to excite the plasma using high power microwaves, the conical waveguide structure has been routinely used. To maintain plasma ignition using microwaves, a high electric field towards the focused direction is required, which is normally difficult to achieve in a conventional waveguide structure. To achieve the focused electric field between the electrodes of a plasma tube, a waveguide with a ridged structure has been developed and reported in [18]. In this study, the optimization was applied to design the structure which resulted in a focused electric field in the region where the discharge will take place upon plasma excitation.

The interaction of plasma and RF microwaves has been realized in [19]. The main objective was to determine the absorption of microwaves in the presence of a plasma source. The simulations were performed in the X band (8−12 GHz) using a standard horn antenna as the RF source in the CST® software. Plasma frequency effects on X-band microwave attenuation were achieved using an array of plasma tubes mounted on a Teflon backing. The array configuration based on plasma tubes was illuminated by an RF source equipped with a horn antenna, unlike other studies in which the plasma source is usually illuminated by plane waves, to simplify the simulation model. The attenuation of the microwave signal at 100 GHz was observed with a variable plasma frequency (0.02 GHz−3 GHz) [19].

In [20], a microwave torch was formed by the glow of plasma at atmospheric pressure, in a silica tube filled with a gas mixture of Ar and O_2. The glowing plasma was produced at the end of the discharge tube and exposed to ambient air. Detailed parametric analysis was performed to determine optimized performance

parameters which included: plasma density; plasma volume; plasma profile and temperature. In addition, the effects of mixed gases, flow rate and corresponding microwave power were measured for the proposed prototype. Zhang *et al.* in [21] reported a mechanism developed to improve plasma-microwave coupling efficiency by choosing a suitable glass-tube integrated plasma torch to be deployed in a metal chamber. The proposed prototype has been made efficient by avoiding unnecessary tuners which usually require a couple of stub/plunger tuners.

A hybrid plasma model simulation study was carried out in [22]. It was performed under normal atmospheric pressure to observe Ar gas-based DC micro-glow discharge. A pin-plate electrode configuration was simulated and implemented with an inter-electrode spacing of 200 μm. The current-voltage characteristics and the density profile indicated the discharge profile as a normal glow discharge. Evaluation of the neutral gas temperature was carried out which revealed that the observed discharge consists of non-thermal and non-equilibrium plasma.

Garamoon *et al.* [23] investigated the dependence of breakdown voltage, normal luminescence potential, and cathodic drop potential on Ar gas pressure and electrode spacing. It has been observed that the normal luminescence potential decreases when the gas pressure increases and on the other hand, it increases with increasing inter-electrode spacing values. In [24], a gas-filled cylindrical tube configuration was deployed for a DC glow discharge with an anode and a cathode attached to both ends of the tube. DC glow discharge appeared for the discharge current ranging from micro to milli ampere for pressure from 0.5 to 300 Pa. DC glow discharge was investigated experimentally by Matthew *et al.* in [25] where they studied the effects of gas breakdown voltage, anode/cathode geometry and distance between anode and cathode. It has been observed that the breakdown voltage depends on the gas pressure as well as the anode-cathode separation ratio and their geometry (radii).

In [26], another study was performed at atmospheric pressure, to observe the negative effects of corona discharge on the glow discharge region. The current-voltage curve of the pin-to-plate configuration shows three different discharge regions: a)

spark; b) crown and c) luminescent regions. The intensity of the light discharge indicates the different electric field values for three regimes. Another study on atmospheric DC flow can be found in [27] where the authors presented the experimental validation of DC glow discharge while maintaining atmospheric pressure. They observed an electron density of 10^{18} m^{-3} and a gas temperature of 2000 K. The study suggested that such a plasma could be implemented to air pollution control. It has been reported that the plasma has a high electron density ($10^{18} - 10^{20}$ m^{-3}) resulting into the creation of a large volume.

The analysis of the glow discharge phenomenon in a plasma switch for a DC bias, is presented in [28] with its simulated data and numerical model. The proposed model is based on the Poisson equation which describes the motion of electrons and ions under particular boundary conditions. The analysis of the radial effect during the glow discharge, in a plasma switch, after the application of DC voltage, is a useful technique for analyzing the properties of the plasma. It has been observed that the electrons are attracted towards the glow center which has a negative region and the positive ions are moved away from this region due to the radial directed electric field. A comparative analysis of different models, under low pressure DC glow discharge for cold cathode, has been carried out in [29]. They reviewed known modeling approaches and developed their own simulation codes. They also performed calculations for reference sets of discharge conditions, and performed a critical comparison of various model parameters. For validation of the simulated data, they used Langmuir probe methods to measure electron density involving Ar gas glow discharge.

Kimura *et al.* [30] studied experimentally and theoretically the DC glow discharge based on an $Ar-N_2$ mixture. The amount of N_2 gas flow in the plasma tube plays an important role in the distribution of electron energy in the plasma column which showed a tangible deviation from the Maxwellian distribution with increasing amount of N_2. The density of N_2 and Ar gas under meta-stable species shows the inverse relationship with the N_2 content estimated from the rate equation. There is a significant difference between the experimental and theoretical estimated energy distribution of electrons, especially towards the positive side of the

column, which contains N_2 gas. A summary of the microwave plasma interaction discussed in the previous paragraphs is appended below in Table 2.1

TABLE 2.1: A summarized history of plasma switch and its various developmental stages.

Author's	Year	Developments	Ref.
Yeh *et al.*	1965	Interaction of microwaves with inhomogeneous and anisotropic plasma	[11]
Boeuf	1988	A two dimensional model of DC glow discharges	[28]
Vidmar	1990	Atmospheric pressure plasmas as electromagnetic reflectors and absorbers	[8]
Laroussi *et al.*	1993	Reflection, absorption, and transmission of microwaves by a plasma	[9]
Kimura	1994	Experimental and theoretical investigations of DC glow discharge	[30]
AShen *et al.*	1995	Properties of a vacuum ultraviolet laser created plasma sheet	[10]
Al-Shamma *et al.*	2001	Development of a 2.45 GHz waveguide-based microwave plasma	[14]
Goossens *et al.*	2002	The DC glow discharge at atmospheric pressure	[26]
Hong *et al.*	2003	Abatement of CF_4 by atmospheric-pressure microwave plasma torch	[15]
Garamoon *et al.*	2003	Electrical characteristics of a DC glow discharge	[23]
Machala *et al.*	2004	DC glow discharges in atmospheric pressure air	[27]
Moona *et al.*	2006	Parametric study of atmospheric pressure microwave-induced Ar/N_2 plasmas	[20]
Farouk *et al.*	2006	DC atmospheric pressure argon micro glow-discharge	[22]

Author's	Year	Developments	Ref.
Kabouzi *et al.*	2007	Modeling of atmospheric-pressure plasma columns	[16]
Derzsi	2009	Accuracy and limitations of fluid models in DC glow discharge	[29]
Nowakowska *et al.*	2013	Modelling of discharge in a high-flow microwave plasma	[17]
Zhang *et al.*	2014	Investigations on microwave absorption by a cold plasma	[12]
Gudmundsson *et al.*	2017	Foundations of DC plasma sources	[24]
Mathew *et al.*	2019	Experimental verification of modified Paschen's law	[25]
Zhang *et al.*	2019	Propagating modes of the travelling wave in a microwave plasma	[21]
Deng *et al.*	2021	Design of a novel microwave plasma source based on ridged waveguide	[18]
Joshi *et al.*	2022	Attenuation of electromagnetic waves in plasma using Drude model	[19]

2.2 HPM Pulse Compression

In [31], researchers proposed a novel approach to design a geometry containing large cumulative systems of compact MPCs to generate ∼10 ns rectangular pulses in the S and X-bands. This design has standard waveguide elements containing single-mode and multi-mode sections connected in T-junctions. One of the T-arms was connected to a resonant cavity and the second arm was shortened while the third arm was connected to a linear waveguide. Finally, a resonance breaking plasma switch was mounted in the side arm of another tee. Thus, a compact system was developed involving planar and three-dimensional structures.

An overmode corrugated internal helical circular waveguide was presented in [32], for RF pulse compression. The resulting pulse was 25 times greater than the input peak power, while the pulse duration was reduced from 80 ns to 1.5 ns. However, this design exhibited a 5% frequency sweep with eigenwave propagation having a frequency-dependent group velocity away from the cutoff. Additionally, the dispersive characteristics associated with high RF breakdown thresholds and low resistive losses made this helical wave design more attractive for a relatively high peak power microwave signal.

The SLAC energy-doubler (SLED) polarizer is a compact device that uses smooth, rounded surfaces to drive a high-power overmoded system [6]. The original design used two high quality resonators to store energy from an RF source for relatively longer duration pulses (μs range) and release them in short bursts. In this way, a pulse compression efficiency of 60% was achieved.

The generation of high-power microwaves using a metallic waveguide as a dispersive medium has been presented in [3]. The principle of operation of their reported design is to sweep the frequency in a modulated pulse train with monotonically increasing group velocity, propagating in the waveguide. Eventually, the trailing edge of the pulse approaches the leading edge, which shortens the pulse and increases its peak power amplitude, subject to small losses. In this technique, the group velocity changes significantly near the cutoff frequency compared to its value away from the cutoff. Therefore, the feasible frequency range for pulse compression is closer to the cutoff frequency, as reported in [33]. This technique is of restricted applicability because of the high ohmic losses and its operating constraints as close as possible to the cut-off frequency. The limitations associated with this technique prevent a high compression ratio; resulting in low energy efficiency, as stated in [3].

Generally, structures with specialized properties are used instead of smooth waveguides. A barrel-type open cavity (BOC) is presented in [34], which is simulated using CST Studio and HFSS. Such pulse compressors are widely used in linear accelerators and are of paramount importance, since the efficiency of the RF power

accelerator depends on them. Unlike the traditional SLED-type pulse compressor, the BOC is composed of a unique barrel-shaped structure and a corresponding waveguide. Due to the low power loss of the inner surface, BOC offers a high unloaded Q value of $> 90,000$. In [34], a BOC-based system was simulated in which a 3 μs pulse was compressed into a 330 ns pulse, with a maximum output power of 50 MW.

Besides the use of spherical cavities as energy storage elements, cylindrical resonant cavities have also been reported since the realization of the first SLED [35]. Considering the nature of the problem requiring low cross-polarization field, low loss and wide bandwidth, corrugated cylindrical structures have been used for several decades [36] in the HPM industry. Helical corrugated waveguides are also used as a dispersive medium to compress frequency swept pulses [33, 37]. One such research using a corrugated cylindrical structure as an energy storage element for compression is reported in [38]. It employed an X-band (11.424 GHz) cavity with a high unloaded Q factor (>100,000).

In a klystron based power amplification system, a klystron continues to fill power into a cylindrical cavity until the phase of the microwave pulse is reversed, then power from the cavity and klystron is added and transmitted to the accelerator assembly using an RF polarizer. Subsequently, peak microwave power up to 150 MW is achieved with a peak microwave power gain of 4. Using a klystron-based technique, the pulse duration can be compressed from 800 ns to 100 ns.

Y. Jiang *et al.* in 2019, demonstrated a cavity based pulse compression system for HPM applications [39]. They designed, fabricated and tested a system comprising upon eight high $Q-$factor spherical cavities with four polarizers. They obtained pulse compression efficiency of 6% and their design worked both for C and S-band comfortably with 20.8 MW power handling capability. In 2020, Z. V. Drikas *et al.* [40] attained microwave ultra short pulses using electromagnetic time reversal technique. Their system offered ultra wide bandwidth ($5 - 8$ GHz) and power handling capacity of 39.2 kW. These results are considered good for the adopted technique. Y. Jiang *et al.* [41] in 2021, developed an X-band corrugated cavity

having dimensions 7×20 cm^2 with $Q-$factor as high as 116000. This is claimed as a smallest cavity of high $Q-$factor. They attained 150 MW peak power from the compressed pulses. However, they showed couple of limitations of their system; such as, relatively low breakdown and high local temperature due to corrugated structure. X. Lei *et al.* [42] in 2023, demonstrated a high gain S-band pulse compression system using a rectangular waveguide for $TE_{1,0,20}$ mode. Relative to the traditional pulse compression system, they reported 51.86% improved gain with 23.33% increased efficiency. They claimed that their design can comfortably be extended to X and K-band high power applications. The techniques discussed in the preceding paragraphs are summarized in table 2.2

TABLE 2.2: A summarized history of plasma pulse compression techniques reported in the literature.

Author's	Year	Developments	Ref.
Clarricoats	1984	Corrugated horns for microwave antennas	[36]
Samsonov *et al.*	2004	Frequency modulated pulses using helically corrugated waveguides	[3]
Burt *et al.*	2005	MPC using a helically corrugated waveguide structure	[37]
McStravick *et al.*	2010	MPC using helically corrugated waveguide.	[32]
Zhang *et al.*	2015	MPC using a five-fold helically corrugated waveguide	[33]
Artemenko *et al.*	2016	HPM pulse compressors with accumulative resonant cavity	[31]
Shu *et al.*	2017	C-band barrel open cavity pulse compressor	[34]
Woolley *et al.*	2017	Control and performance improvements of a pulse compressor accelerating structures	[35]
Jiang *et al.*	2018	X-band pulse compressor for TTX	[38]
Jiang *et al.*	2019	Rectification in pulse shape using a cavity based system	[39]
Drikas *et al.*	2020	Pulse compression by time-reversal techniques	[40]

Author's	Year	Developments	Ref.
Jiang *et al.*	2021	Microwave X-band pulse compression by employing a corrugated cylindrical cavity	[41]
Zhang *et al.*	2023	Design of a relatively high gain over-moded HPM system	[42]

2.3 HPM Array Antenna Configurations

There are many HPM antennas reported in the past in which the most famous antenna is the horn antenna. It is a compact antenna with over 1 GW power handling capability with reasonable gain and low SLLs. This device, electronically, cannot offer a [43] beam scanning function. In 2013, Vlasov gave the concept of a mode converter using a quasi-optical transformer which converts the wave of circular section into fundamental wave of rectangular waveguide. Using this concept, the Vlasov antenna was presented [44]. This has a cylindrical shape but ends in a cut shape. There are two famous cut shaped of Vlasov antenna. One is step cut and the other is bevelled cut. The bevelled cut gives lower SLL while the step cut results in higher gain and lower HPBW.

There is another example of a high power antenna called a mode transducing antenna. It has TE_{01} mode, known as low-loss mode. The antenna generally has a larger cross-section, which allows it to transmit higher power signals [45]. The radial line helical antenna array has higher gain and can also handle higher power [46]. In this design, beam steering is possible by mechanically moving the antenna. The EZ antenna is a small HPM antenna, typically used for testing HPM sources. The mode converter with radiant horn to convert TM_{01} mode to TE_{11} mode is also used in HPM transmission. Mode conversion is required because the TM_{0n} mode has a doughnut pattern, which is undesirable for HPM transmission. The radial slot array antenna uses radial line slow wave structure to improve power handling capability instead of high gain dielectric foil [47–49]. The leaky wave

array antenna can provide beam scanning in the E-plane by varying the phase of each radiating element. It offers more than 30 dBi typical gain with more than 1 GW power handling capability, but with low SLLs. This effect is normally ignored in HPM applications because SLLs play a negative role, mainly, in communication systems [50, 51].

For the monopole antenna array, a brief mathematical modeling method of the phased array antenna is discussed in [52]. The authors found that the binomial current distribution is more useful for SLL suppression than the uniform current distribution. A high gain antenna array designed for HPM applications has been presented in [53]. It consists of four sub-arrays of four rectangular patch elements with a power handling capacity of approximately 1 kW. In an array antenna, it is always necessary to optimize the excitation amplitude, the phase and the inter-element spacing of the array, which has been explained in [52, 54]. They discussed techniques that can be used to achieve the desired gain with low SLLs, narrow HPBW, and controlled nulls.

A radial helical array antenna consisted of eight ring feeds using specially designed slots waveguide coupled to helical antenna elements featuring 30 dBi gain and power handling capability 100 MW is presented in [55]. In addition to electronic scanning, the radiation beam from an HPM horn antenna can be scanned by attaching a Risley prism lens to the aperture of the antenna [56]. In this technique, one lens remains in its position and the other lens rotates. Although it is a very unique idea to make a phased array horn, however, it is necessary to rotate the lens mechanically. A novel design of a slotted array antenna with a narrow sidewall and mechanical beam scanning capability is discussed in [57]. The proposed antenna can steer the beam in the azimuth plane by changing the source frequency. However, in practice, narrow band sources like the relativistic magnetron cannot easily change their operating frequency. So, to make the beam steerable, the wider dimensions of the waveguide wall must vary, which is not really a feasible option. The single-layer radial line helical antenna composed of sixteen elements has a gain of about 23 dBi with a power handling capability of 625 MW was presented

in [58] but it does not have beam steering functionality. Another new radial helical array antenna discussed in [59] which can accept azimuth output signal from HPM sources such as VCO, MILO and radiate it in circularly polarized form. Thus eliminating the need for mode converter which makes it more suitable for HPM applications. A helical antenna array with sufficient beam sweep capability is discussed in [60]. It has a low power handling capacity of about 100MW, and the design complexity is also high.

A leaky waveguide antenna for the X-band with a gain of 26 dBi and a power handling capacity of about 200 MW is presented in [51]. The leaky wave antenna can provide beam sweep in the E-plane by varying the phase of the input source and in the H-plane by varying the operating frequency. The elliptical slotted waveguide array antenna provides high power handling capability, as the elliptical shape is better than the rectangular slot for high power applications. The gain of the reported array [61] is about 17 dBi for 10 slots on the broader wall of the waveguide without Balun. It overcame the efficiency issue that appeared in [58] because of reduced aperture size. Its reflection cancellation structure is softer than the previous design with excellent directivity (32 dBi) and power handling capacity of 500 MW. But it cannot provide e-beam scanning functionality. Recently, a 48-way X-band leaky waveguide array antenna was demonstrated, which had a power handling capability of over 1.5 GW with a directivity of 38.75 dBi [62]. Beam scanning in the slotted waveguide array antenna presented in [63] has high power handling capability ($\sim$ 1 GW), but also with high SLLs.

The groove structures in the slotted array configuration are used for dual purposes, reducing mutual coupling and improving gain. Mutual coupling between array elements degrades beam scanning capability and causes power flow to the source. These are the critical issues in designing a phased array antenna for large beam steering capability. Finding the optimum spacing will result in no nulls and grating lobes is also a very challenging in the design of an HPM phased array antenna. Undesirable mutual coupling between array elements is overcome using different techniques including inter element spacing, metal wall integration, frequency-selective surfaces, metamaterial structures, and introduction of grooved

regions [64]. Specially designed grooved regions suppress the propagation of surface waves. The redistribution of electromagnetic waves in the slotted regions produces high surface currents in the grooves, suppresses unwanted currents and re-radiates as a secondary source [65, 66]. A comprehensive summary of the HPM antenna discussed in this section is presented in Table 2.3.

TABLE 2.3: Developmental history of high power microwave antenna array.

Author's	Year	Developments	Ref.
Li *et al.*	2008	GW radial line helical array antenna	[58]
Huang *et al.*	2009	Grooves-assisted mutual coupling reduction and gain enhancement	[65]
Chang *et al.*	2010	Design and experiments of the GW high-power microwave feed horn	[43]
Godard *et al.*	2010	A transient UWB antenna array used with complex impedance surface	[45]
Li *et al.*	2010	16-element rectangular radial line helical array antenna for HPM applications	[55]
Li *et al.*	2011	Design and simulation of X-band HPM antenna based on leaky waveguide	[51]
Kaur	2012	Electronically steerable planar phased array antenna	[52]
Misilmani *et al.*	2013	Improved Vlasov antenna with curved cuts for HPM applications	[44]
Yuan *et al.*	2013	Designs and experiments of a novel radial line slot antenna for HPM applications	[49]
Husseini *et al.*	2013	S-band slotted waveguide antenna arrays with elliptical slots	[61]
Pottier *et al.*	2014	High pulsed power compact antenna for HPM applications	[48]
Chauloux *et al.*	2014	High gain and low losses antenna array for HPM applications	[53]

Author's	Year	Developments	Ref.
Yang *et al.*	2014	A beam steering antenna for X-band high power applications	[57]
Peng *et al.*	2015	Design of a concentric array radial line slot antenna for HPM applications	[47]
Arai	2015	Radial line slot antennas	[59]
Guo *et al.*	2016	Studies of a leaky-wave phased array antenna for HPM applications	[50]
Saleem *et al.*	2016	Optimization of linear antenna array for low SLL and high directivity	[54]
Yu *et al.*	2017	Design of a slot-coupled radial line helical array antenna for HPM applications	[46]
Zhao *et al.*	2017	All-metal beam steering lens antenna for HPM applications	[56]
Meng *et al.*	2018	X-band leaky waveguide antenna with high aperture efficiency and high power	[62]
Yong *et al.*	2018	Analysis of wide-angle scanning of HPM waveguide slot array antenna	[63]
Yu *et al.*	2018	Beam steerable array antenna based on rectangular waveguide for HPM applications	[60]
Boas *et al.*	2020	Low-profile high-gain slotted waveguide antenna array	[66]
Casula *et al.*	2021	A review on improved design techniques for high performance planar waveguide slot arrays	[64]

2.4 Research Gaps

a. For high energy pulse generation, pulse compression is usually carried out which could be done using various techniques discussed in the preceding

sections of this chapter. These techniques, however, are complicated in their design and thus difficult to implement. To overcome these difficulties a comprehensive study will be carried out to have a complete understanding of RF-Plasma interaction, so that the attained knowledge could eventually be employed for the devices meant for microwave pulse compression.

b. Transmission of RF pulses from an HPM system requires a specific design of an antenna, which is usually based upon a waveguide having dimensions determined by the target frequency. The design of an HPM antenna and its associated characteristics, as discussed in this chapter is a challenging task. Keeping in view the current trends in technology, a comprehensive study is proposed to optimize high power handling capability of a rectangular waveguide and its subsequent transmission. In addition, the optimized design based on a single element can be further extended to achieve array characteristics by designing a radiator having more than one element.

2.5 Summary

In this chapter, a historical perspective of microwave pulse compression, high power microwave antennas, their types and capacity is presented. For microwave pulse compression, the importance of plasma-microwave interaction is established. It has been discussed that traditionally a horn antenna with an appropriate feed structure was used, whenever it was necessary to transmit a high power signal. Because, by their very nature, waveguides are well suited to handle high power transmission. However, the horn antenna has limitations due to its structure, and it is relatively difficult to obtain beam sweep from a system involving a horn antenna. The chapter also discussed the radial helical array antenna, in particular its suitability for high power applications as well as the associated challenges. The chapter then introduced the leaky waveguide array antenna and its performance degradation, due to the mutual coupling of array elements and the presence of significant side lobe levels. Thus, causing limitations in the directivity of the

array. The high mutual coupling between array elements cannot be mitigated in an array configuration without changing its geometry. Therefore, it has been established that in a high-power array configuration, a new technique is required to achieve high directivity and reduced mutual coupling.

Chapter 3

A Novel Phase Reversal Technique for Microwaves Pulse Compression

3.1 Introduction

The newly compact SLED consists of a polarizer and spherical cavity, as the spherical cavity may resonate at degenerate modes with a phase shift of 90° at critical dimensions, while on the other hand, the polarizer is a key component behind such a compression system that makes these degenerate modes to resonate [67, 68]. It is a three-port device that first converts fundamental TE_{10} mode into TE_{20} mode. The mode is then transformed into TE_{11}, with a phase difference of 90° between them. The power of the incoming RF signal is equally divided between circulating TE_{11} modes. Further, these modes are injected into the cavity to store energy for a particular time period [69, 70]. Comprehensive research has been published regarding the phase reversal mechanism. Some methods employed in the literature include the silicon wafer-based technique in which the conductivity of the wafer is varied by exposing the laser beam [71, 72], changing the dielectric constant of a material by applying high voltage pulses [73], and the ferroelectric

module [74], among others. These techniques, however, are critical and difficult to handle as precise calculations are required with alignment.

The following sections propose a push-pull-based plunger to adjust the reflection coefficient by involving a mechanical variation in the cylindrical component of the polarizer. This reduces the size and removes the need for an additional phase reversal component, allowing for compactness and ease of design.

3.2 RF Polarizer Design

The RF polarizer is a key component of microwave pulse compression (MPC) systems and offers positive characteristics such as minimal loss and compactness. The mode conversion is also highly efficient and converts the input TE_{10} mode into two circular TE_{11} modes with a 90° phase separation. Based on functionality, the polarizer may be divided into three sections, i.e., TE_{10} mode section, over-mode section (TE_{10}−TE_{20}), and dual-circular TE_{11} mode section.

Initially, the RF wave is injected into a RF polarizer via Port I. In this case, the WR-284 standard waveguide size is used for operation in S-band, and the polarizer is designed to operate at a central frequency of 3 GHz. The primary resonating mode in this section is TE_{10}. This mode then reaches the overmode region and is converted into TE_{10} mode. Finally, a circular coupler is placed at the point where the modes are 90° apart from each other. The dimension of a polarizer is set in such a way that it must satisfy the following scattering matrix [75]:

$$S_{ij} = \begin{bmatrix} S_{11} & S_{12} & S_{13} & S_{14} \\ S_{21} & S_{22} & S_{23} & S_{24} \\ S_{31} & S_{32} & S_{33} & S_{34} \\ S_{41} & S_{42} & S_{43} & S_{44} \end{bmatrix} \tag{3.1}$$

$$S = \begin{bmatrix} 0 & 0 & 1/\sqrt{2} & i/\sqrt{2} \\ 0 & 0 & i/\sqrt{2} & 1/\sqrt{2} \\ 1/\sqrt{2} & i/\sqrt{2} & 0 & 0 \\ i/\sqrt{2} & 1/\sqrt{2} & 0 & 0 \end{bmatrix} \tag{3.2}$$

Eq. 3.2 states that there is perfect isolation towards the output port II, and 3 dB coupling between input and the two circular TE_{11} modes, while when power flows from a circular port, it must be equally divided into two rectangular TE_{10} modes at different ports. Fig. 3.1 shows a detailed description of a polarizer. It is the simplified setup of an RF polarizer with standard rectangular and circular ports.

The scattering matrix for 3 dB coupler/polarizer can be realized by solving the generic S-matrix given by Eq. 3.1. The 3 dB coupler matrix, under ideal conditions, shall have the form as defined by Eq. 3.3

$$S = \frac{\sqrt{2}}{2} \begin{bmatrix} 0 & 0 & 1 & i \\ 0 & 0 & -1 & i \\ 1 & -1 & 0 & 0 \\ i & i & 0 & 0 \end{bmatrix} \tag{3.3}$$

The above matrix, as stated before, represents the system under ideal conditions whereas, for a real system, it can be described by a matrix represented by:

$$S = \frac{\sqrt{2}}{2} \begin{bmatrix} 0 & 0 & e^{i\theta_1} & e^{i(\theta_1+\frac{\pi}{2})} \\ 0 & 0 & e^{i(\theta_2+\frac{\pi}{2})} & e^{i\theta_2} \\ e^{i\theta_1} & e^{i(\theta_2+\frac{\pi}{2})} & 0 & 0 \\ e^{i(\theta_1+\frac{\pi}{2})} & e^{i\theta_2} & 0 & 0 \end{bmatrix} \tag{3.4}$$

where θ_1 and θ_2 can have any arbitrary values. Eq. 3.4 represents a scattering matrix for left-hand circular polarizer and for right-hand circular polarizer, the scattering matrix shall be represented by Eq. 3.5 [76].

$$S = \frac{\sqrt{2}}{2}\begin{bmatrix} 0 & 0 & e^{i(\theta_1+\frac{\pi}{2})} & e^{i\theta_1} \\ 0 & 0 & e^{i\theta_2} & e^{i(\theta_2+\frac{\pi}{2})} \\ e^{i(\theta_1+\frac{\pi}{2})} & e^{i\theta_2} & 0 & 0 \\ e^{i\theta_1} & e^{i(\theta_2+\frac{\pi}{2})} & 0 & 0 \end{bmatrix} \tag{3.5}$$

By engaging the above theory 3 dB coupler/polarizer was designed in CST and its model is shown in Fig. 3.1. The section-wise view of the polarizer is depicted by Fig. 3.2. In order to achieve the scattering matrix characteristics, the width of the over-mode section ($TE_{10} - TE_{20}$) must lie between $\lambda < a < 3\lambda/2$, where, a is the width of the waveguide and λ is the wavelength of the desired frequency component. Similarly, for the circular port $\lambda/3.41 < R < \lambda/2.61$, where R is the radius of the circular coupler. CST Microwave Studio is used to optimize the dimensions of the polarizer and finally achieved the desired characteristics. The optimized dimensions for a, b and R are 72.14 mm, 34.04 mm and 76 mm, respectively.

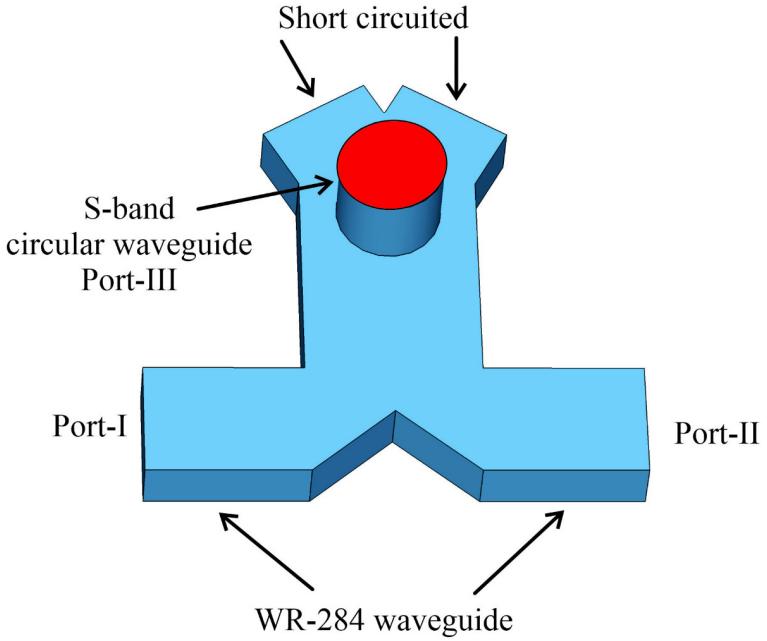

FIGURE 3.1: CST model of the designed RF polarizer.

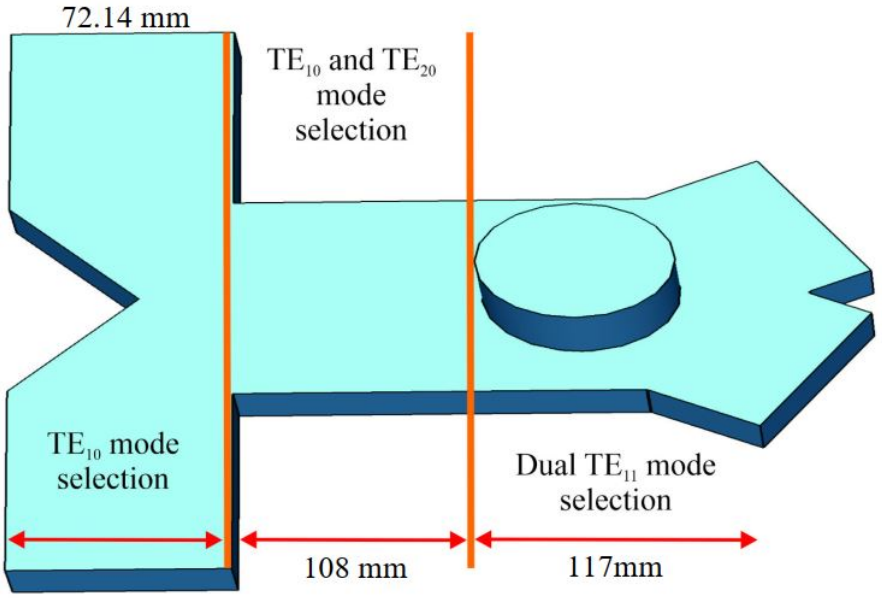

FIGURE 3.2: Section-wise overview of the designed RF polarizer.

3.3 Simulation Results

3.3.1 S-Parameters

The S-parameters and the phase response of the proposed RF polarizer are shown in Figs. 3.3(a) and 3.3(b). It is observed that the power fed from port-1 is equally divided between two TE_{11} modes (port-3), which are 90°apart from each other, and provides complete isolation with port-2. When power injected from the circular port, it equally divides into two rectangular TE_{10} modes at port-1 and port-2. The isolation between ports and modes is good enough to proceed further.

3.3.2 RF Polarizer with Variable Stroke

According to the transmission line theory, by varying the length of the short circuit stubs, the input impedance of the system changes, which directly affects the reflection coefficient. In the RF polarizer, there are two symmetrical cylinders, one of which is shorted whereas, the other one is meant to couple with while the spherical cavity as shown in 3.2. The shorted cylinder is free to vary. Therefore, by varying the length of the matching stub (see Fig. 3.4), the reflection coefficient

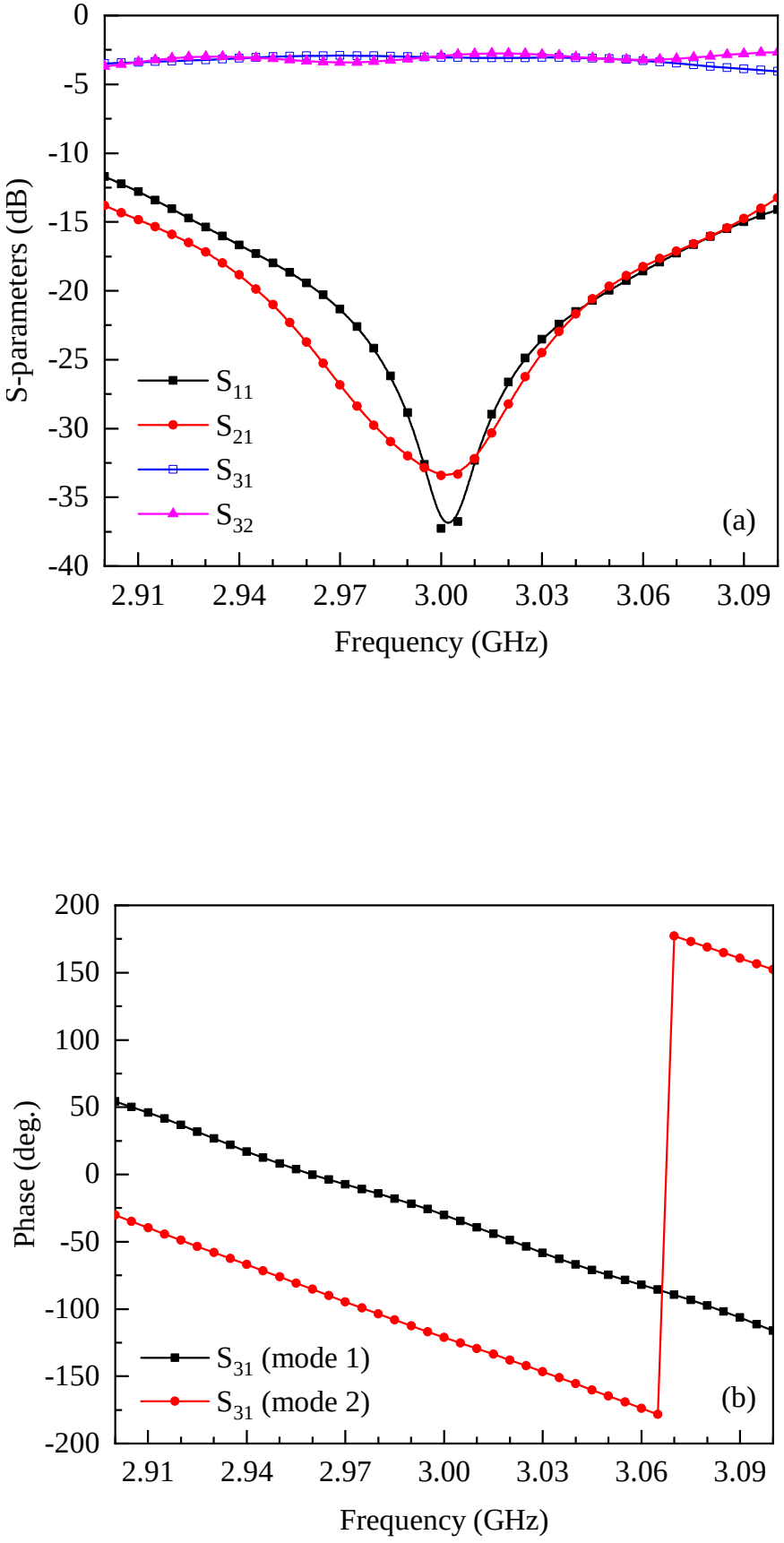

FIGURE 3.3: Simulated (a) S-parameters and (b) phase response of the designed RF polarizer.

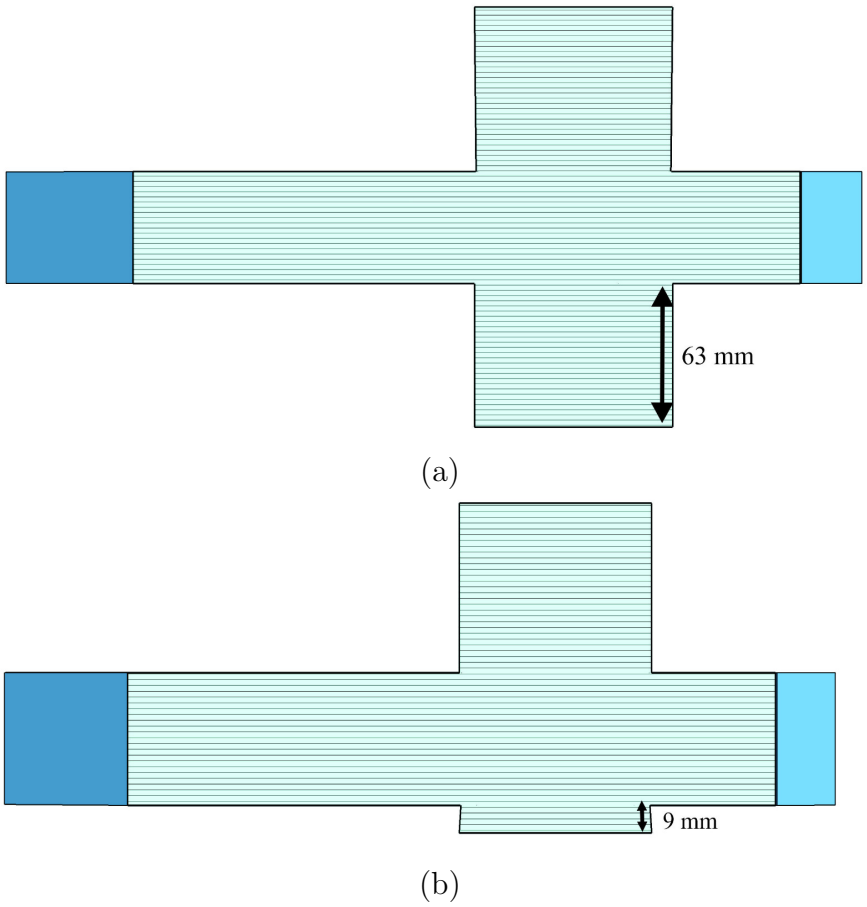

FIGURE 3.4: RF polarizer with variable stroke length (a) 63 mm and (b) 9 mm.

changes and signals start to couple at the coupling port. A variation from 9 to 63 mm stroke displacement, which corresponds to a difference of 54 mm, is required to obtain the discharging phase of the system, i.e., at 63 mm, the polarizer transfers energy to the cavity and acts as a storage phase, while at 9 mm, the polarizer couples the stored energy at port-2 [77]. Fig. 3.5 shows variation in S_{21} of the RF polarizer with variable stroke. It is observed that the magnitude of S_{21} is changed from -34 to 0 dB when the stroke length is decreased from 63 to 9 mm.

Fig. 3.6 shows the simulated S-parameters of the RF polarizer for stroke length of 9 mm. It is observed that the designed polarizer is able to resonate well in the S-band. In addition, the isolation between port-1 and port-3 is reasonably high, as observed in Fig. 3.6.

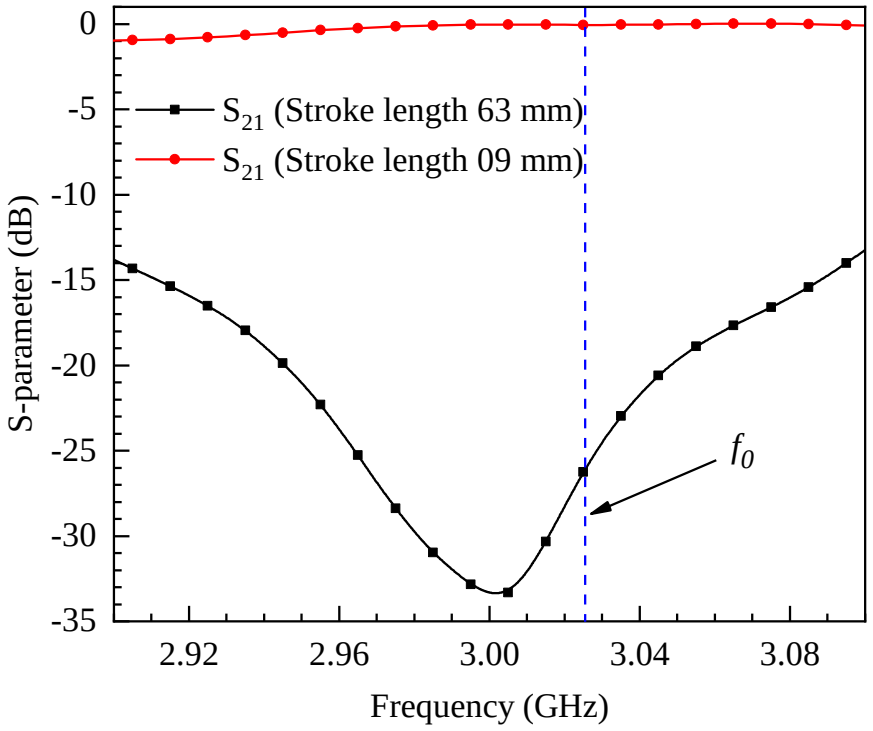

FIGURE 3.5: S_{21} of RF polarizer for two stroke lengths.

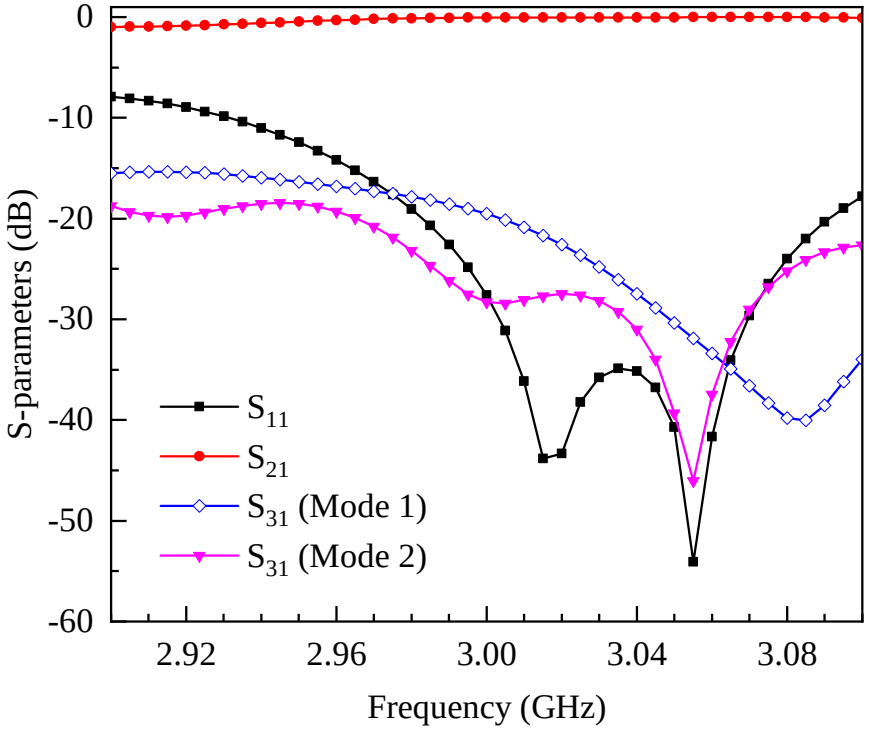

FIGURE 3.6: S-parameters of the RF polarizer for stroke length 9 mm.

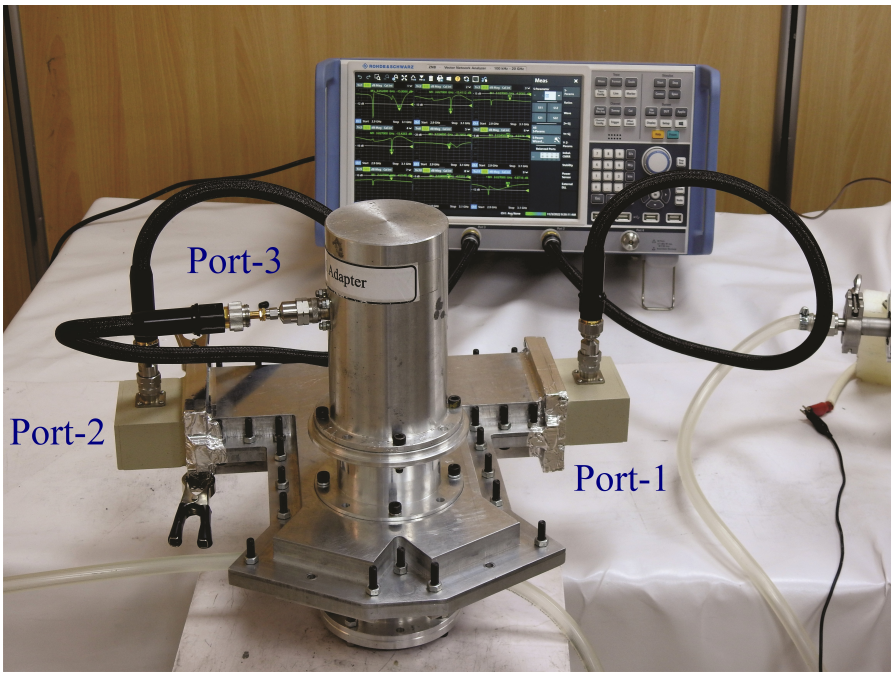

FIGURE 3.7: Fabricated RF polarizer without plunger connected with VNA.

3.4 Experimental Results

For validation of the simulation result, a prototype of an S-band RF polarizer is fabricated. The body of the RF polarizer is casted from aluminum in two parts and combined together through nuts and bolts. A cold test is performed using the Rhode & Schwarz Vector Network Analyzer ZNB (100 kHz−20 GHz). Fig. 3.7 shows the fabricated polarizer connected to the VNA without the plunger, which shows the charging state. Port-1 is input, port-2 is output, and port-3 is a circular port for cavity charging and discharging. All ports were connected through VNA in balanced configuration i.e. RF signal of equal phase and amplitude in order to analyze the performance of 3 ports polarizer thoroughly.

The magnitude of the scattering parameters vs the frequency of all three ports is shown in Fig. 3.8. In the measurement setup, the frequency span is set to 60 MHz ranging to 3.05 GHz. According to measurement results, the observed values of S-parameters at 3.028 GHz are: $S_{11} = -24.67$ dB, $S_{21} = -13.22$ dB, and $S_{31} = -3.67$ dB. There is a frequency shift of 20 MHz between the measured (3.028 GHz) and designed (3 GHz) values due to fabrication tolerance. Comparing the

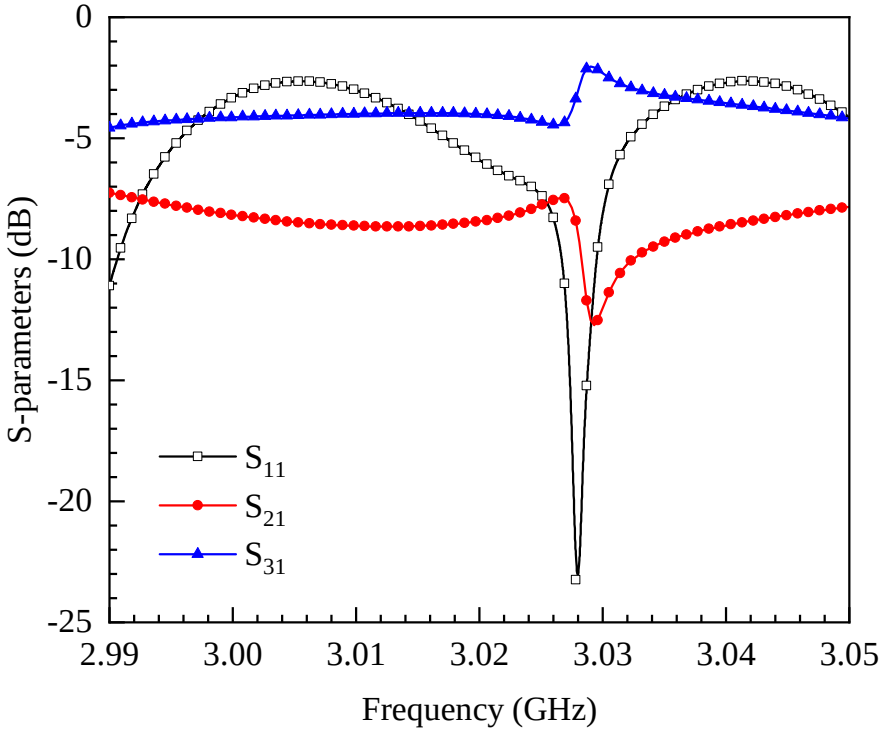

FIGURE 3.8: Measured S-parameters of the RF polarizer without the insertion of plunger.

data of Figs. 3.6 and 3.8, there is slight discrepancies in scattering parameters which can be attributed to the resistivity of aluminium.

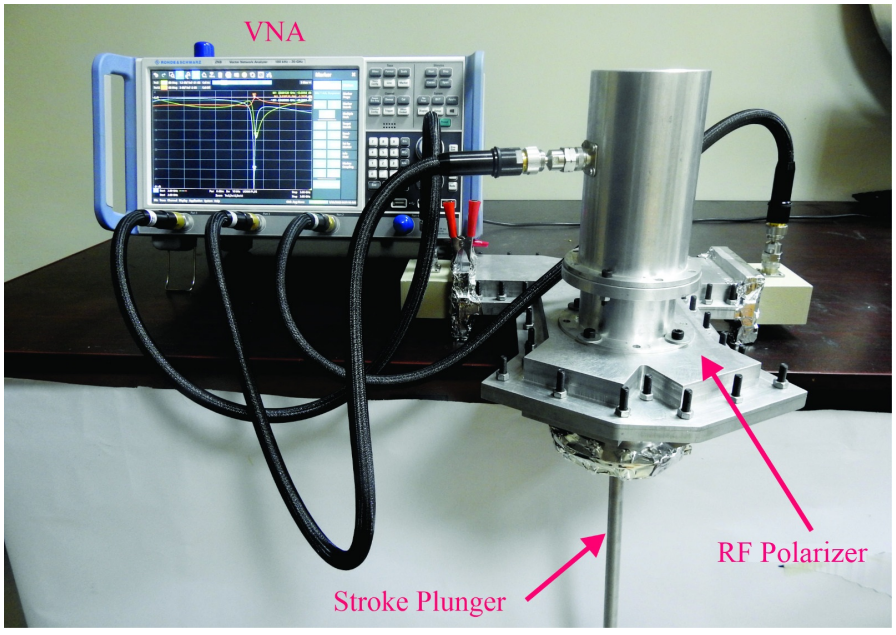

FIGURE 3.9: Fabricated RF polarizer with plunger connected with VNA.

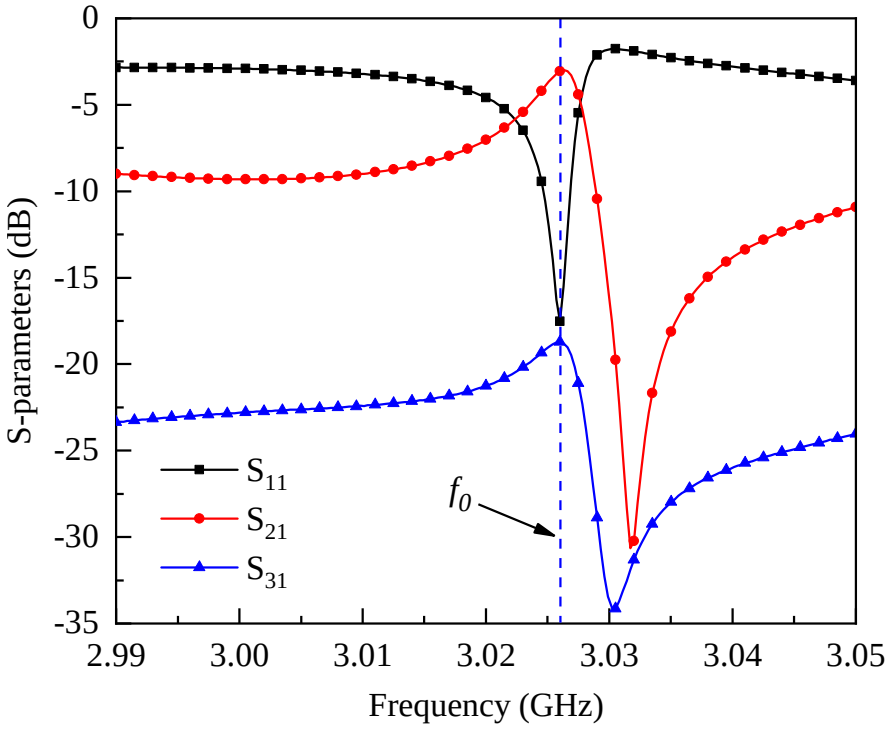

FIGURE 3.10: Measured S-parameters of the RF polarizer with the insertion of plunger.

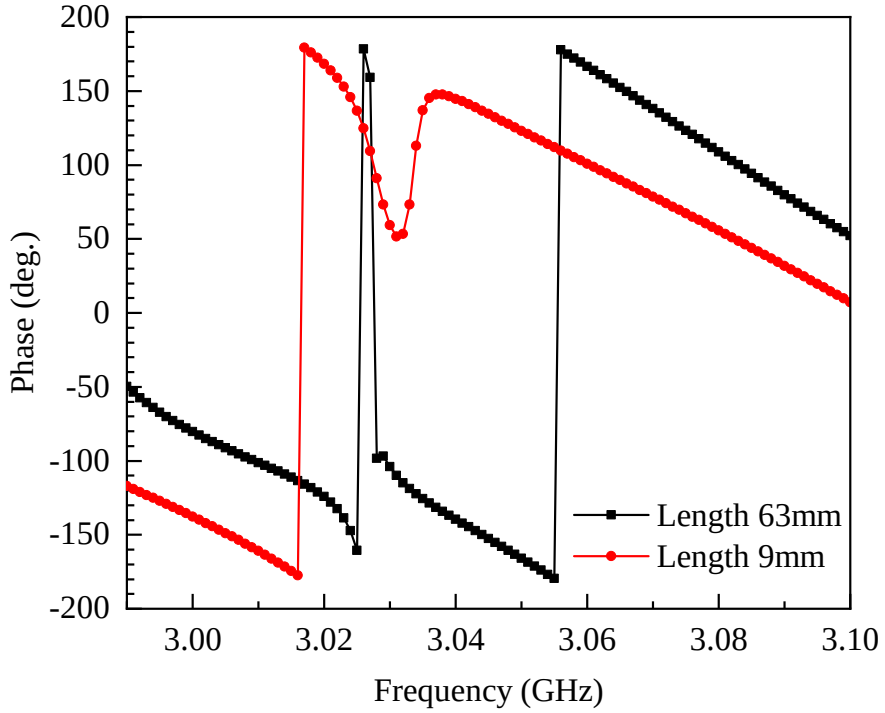

FIGURE 3.11: Phase response of the RF polarizer for different plunger positions.

Fig. 3.9 shows the fabricated polarizer connected to the VNA with a plunger. The position of the plunger is set at 9 mm. The measured S-parameter values are noted

to be (see Fig. 3.10): $S_{11} = -17.5$ dB, $S_{21} = -3.22$ dB, and $S_{31} = -19.67$dB, which show that all the power from port-1 is delivered to the output port (port-2), while port-3 is isolated. Fig. 3.11 shows the phase difference between plunger positions at 63 mm (charging state) and 9 mm (discharging state). The phase difference is ≈180°at 3.028 GHz.

3.5 Summary

The RF polarizer is considered the backbone of an MPC system because it allows the system to store RF energy in the cavity. The unique phase inversion characteristic achieved through the RF polarizer allows the cavity to discharge efficiently to achieve high RF peak power; resulting in a high gain and a high $Q-$ factor.

This chapter presents a design of an RF polarizer with variable stroke length response; to achieve the desired phase reversal and reflection coefficient in order to compress the RF pulses successfully. A cold test is performed with a plunger by varying the stroke length. The results of the experiments are in good agreement with those of the simulations.

Chapter 4

RF-Plasma Interaction with Low Pressure DC Glow Discharge

4.1 Introduction

Plasma has gained widespread use in recent years, with applications ranging from commercial industry to defense applications [25]. One of the significant ways plasma is applied HPM systems is by utilizing its ability to behave as a high-frequency switch. Plasma sources are able to operate both in continuous and repetitive or pulsed operating conditions, allowing narrow or wide charge particle beams to be formed. Due to fast response times, a plasma switch can be used in MPC systems to reflect RF waves, enabling high-power discharge [78].

Different types of gas discharge can be used for plasma generation, such as cold-cathode glow discharge, arc-type discharge, triggered discharge, high-frequency discharge, etc. The design process for each application requires different characteristics in the plasma. While it is possible to generate plasma at atmospheric pressure, most applications utilize a low vacuum ($1-1000$ Pa) for the plasma source. Some important things to consider are the conductivity, the frequency of the plasma, the frequency of the collisions, and the permittivity in both the longitudinal and radial directions. Most of the time, there are only two ways to

make plasma: with an electrode or without one. The former uses a voltage for excitation, and the latter is generated with high-power RF.

In the first method, DC excitation is more common than others. This is in contrast to RF-plasma, which is generated by exposing a plasma tube to a high-power RF signal generated by a suitable device, e.g., Klystron. Notable applications of this interaction are plasma antennas [79] and plasma torches [21]. In this chapter, the DC-excited plasma switch is developed. The plasma is created by applying a DC voltage over the gas-filled gap between two electrodes. Such DC discharge has been the subject of intensive research for decades. The DC discharge and, in particular, the DC glow discharge have been historically important both for studying the properties of the plasma as well as for the various applications where the DC discharge is used to provide a weakly ionized plasma. DC discharge can be used as a light source, as a gas laser, as an electron source for Hall thrusters, as a pixel in a plasma display panel, or as a tool for sputter deposition [80, 81].

The interaction of plasma with microwave depends upon many factors like thickness of plasma, its frequency and response time etc. In 2022, Omran *et al.* [82] used the plasma as an RF switch with self-triggering characteristics in order to protect the Radar system. In 2022, Ghosh *et al.* [83] proposed self-aware dynamic mesh refinement technique to study the non-linear, multi-physics and multi-scale natures of plasma. Anitha *et al.* [84] in 2022, experimentally studied the dense plasma whose plasma frequency was greater than incident microwave frequency to observe the electromagnetic wave absorption.

Desai *et al.* [85] presented a deep learning model of plasma interaction with microwave by employing convolutional neural networks method in which the absorption and reflection of microwave propagation were studied. In 2020, Wilson *et al.* [86] investigated Laser triggered plasma interaction with microwave to achieve microwave pulse compression. Yao *et al.* [87] developed plasma metal model to study the interaction of microwave with plasma at low temperature. In [88, 89], a study was conducted to observe the effect of high power sub-nanosecond microwave pulses on plasma filled cylindrical waveguide which form Wakefield's.

This chapter pertains to the practical formation of plasmas, with a focus on plasma interaction with EM waves. In the case of high-power microwave systems, plasmas are either used to absorb the EM wave or reflect it. Both cases exist under different circumstances, which will be discussed in the following. Section 4.2 describes the behavior of the interaction between RF waves and plasma. Furthermore, section 4.3 shows simulations of the discharge tube as conducted in Magic3D and COMSOL Multiphysics for plasma characterization and interaction visualization. Section 4.4 shows experimental testing of RF-plasma interaction, and results are compared to the simulated values.

4.2 RF-Plasma Interaction

Plasma is characterized by the number of ions per unit volume oscillating at certain frequency. Depending on this density and the frequency, a wave might be reflected, absorbed, or transmitted by the plasma medium. This behaviour of interaction between RF (ω) and a plasma frequency (ω_p) is determined by the permittivity of the plasma medium. The effective permittivity (ϵ_e) can be defined for a uniform plasma region as:

$$\epsilon_e = \epsilon_0 \left(1 - \frac{\omega_p^2}{\omega^2}\right) \tag{4.1}$$

where,

$$\omega_p = \sqrt{\frac{n_e q^2}{m_e \epsilon_0}} \tag{4.2}$$

where q is the charge of the electron, m_e is the mass of the electron, n_e is the number of ionized particles per unit volume, and ϵ_0 is the permittivity of free space. By studying the solution of Maxwell's equations for plane wave propagation in such a medium [90], it can be shown that wave propagation through a plasma is only possible for $\omega > \omega_p$ [80]. Lower-frequency waves will be reflected. If a magnetic field is present, the plasma becomes anisotropic, and the analysis is more complicated. However, magnetic field-focused plasmas are outside the scope of this research.

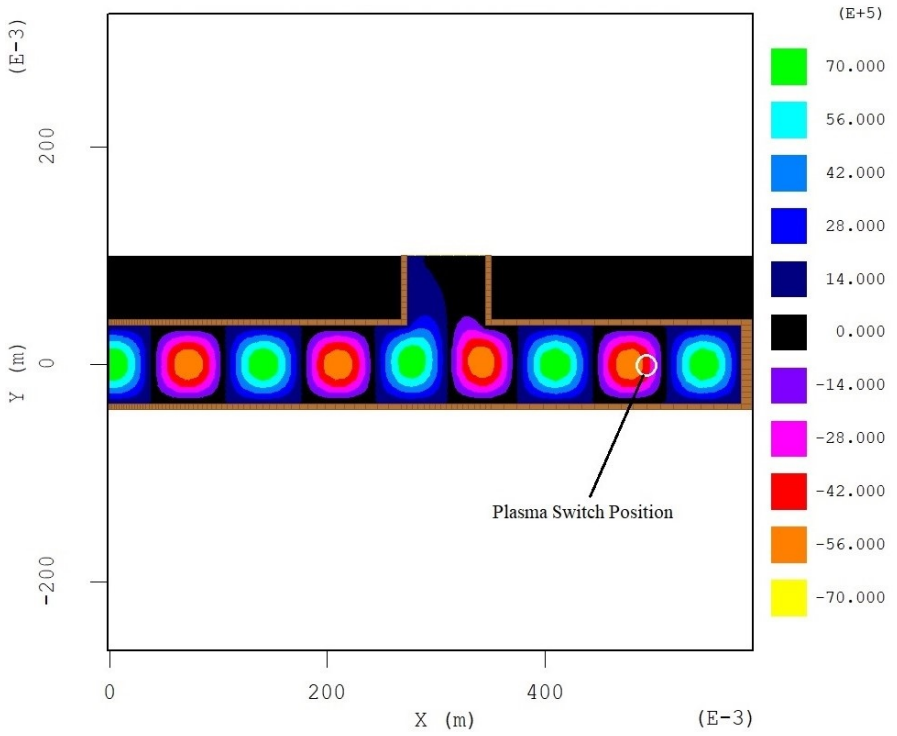

FIGURE 4.1: Interaction between standing RF waves and beam switch.

RF-plasma interaction can be visualized through simulation (see Figure 4.1). By injecting an RF wave into a structure with a plasma column in its path, we can check the interaction behavior. This behavior is observed in Magic3D, where a simple waveguide structure for an S-band wave is constructed. Figure 4.1 shows a two-dimensional (2-D) cross section of a WR-284 waveguide with a switch placed near the boundary. When the waveguide is excited, a standing wave is established in the waveguide when the switch is in the off-state. There is almost no power going towards the upper open port of the waveguide. When the plasma switch is activated, it acts as a metallic obstacle in the path of the EM wave and creates a short at the switch position. Resultantly, the EM wave reflects back from this switch, as shown in Figure 4.2. Now, as we can see from Figure 4.2, almost all the stored power is going towards the output port of the waveguide. This is the fundamental interaction between a plasma column and an EM wave, which we have aimed to replicate via the use of a plasma tube placed within a waveguide.

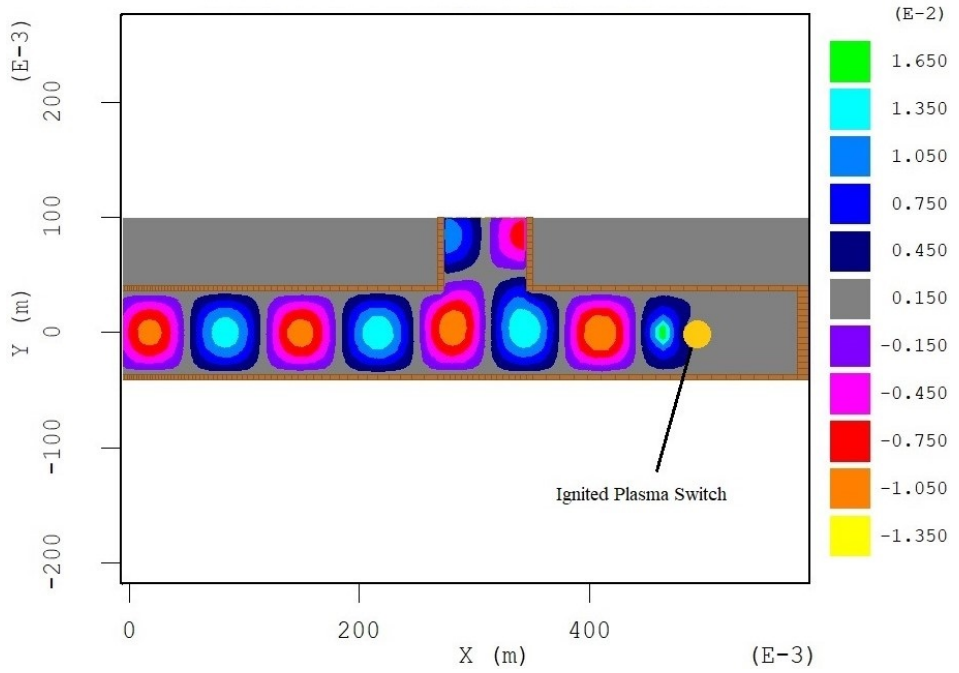

FIGURE 4.2: Standing wave reflection after RF-beam interaction.

4.2.1 Discharge Tube

Applying a DC voltage over the gas-filled gap between two electrodes in a discharge tube produces the plasma. To keep the discharge going, there has to be a few hundred volts maintained between the cathode and anode. The working gas pressure, composition, working gas type, applied voltage, and discharge profile all affect the kind of discharge that develops between the two electrodes. Electric current flowing through a gaseous medium is referred to as a gas discharge. The DC glow discharge manifests itself in the discharge current range of A to mA and in the pressure range of $0.5-1000$ Pa. Some of the gas's atoms and molecules must be ionized for discharge to take place. Additionally, this current requires an electric field to be driven. The discharge must have constant current flowing through it for the entire length of the discharge tube. Ions and electrons produced in the plasma volume, as well as electrons emitted from the cathode, drive the current in a DC discharge.

The diverse plasma species do not all have the same temperature because the various particles are typically not in thermal equilibrium. In particular, the electrons

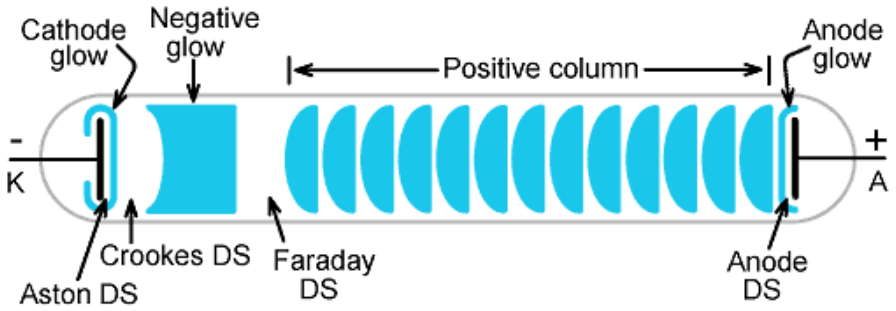

FIGURE 4.3: Schematic of DC glow discharge showing several distinct regions that appear between cathode and anode.

can be readily accelerated to the high energies necessary to excite and ionize neutral atoms or molecules due to their low mass. Therefore, the temperature of the electrons is substantially higher than that of the heavier particles (ions, atoms, and molecules), or $T_e >> T_i, T_g$, where T_e is the electron temperature, T_i is the ion temperature, and T_g is the neutral gas temperature.

The gas pressure is a significant factor affecting the temperature of the plasma species and the thermal equilibrium between species. Few collisions happen at low pressure, and the transmission of energy between species is ineffective. The numerous collisions between the different plasma species that take place under high pressure lead to more evenly distributed temperatures between the species. A very distinctive appearance can be seen in the low-pressure DC glow discharge, which is shown in Figure 4.3.

An electrically conductive metal is generally used to create the cathode. Utilizing secondary electron emission, the cathode's electrons are used to keep the discharge going after a favorable ion bombardment of the cathode surface. The positive column occasionally exhibits prominent and regular luminous striations, which may be stationary or moving down the length of the tube. In a DC glow, the stratification of the column moves in alternating bright and dark regions. In molecular gases (such as hydrogen, nitrogen, and oxygen) and mixtures of molecular and rare gases, standing striations can be seen with the bare eye [91]. The primary dark space, also known as the Aston dark space, is located in front of the cathode and is where the secondary electrons are gathered. The cathode glow, which has a comparatively high ion density, is located next to the Aston dark space. At this

point, the secondary electrons start moving very quickly away from the cathode. The cathode begins to glow as these high-energy electrons begin to collide with neutral gas atoms at a distance from the cathode corresponding to the mean-free path.

The working gas and the cathode material can both be identified by the hue of the light that is produced. The type of gas and gas pressure affect the axial length of the cathode glow. Following the cathode glow is the cathode's (Crookes or Hittorf) black space, which has a moderate electric field and a positive, relatively high-density space charge. The positive ions are likewise driven in this area toward the cathode. Since ions have far lower mobility than electrons, they make up the majority of this dark area. The negative glow is followed by the black space of the cathode. The light intensity of the discharge's negative glow is the brightest. In this area, excitement and ionizing collisions result from the secondary electrons' acceleration. The current is virtually exclusively carried by electrons in this situation, and there is a low electric field.

4.3 Plasma Study and Simulation Results

For this study, we selected Argon as the medium for plasma generation due to its characteristics of easy ionization and uniform plasma. For an argon column, we can use COMSOL simulation to determine the electron density in the switch with appropriate simulation parameters. The column is designed as follows: A 100 mm long tube defined as a dielectric material boundary is defined with two long metal inserts on both ends of 12 mm each, with one defined as an anode and one as a cathode. The physical parameters are given in Table 4.1. Reduced electron mobility characterizes how quickly an electron can move through a solid material when pulled by an electric field. Work function represents the minimum amount of energy required to pull an electron out of any emitter, like a cathode. These parameters will also be utilized for the simulation.

TABLE 4.1: Simulation parameters for plasma column.

Parameter	**Value**
Axial lengh of tube	100 mm
Plasma column length	76 mm
Pressure	3.8 Torr
Reduced electron mobility	1.25×10^{24} $(\text{mVs})^{-1}$
Work function	5 eV
Temperature	20 °C

The plasma column is simulated according to parameters that are experimentally feasible. COMSOL Multiphysics is utilized, which offers in-depth study with its plasma module. The schematic of the plasma module with labeled components is shown in Figure 4.4. Most published literature discusses five types of reactions in the plasma. They include ionization, excitations, eliminating excitations, elastic collisions, and attachments. The following types of interactions are possible in all five types of reactions: 1) electrons and neutral molecules; 2) electrons and ions; 3) ions and neutral molecules; 4) neutral–neutral molecules; and 5) surface and wall recombinations. The gas considered in our simulations is Argon (Ar). We can excite Ar with simple mechanisms at low pressure.

Plasma chemistry is governed by a set of ionization equations that show the behavior of the selected gas in a plasma state. For an Argon medium, there are both elastic and inelastic (e.g., ionizing) collisions occurring during the plasma generation process. For instance, the ionization potential of Argon gas is 15.8 eV, which is an intrinsic property. During the ionization process, Argon also enters a metastable state, where it leads to the excitation of other Argon atoms (known as Penning ionization), which also contributes to the plasma density [92]. The reaction process is intrinsic to the species (in this case, Argon) and does not rely on the physical geometry of the tube. These equations, along with reaction types and reaction energies, are given in Table 4.2.

In Table 4.2, Ars represents an Argon atom in an excited state, while Ar^+ shows an Argon ion. With physical and chemical parameters (see Tables 4.1 and 4.2),

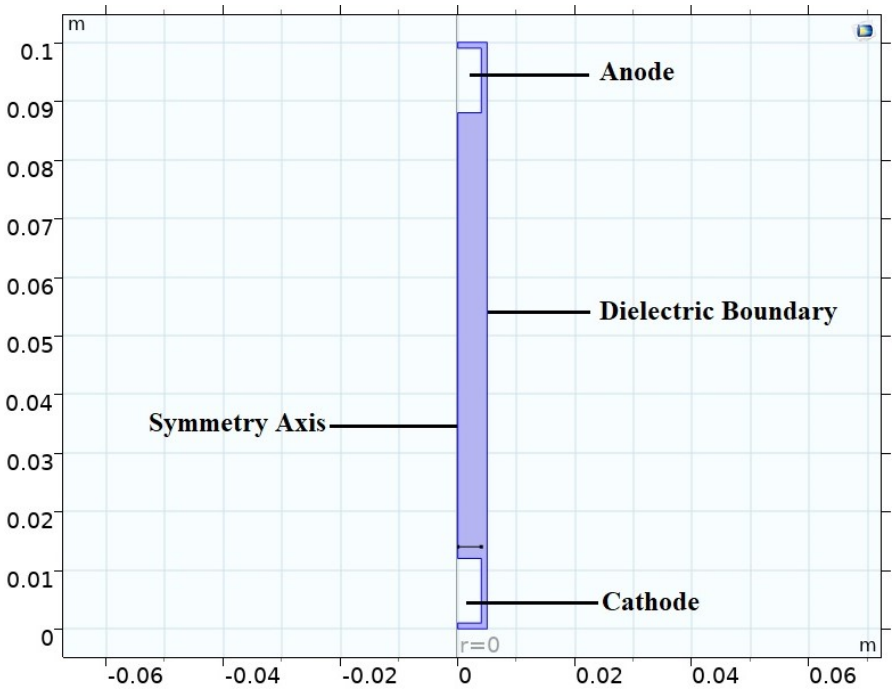

FIGURE 4.4: Schematic of plasma column.

TABLE 4.2: Modeled collisions and reactions.

Reaction	**Formula**	**Type**	$\Delta\epsilon$ **(eV)**
1	e+Ar $\geq$ e+Ar	Elastic	0
2	e+Ar $\geq$ e+Ars	Excitation	11.5
3	e+Ars $\geq$ e+Ar	Super-elastic	-11.5
4	e+Ar $\geq$ 2e+Ar$^+$	Ionization	15.8
5	e+Ars $\geq$ 2e+Ar$^+$	Ionization	4.24
6	Ars+Ars $\geq$ e+Ar+Ar$^+$	Penning Ionization	–
7	Ars+Ar $\geq$Ar+Ar	Metasbale Quenching	–

the tube is simulated for $t = 1$ s. From the simulations, it is observed that the potential across the switch becomes uniform when plasma is generated, as shown in Figure 4.5. However, the plasma density is not uniform (at 500 V). The density is concentrated near the cathode, in the dark space region (see Figure 4.6).

This electron density is plotted across a range of voltages using a parameter sweep. The range is selected as $400-700$ V with an interval of 50 V. It is observed that an increase in voltage corresponds to an increase in electron or ion density, as shown

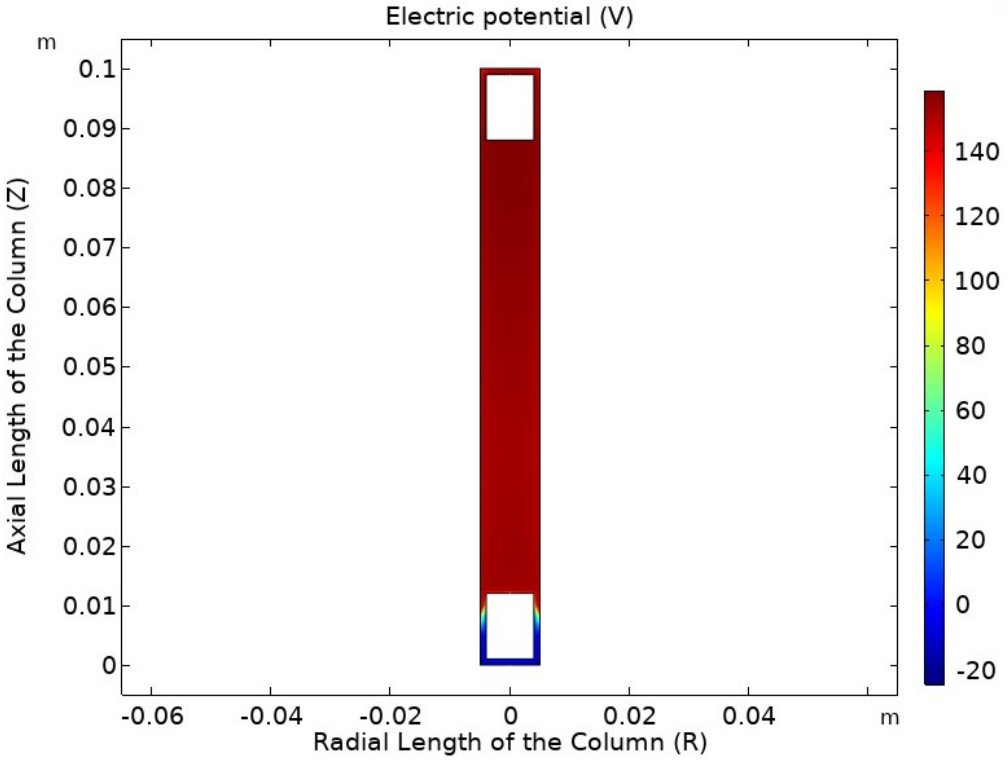

FIGURE 4.5: Visualization of constant voltage across the plasma column.

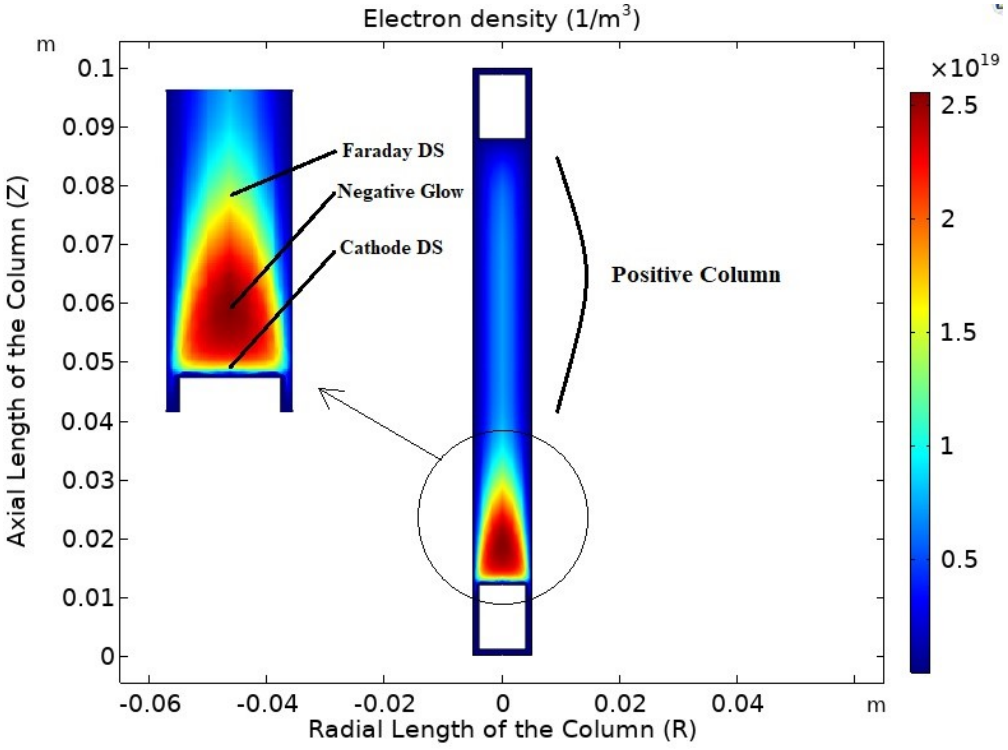

FIGURE 4.6: Visualization of plasma column at 500 V.

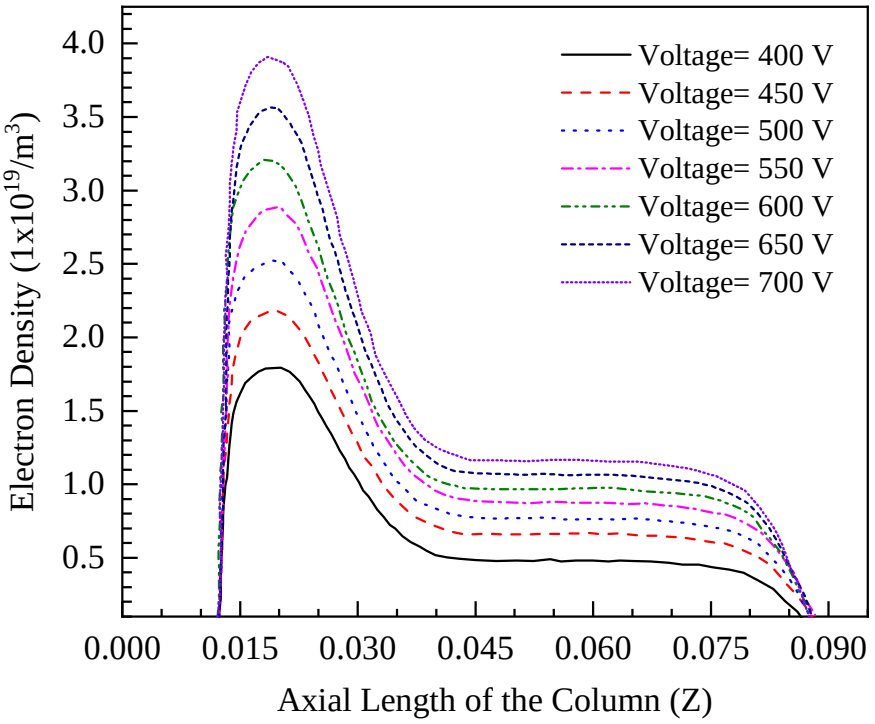

FIGURE 4.7: Electron density plots for a voltage sweep of 400 V to 700 V.

in Figure 4.7. The curve is plotted against the axial direction and shows the peak plasma density near the cathode, within the Faraday dark space.

For our case, as per the experimental study, we select 500 V as the operating voltage, which corresponds to an electron density of $n = 2.5{\times}10^{19}$, which corresponds to a plasma frequency of 7.1 GHz. We compare this with experimental results in the following section.

4.4 Experimental Setup and Results

The gas discharge tube is made of glass and has an inner diameter of 15 mm and a length of 100 mm. The electrode gap is set to 80 mm, and the pressure in the tube is maintained at 3.8 Torr. Gas tube operation follows Paschen's law. Electrodes are connected to a high-voltage supply via a high-voltage cable rated for 100 kV. Vacuum pressure is monitored using an Agilent FRG730 digital vacuum gauge. The vacuum assembly is connected via KF fittings and flanges.

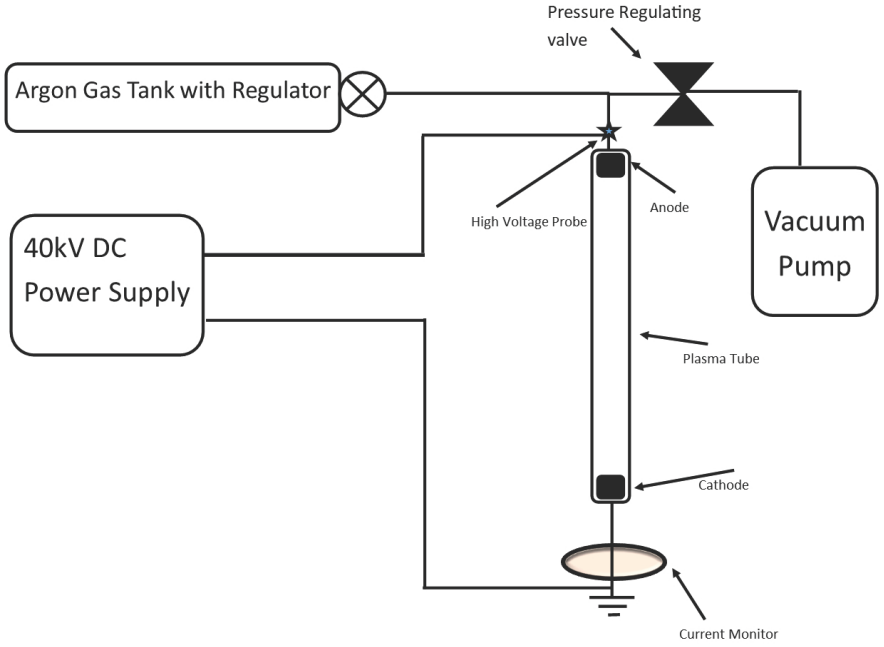

(a)

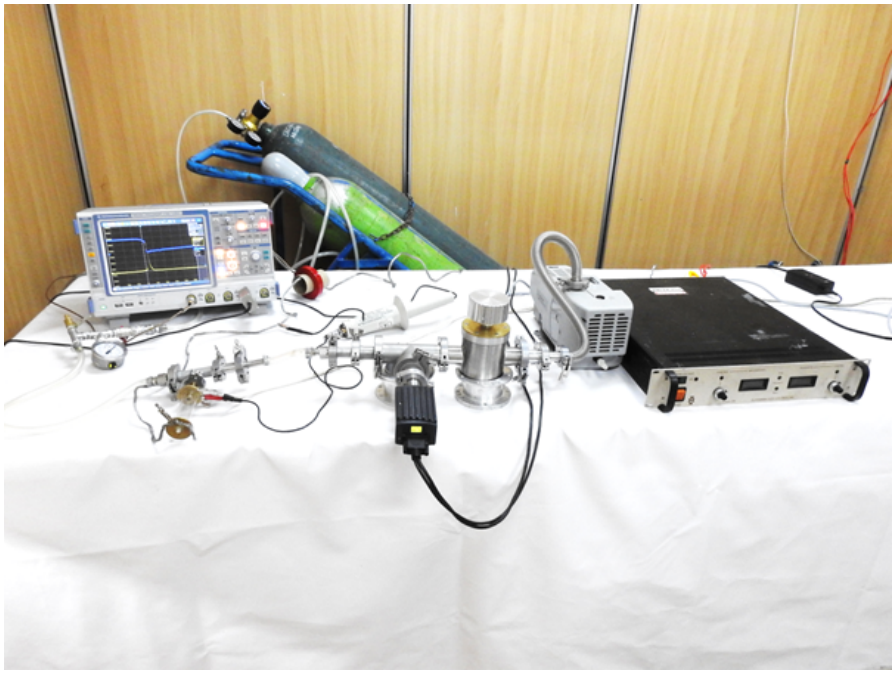

(b)

FIGURE 4.8: (a) Schematic of experimental setup. (b) Experimental setup with vacuum pump, Argon tank, pressure gauge, and high voltage DC power supply connected to a plasma tube.

The switch is connected to a 30 kV DC power supply with a maximum current rating of 30 mA. A rotary pump is connected to the tube on one side, and the other side is fed with Argon. Vacuum and gas pressures are controlled using a regulating valve at the inlet of the tube. The schematic of the experimental arrangement is

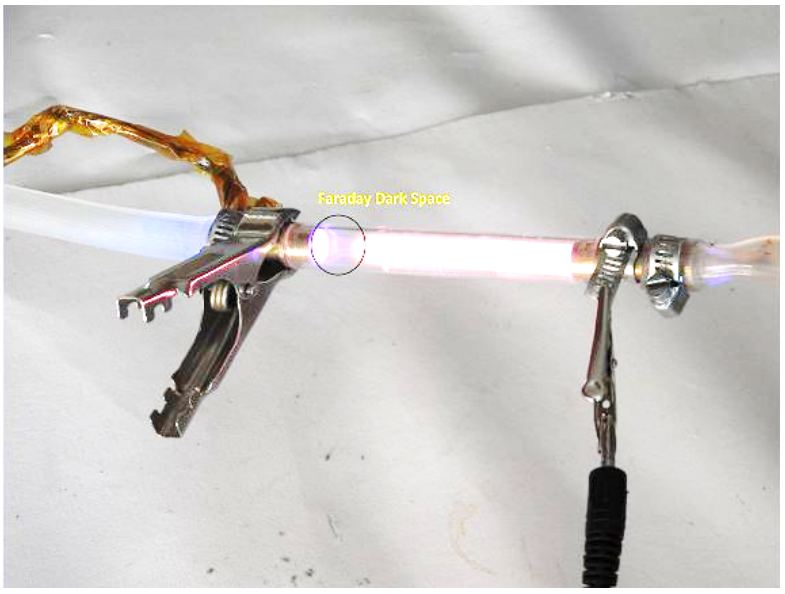

FIGURE 4.9: Experimental demonstration of DC glow discharge.

shown in Figure 4.8a and the complete experimental setup is shown in Figure 4.8b.

The generated plasma tube is shown in Figure 4.9. As can be seen, the positive column and Faraday dark space are visible in the tube. When the breakdown voltage is achieved, a bright glow is produced. If the gas flow rate is increased further, it quenches the plasma channel and arcing is produced. The flow rate is maintained beyond this level to achieve stable DC glow discharge. The voltage and current characteristics are measured using a high-voltage probe (model Tektronix P6015) and a current transformer (model Bergoz coil CT-F1.0), respectively. Furthermore, the frequency characteristics of the tube are diagnosed using a Keysight E5071C network analyzer. To validate the RF-plasma interaction, a wideband signal (2.90 GHz–3.06 GHz) is applied from the network analyzer. The tube is placed in a hollow circular waveguide with a coaxial RF adapter on both sides. The network analyzer is set to measure the magnitude and phase of the reflection parameter S_{11}. The plasma column is ignited to measure the difference between RF on-state and off-state.

The voltage response of the tube is shown in Figure 4.10a. With an input voltage of 6.5 kV, the switch enters self-break mode, and the value reaches 500 V at steady state. Similarly, the current response exhibits the opposite trend, reaching a steady state value of peak supply current of 30 mA (see Figure 4.10b).

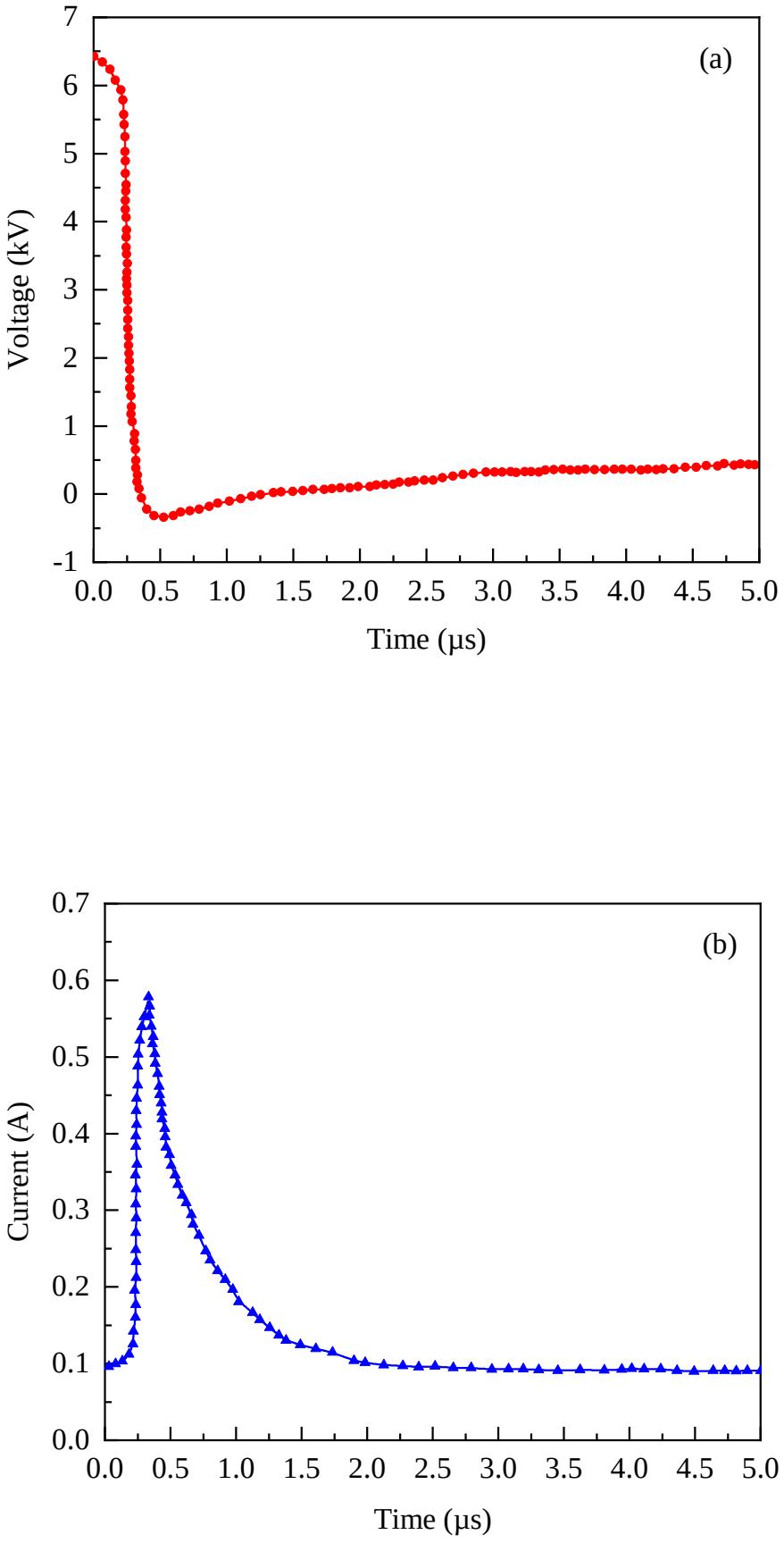

FIGURE 4.10: Experimentally obtained (a) voltage and (b) current response of plasma tube.

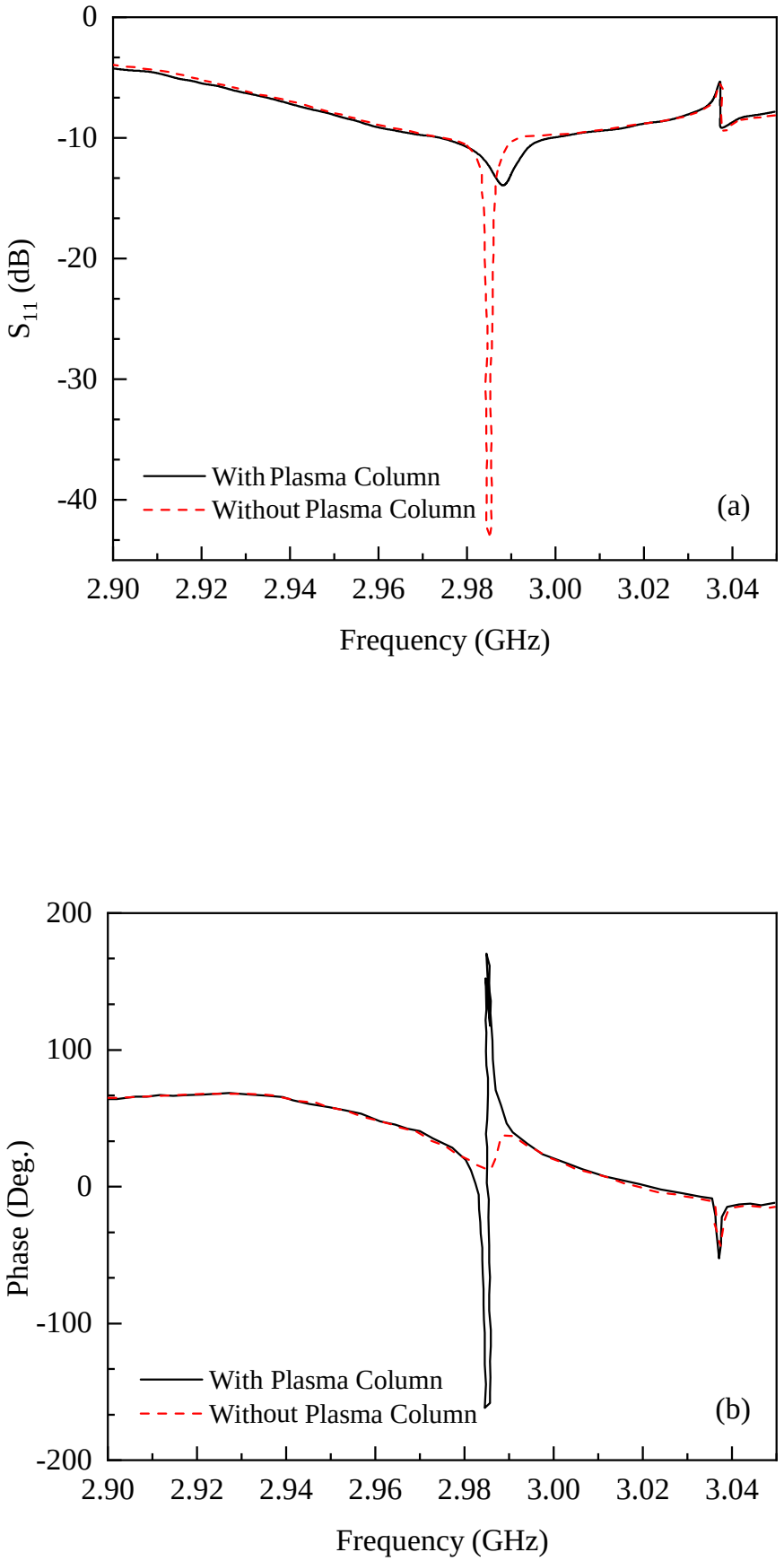

FIGURE 4.11: (a) Magnitude and (b) phase response of S_{11}.

The S_{11} response of the RF-plasma switch is shown in Figure 4.11a, which shows that the magnitude of S_{11} is increased when the switch is ignited. The value goes from -40 dB in the switch off-state to -13 dB when the switch is ignited, corresponding to a difference of 27 dB. This shows that the plasma column can reflect the RF signal, which proves that the plasma frequency is greater than RF signal. Similarly, the corresponding phase at the same frequency is observed and shown in Figure 4.11 (b). The on and off-state conditions of the tube cause a 180° phase shift in the S_{11}.

4.5 Summary

In this chapter the significance of RF-plasma interaction and its theoretical understanding is discussed. The interaction behaviour is observed in Magic3D and a simulation study of argon plasma generation with the required characteristics is performed in COMSOL. It is calculated that the plasma density, observed through simulations, results in a plasma frequency of 7.18 GHz. This plasma frequency reflects lower-frequency band, which in our case is the S-band (3 GHz). Experimental testing is conducted with low-pressure, argon-filled glass tubes of the given specifications. The plasma is sustained at 500 V, with the tube placed in a cavity between two coaxial waveguide adapters. A network analyzer is used to determine the effects of the plasma on the input RF. Results show a difference of 180° in phase shift and a 27 dB difference in reflected magnitude.

Chapter 5

Spherical Cavity for Pulse Compression

5.1 Introduction

High power microwave (HPM) devices are used in multiple scientific and industrial applications including particle accelerators, communication, and defense technology. There are many HPM systems used globally, with industrial, research, medical and defense applications. A modern high-power microwave system requires electro-vacuum or vacuum electronic microwave devices with an output pulse power exceeding 100 MW, generally at GHz−THz range of frequencies. Multi-GW power has been obtained with particle energies exceeding 1 MV at tens of kA currents for longer wavelengths [3], which is only possible with careful designing and precision manufacturing. One such device of interest is the magnetron oscillator, which has high power efficiency and is capable of MW-range power operation. However, in magnetrons, pulse power of this order is achieved with anode voltage of hundreds of kilovolts (320−450 kV), so application of such devices are often limited with size and bulk of their power supply sources, and large sized device geometries. It is therefore favourable to not only improve device efficiencies but also consider the electrical properties of the device. A lower anode voltage is favourable as it reduces

power supply constraints and heating issues. It also improves device reliability, since low anode voltages cause reduced electric stress on dielectric and, therefore, higher reliability during operation [4]. The stringent demands of these applications are translated directly to the requirements for RF source parameters, thus, increasing the cost and complexity of the devices. RF pulse compression is often utilized to alleviate this cost by transforming a low power long pulse input signal into a higher power short pulse output [5–7]. This process reduces the required power output of the source; allowing for the implementation of a cheaper and a more efficient device.

The basic operation of such a system includes charging the system with a long duration, high energy wave. With the use of a suitable switching mechanism, the wave is quickly discharged to achieve higher power of a shorter duration. This principle greatly reduces the physical requirements of the system. The use of a metal waveguide as a dispersive medium to generate high peak-power microwaves was proposed in [3]. The principle is to use a swept frequency modulated pulse train with a monotonically increasing group velocity propagating through the waveguide. The tail of the pulse will overtake its leading edge, which results in pulse shortening and growth in power amplitude, if the losses are small. From the dispersion curve of the smooth waveguide, the group velocity has a large change near the cut-off frequency and the group velocity changes less at the frequencies further away from the cut-off frequency. Therefore, most of the frequency range suitable for the pulse compression is near the cut-off [33]. However, the large ohmic losses close to cut-off prevent a high compression ratio, resulting in low energy efficiency.

Generally, structures with specialized properties are used in lieu of smooth waveguides to improve energy efficiency of the system. The pulse compressor which is widely used in the linear accelerators is of importance to increase the power efficiency of the klystron RF power and the accelerating gradient. Unlike the traditional SLED type pulse compressor, a barrel open type cavity (BOC) is composed of a single barrel open cavity and a matching waveguide. Due to the low power loss on the inner surface, BOC has a high unloaded Q $>$ 90,000. The system

was simulated for compressing a 3 μs pulse into 330 ns, with a max output power rated at 50 MW.

Besides using the spherical cavities as energy storage elements, resonant cavity pairs of the cylindrical structure have been adopted since the first SLED [35]. Given the nature of the low cross-polarization field, low loss, and wide bandwidth, the corrugated cylindrical structure has also been applied to waveguides as transmission lines for several decades [36], and the helically corrugated waveguides have been used as a dispersive medium to compress frequency-swept pulses [33, 37]. One such research uses a corrugated cylindrical structure as an energy storage element is parented in [2]. It shows an X-band (11.424 GHz) cavity with a high unloaded Q-factor ($>$ 100,000). The power from the klystron keeps filling in the corrugated cylindrical cavity until the microwave pulse phase is reversed, hence, the power from both the klystron and the cavity is combined and fed into the accelerating structures through the RF polarizer. In this design, the authors achieved 150 MW peak power with a gain of 4 by compressing 800 ns pulses to 100 ns ones.

5.2 Cavity Design and Simulation

5.2.1 Rectangular Cavities

Existing literature for cavities used for pulse compression is limited to polarizers and spherical/cylindrical geometries. It may be prudent to investigate the use of rectangular geometries in combination with rectangular waveguide based pulse compression, as it reduces the number of mode conversions, and may, therefore, offer competitive performance. To begin with a rectangular cavity structure is designed in CST Studio. The cavity is sized to wavelength comparable dimensions. The slot plate (larger plate) has a size of 132.5 mm $\times$ 100 mm and a height of 20 mm. The ridge plate (smaller plate) has a size of 72.14 mm as shown in Fig. 5.1.

This rectangular cavity is connected to a waveguide adapter with iris as illustrated Fig. 5.2. The first 20 modes of the geometry are analyzed, with frequencies

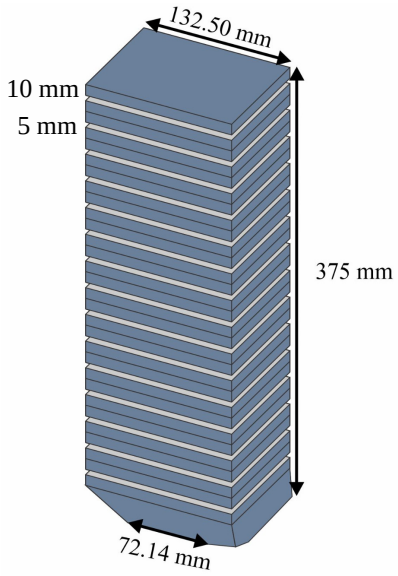

FIGURE 5.1: Schematic of rectangular resonating cavity.

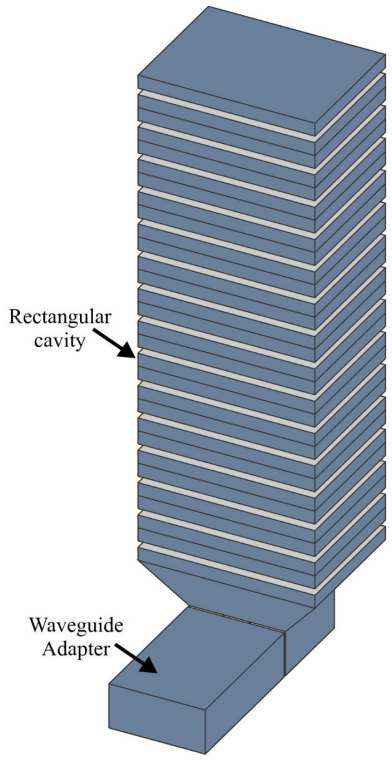

FIGURE 5.2: Rectangular resonating cavity charging setup with waveguide adapter and iris.

spanning from 2.51 GHz to 3.06 GHz. From these, mode 17 is selected as it exists at 3 GHz. The mode is identified as TM_{21} as shown in the top view of Fig. 5.3 (a) and (b), and the mode pattern for the complete eight standing wave maximas, the TM_{218} can be seen in Fig. 5.3 (b). The structure is charged for 3.5 μs by using an

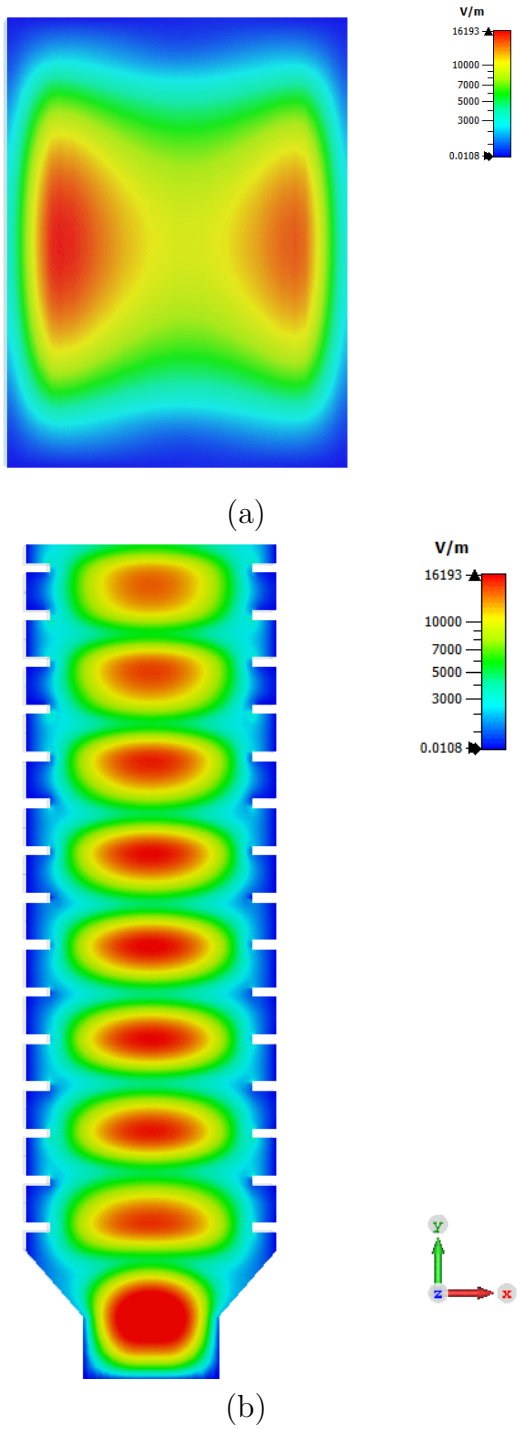

FIGURE 5.3: Standing wave pattern in rectangular cavity (a) top view (b) side view.

electric field as shown in Fig. 5.4. The absolute electric field intensity is measured using an electric field probe placed within the structure. It can be seen that the structure does not saturate with the long pulse.

The rectangular cavity simulation shows that while the cavity is capable of storing

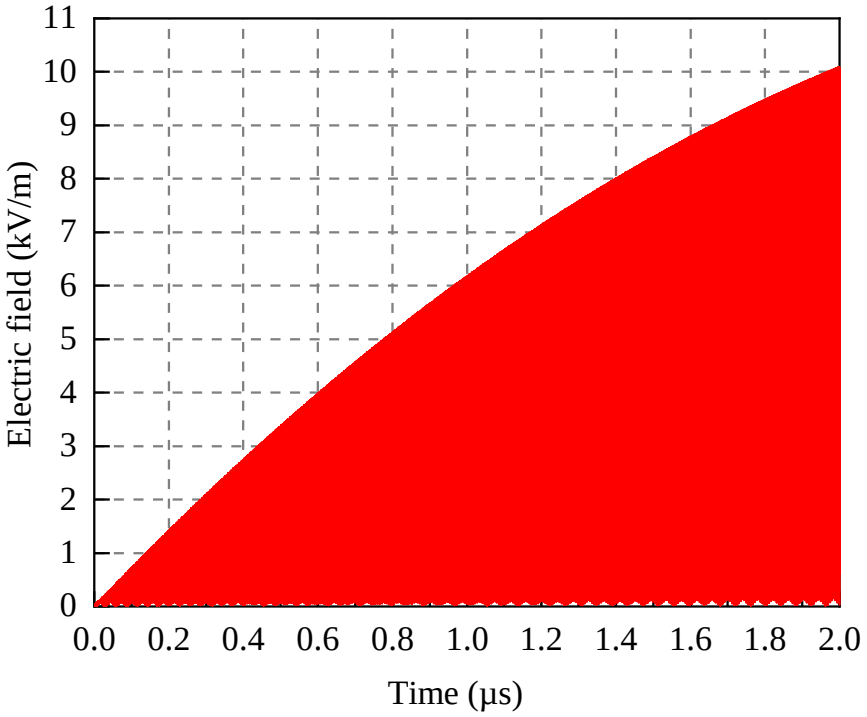

FIGURE 5.4: Charging of rectangular cavity with E-Field.

large electric fields, it is difficult to use it with the SLED RF Polarizer discussed in Chapter 3. This is due to the requirement of using mode converter at the input port. While it is possible to directly interface a rectangular cavity with a rectangular waveguide, as the tapered mode converter suffices for TE_{01} to TM_{21} conversion. However, for TE_{11} complementary modes, the converter geometry is more complicated. Moreover, the rectangular structure usually demonstrates an unloaded $Q \approx 30{,}000$. It is very likely that one can achieve a higher Q-factor from a spherical cavity.

5.2.2 Spherical Cavities

This part describes the design of spherical cavity resonating at degenerate's modes. For a proper dimensioned spherical cavity three modes are presented, i.e., TE_{01x}, TE_{11x} and TE_{11x} (90° apart) where x is radiating index along the direction of propagation. The electromagnetic fields of the structure, in the form of electric and magnetic fields within a spherical cavity, are found by solving the following

vector potential equations in spherical coordinate system:

$$\vec{\nabla}\times\vec{\nabla}\times\vec{F}-\omega^2\mu\varepsilon\vec{F}=-j\omega\mu\varepsilon\nabla\psi_m, \text{ and } \vec{\nabla}\times\vec{\nabla}\times\vec{A}-\omega^2\mu\varepsilon\vec{A}=-j\omega\mu\varepsilon\nabla\psi_e \quad (5.1)$$

where ω is the angular frequency, μ is the permeability, ε is the permittivity, $\vec{F}$, and $\vec{A}$ are the vector potentials. ψ_m and ψ_e represent the scalar potentials. For TE wave $A_r = 0$, considering $\vec{F} = \vec{a}_r F_r(r,\theta,\phi)$, where (r,θ,φ) are spherical coordinates, a general solution of Eq. 5.1 is

$$F_r = \left[A_1\hat{J}_n(kr)+B_1\hat{Y}_n(kr)\right]\left[A_2P_n^m(\cos\theta)+B_2Q_n^m(\cos\theta)\right](A_3\sin m\phi+B_3\cos m\phi)$$

where m and n are integers, A_i and B_i are constants, P and Q are Legendre's function. J and Y represent Bessel's function of first and second kinds, respectively. Since the field is finite at $r = 0$; thus, $B_1 = 0$ as $\hat{Y}_n(kr)$ is singular at $r = 0$. Also fields must be finite at $\theta = 0, \pi$, therefore, B_2 is zero as $Q_n^m(\cos\theta)$ is singular at $\theta = 0, \pi$. The field component can then be found as:

$$\vec{E} = -\frac{1}{\varepsilon}\vec{\nabla}\times\vec{F} \text{ and } \vec{H} = \frac{1}{j\omega\mu\varepsilon}\vec{\nabla}\times\vec{\nabla}\times\vec{F}$$

we have

$$E_r = 0 \quad (5.2)$$

$$E_\theta = -\frac{1}{\varepsilon r\sin\theta}\frac{\partial F_r}{\partial\phi} \quad (5.3)$$

$$E_\phi = \frac{1}{\varepsilon r}\frac{\partial F_r}{\partial\theta} \quad (5.4)$$

$$H_r = \frac{1}{j\omega\mu\varepsilon}\left(\frac{\partial^2}{\partial r^2}+k^2\right)F_r \quad (5.5)$$

$$H_\theta = \frac{1}{rj\omega\mu\varepsilon}\frac{\partial^2 F_r}{\partial r\partial\theta} \quad (5.6)$$

$$H_\phi = \frac{1}{rj\omega\mu\varepsilon\sin\theta}\frac{\partial^2 F_r}{\partial r\partial\theta} \quad (5.7)$$

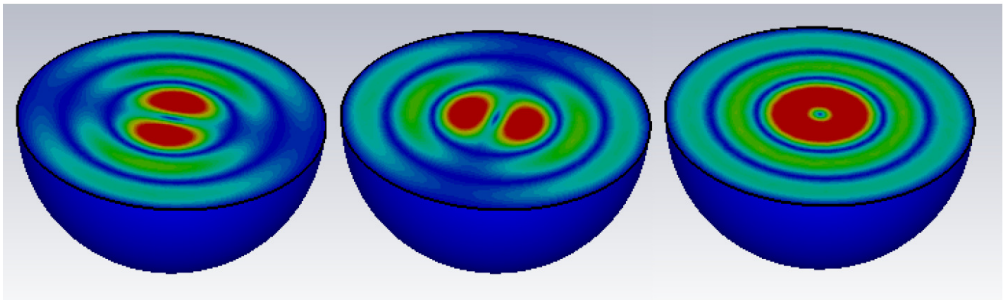

FIGURE 5.5: CST Simulation showing TE_{013} mode inside a spherical cavity.

where

$$(F_r)_{mnp} = \hat{J}_n \left(\mu_{np} \frac{r}{R}\right) P_n^m(\cos\theta) \begin{bmatrix} \cos m\phi \\ \sin m\phi \end{bmatrix} \tag{5.8}$$

The resonance frequency for TE modes is given by

$$f_{r,np} = \frac{\mu_{np}}{2\pi R\sqrt{\mu\varepsilon}} \tag{5.9}$$

where

$$m = 0, 1, 3, \cdots \leq n$$

$$n = 1, 2, 3 \ldots$$

$$p = 1, 2, 3 \ldots$$

Eq. 5.9 can be used to determine the radius of the cavity. The variable μ_{np} represents the permeability offered by the cavity to a specific mode. For 3 GHz resonating frequency and TE_{113} mode, the radius of the cavity is calculated as, $r = 173$ mm. The structure is simulated in CST MWS to verify its operation. There are three degenerate resonating modes in which two are TE_{113} with phase difference of 90°, while the other one is TE_{013}. In Fig. 5.5, the TE_{013} mode is shown.

This is a special feature of a spherical cavity in which two equivalent modes are resonating at same frequency, at complementary phase, which reduces the need of another cavity, hence, allowing for the compact RF pulse compressor design consists of a single cavity. The critical part is the coupler design i.e., the circular waveguide which will feed the cavity, and an iris between cavity and the waveguide. The dimension of circular waveguide and iris radius is needed to be set in such

TABLE 5.1: Specifications of the spherical cavity

Operating Frequency	3 GHz
Modes	TE_{113}(0, 90 deg.), TE_{014}
Perturbation Q-factor	125,600
Loaded Q-factor	20,930

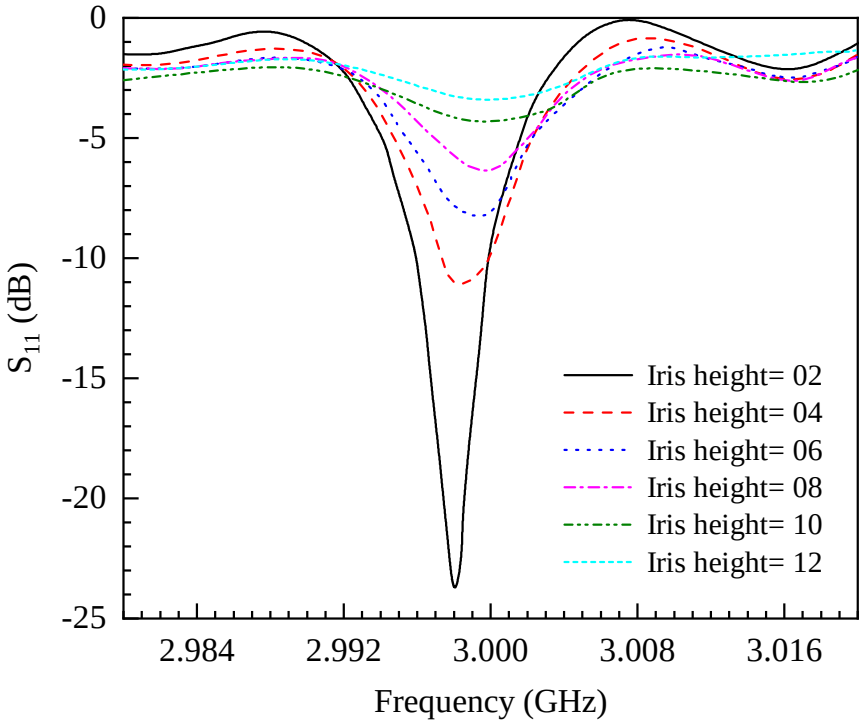

FIGURE 5.6: Cavity iris height optimization using S_{11} parameter.

a way that TE_{013} mode should die out. After long simulation and optimization using CST MWS, the desired characteristic is achieved. Also the optimization is needed in order to extract the coupling coefficient given by,

$$\beta = \frac{1 + |S_{11}|}{1 - |S_{11}|}. \tag{5.10}$$

Eq. 5.10 holds for over coupled cavities. The S_{11} of cavity at different iris dimensions are shown in Fig. 5.6. The coupling coefficient with desired resonating mode is found to be $\beta \approx 5$. If S_{11} is maximized, it leads to a lower β. In our case, an adapter height of 16 mm is selected with $S_{11} = -3.5$ dB.

Using a combination of Eigenmode solver and Time Domain solver, the cavity

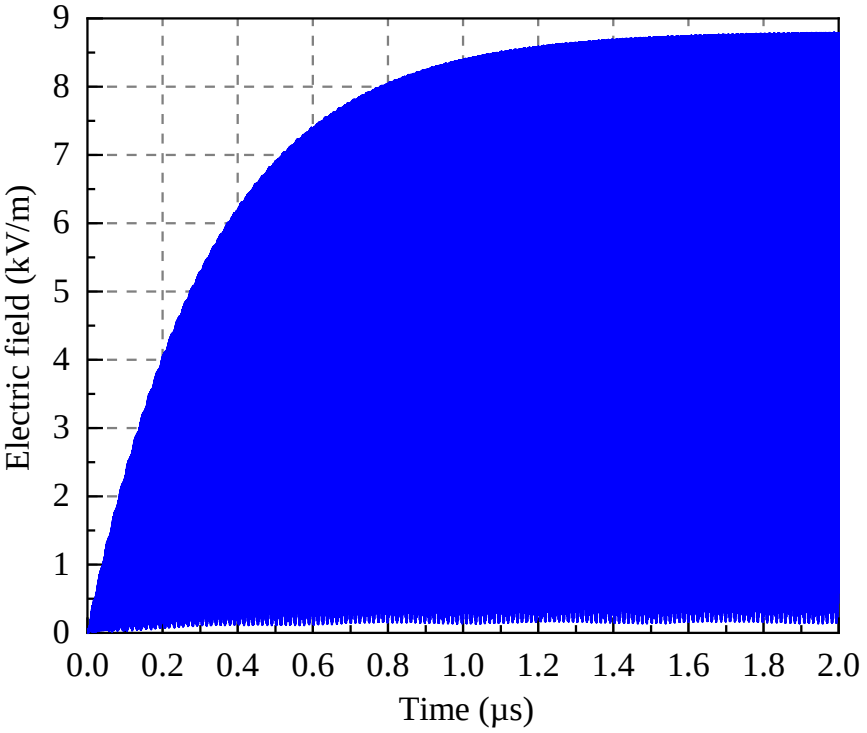

FIGURE 5.7: Charging E-field of the cavity for 2 μs.

can be fully characterized. The values of cavity characteristics obtained from the simulation are presented in Table 5.1.

In the time domain analysis, an input signal is provided for 2 μs at 1 MW power. The charging of the cavity is shown in Fig. 5.7, from the E-field probe placed within the cavity.

5.3 Fabrication of Spherical Cavities

For the study, an aluminium cavity was initially fabricated with a radius of 173 mm. Using a solid cylinder of aluminum having commercial specification as Al-6061, hemispheres were machined firstly by ID turning and then by OD turning. However, the cavity did not meet the stringent requirements for a high Q. The Q-factor is measured via S-parameter measurement using a probe connected to a Network Analyzer. Even after plating the inner surface with copper, the cavity only yielded a Q-factor (with adapter) 8,500. A second aluminium cavity was then fabricated for the same specifications. Again, utilizing a blank of

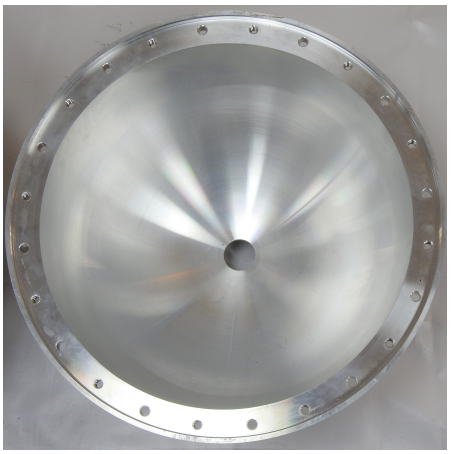

(a)

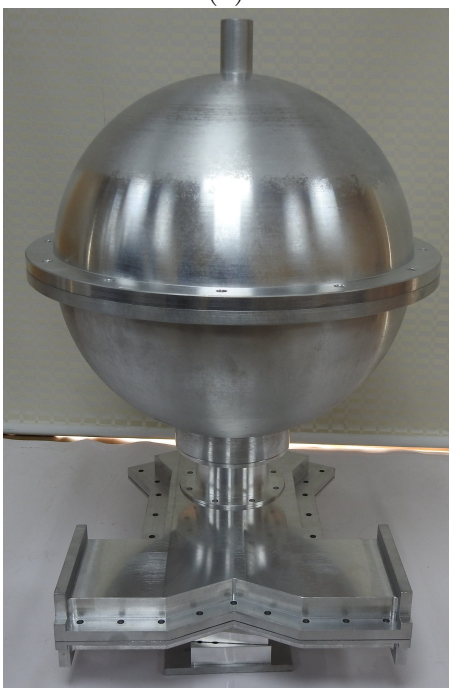

(b)

FIGURE 5.8: Aluminium cavity machined from a solid bulk (a) the inner surface of the finished cavity (b) outer view of the complete fabricated cavity

Al-6061, the hemispheres were machined on a vertical turning center, by ID and OD turning. The second cavity is shown in Fig. 5.8. In this, a special attention was paid to the surface finish of the cavity. However, due to non pure aluminium it was not possible to achieve mirror finish on the surface. The Q-factor, therefore, was only increased up to $Q \approx 11,000$ (with adapter).

Keeping in view, all these constraints, it was finally decided to fabricate copper cavity by adapting the following method:

(a) A 17 mm thick sheet of 99.95% pure copper is forged into a hemispherical shape on 500 Tons hydraulic press, with intermittent annealing and final stress relieving,

(b) The forged part is then machined into required dimensions.

(c) The roughness average (RA) value of machined part was 10 microns.

(d) After machining of the cavity, its interior surface is further improved by implying a series of emery papers of varying grain size.

(e) The surface is then electro-polished to achieve a mirror surface finish, using an electrolytic bath of 85% phosphoric acid at 4.5 V and 3.0 A.

(f) The observed RA value after electro-polishing was 0.25 microns.

(g) This is a 40 times improvement in the surface finish. The performance of electro-polished parts is improved appreciably compared to the machined parts.

A flange is brazed on to both hemispheres. A K-40 vacuum flange is brazed on one hemisphere, and the other side has a brazed SS cylindrical flange for connection with polarizer. The fabricated cavity is shown in Fig. 5.9.

5.4 Simulation with Polarizer, Experimental Testing and Results

The cavity was simulated with the polarizer for testing the compatibility of the compressor with the resonating structure. For complete design, the spherical cavity is placed on polarizer's circular port as shown in Fig. 5.10. The cavity is fed through port-1, and after a particular time of input signal, the phase reversal is applied at the input port which reverts the resonating mode field stored in the cavity. As a result, the cavity starts to discharge through port-2. The field monitor is also set at resonating frequency in order to verify the resonating mode of

(a)

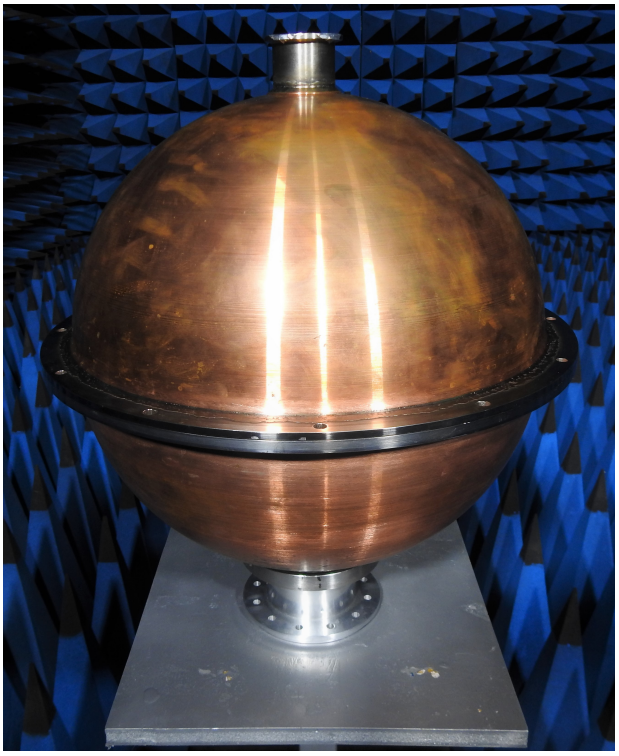

(b)

FIGURE 5.9: High purity copper cavity (a) represents interior shining surface (b) exterior of the cavity

the compressor. The resonance is unaffected when the desired mode is achieved, as shown in Fig. 5.10.

For discharge analysis, the phase is reversed once the charging is completed, and the cavity discharges for 2 μs. The power response of input and output calculated from the port signals, is shown in Fig. 5.11. It can be seen that the output power peaks at 9 MW, which shows a gain of 9 for the system. To convert the signal from time domain to frequency domain, the Fourier transform of the signal is performed and the result is shown in Fig. 5.12, which shows a central frequency of 3 GHz as

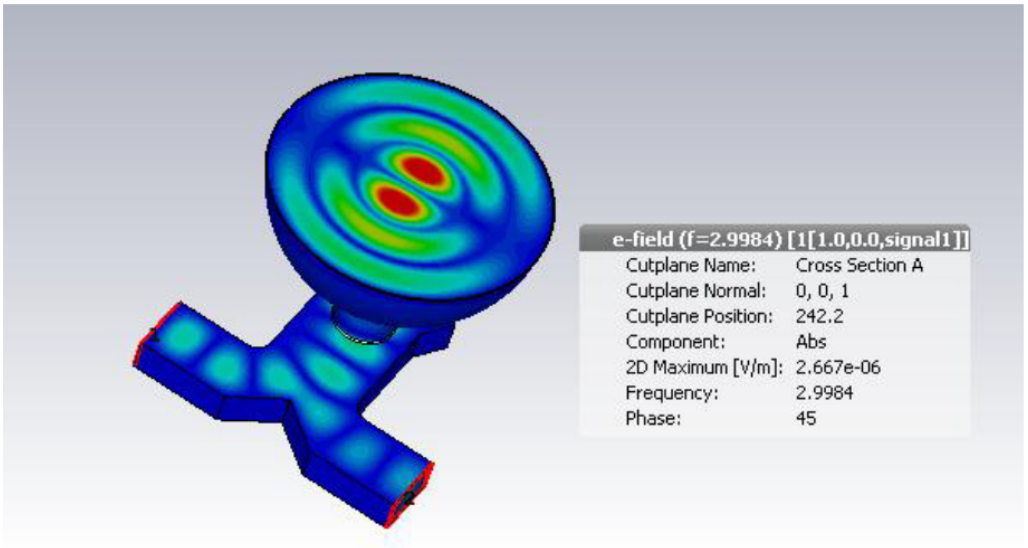

FIGURE 5.10: Mode pattern inside the cavity as it is charged/discharge via polarizer at f=2.9984 GHz.

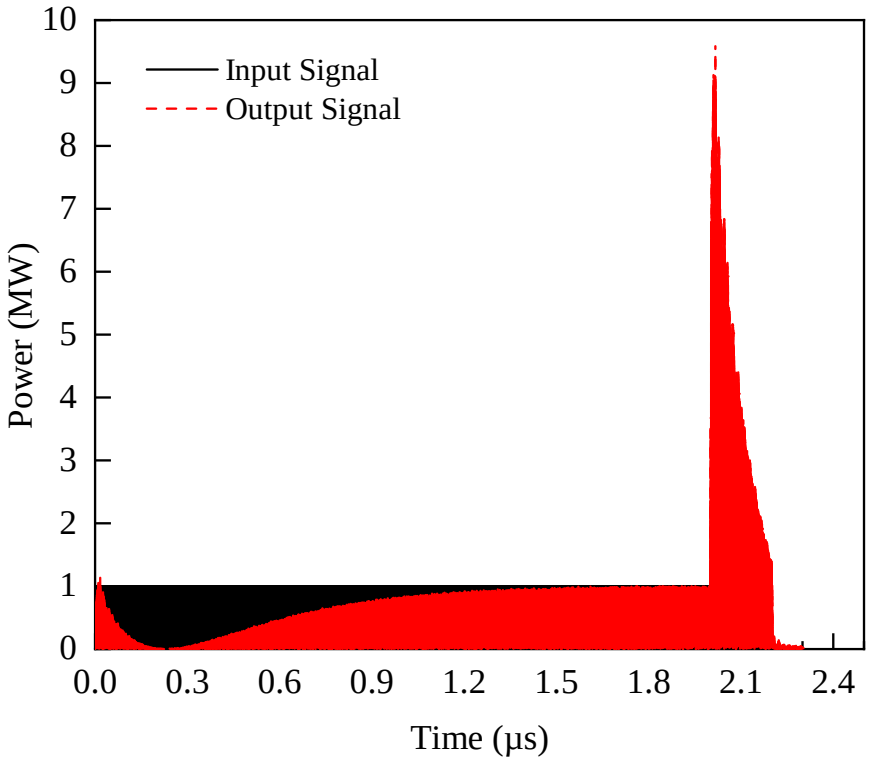

FIGURE 5.11: Input and output power for 1 MW charging and discharging from a pulse compression system based on polarizer and cavity.

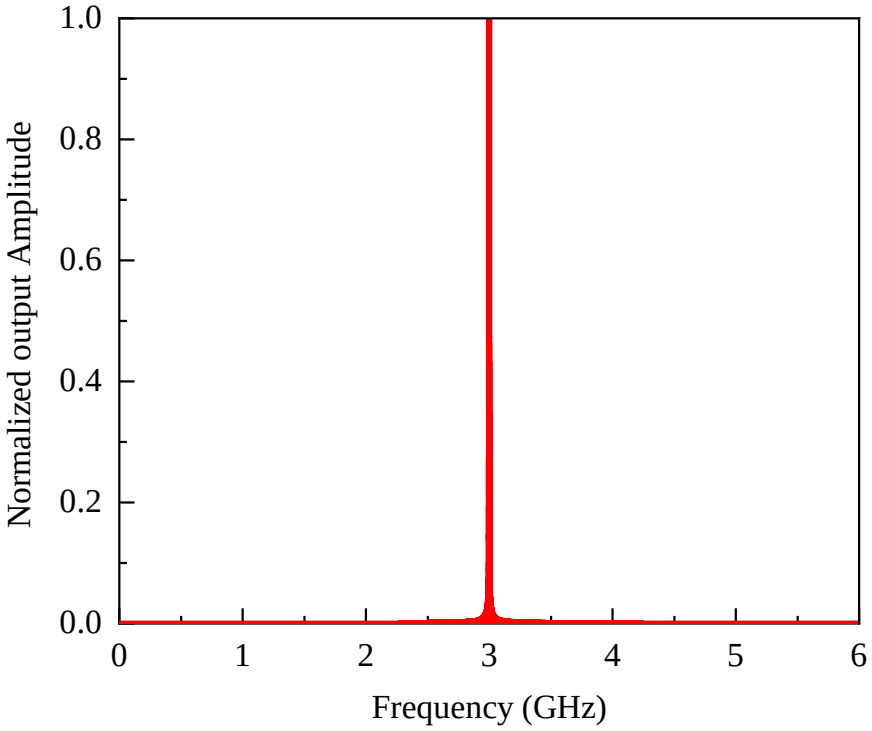

FIGURE 5.12: Fourier transform of the output signal from the cavity and the polarizer.

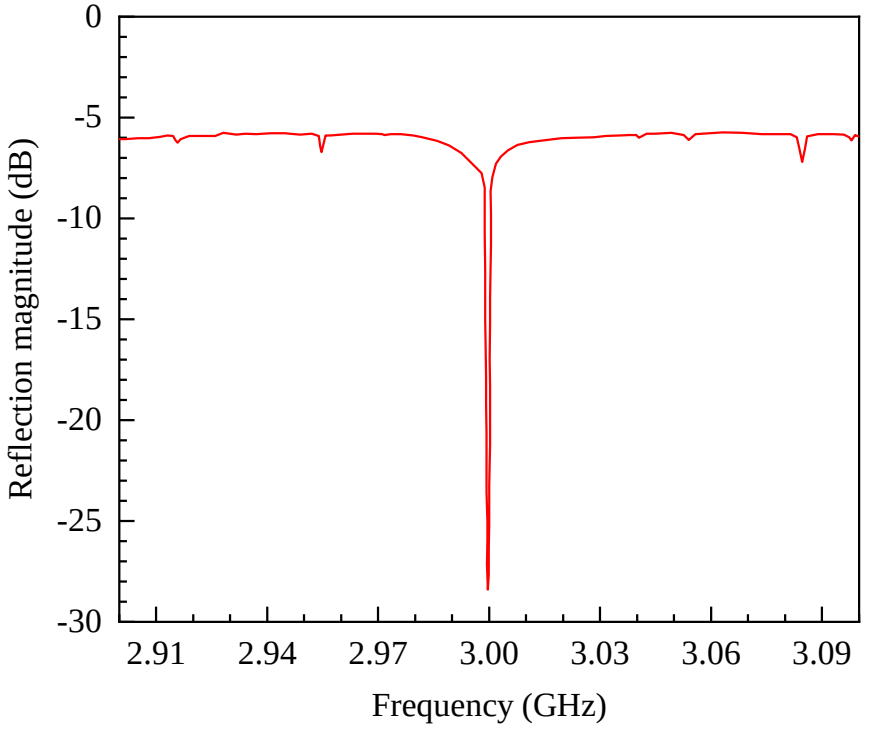

FIGURE 5.13: S_{11} plot for experimentally measuring S-parameter.

FIGURE 5.14: Pulse compressor assembly made from the copper cavity.

per specifications. Cold test is performed using VNA for a frequency range 100 kHz−20 GHz. The S_{11} plot obtained from VNA is shown in Fig. 5.13. Using this data, one can evaluate that the fabricated system leads to a high $Q_0 \approx 85,000$ for the copper cavity having brazed vacuum port and polarizer adapter.

It is pertinent to mention here that the $Q-$factor obtained experimentally, lies between loaded and unloaded $Q-$factor achieved from the simulation data. A possible explanation of this deviation could be that experimental data might not be considered as completely unloaded data, as the cavity is connected with a vacuum flange and adapter at the base. From this test it is evident that meeting the $Q-$factor standard requires compliance with stringent fabrication conditions. The pulse compressor plasma switch is assembled, as shown in Fig. 5.14. The loaded $Q-$factor of the cavity is calculated as $Q_L \approx 1{,}500$, measured from the S_{11} plot shown in Fig. 5.15.

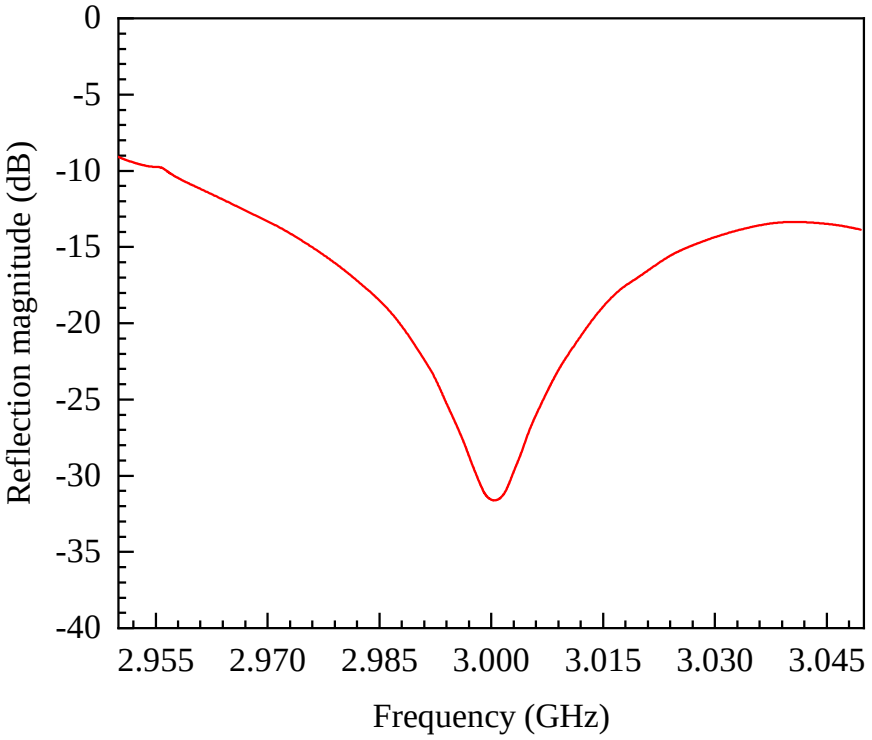

FIGURE 5.15: S_{11} plot for experimentally measuring loaded Q-factor.

5.5 Summary

This chapter presented fabrication and characterization of cavities (Al, Cu) for energy storage purposes. It is established that pulse compression is one of the techniques which could be employed to realize high energy. Simulation results showed that with the addition of a cavity structure to a waveguide, it is possible to charge the cavity in μs with proper mode conversion. It is observed that a rectangular cavity provided acceptable charging characteristics; however, it did not provide a decent $Q-$factor. A spherical cavity, while difficult to manufacture, provides the highest quality factor, if appropriate manufacturing conditions are met. Three different spherical cavities were manufactured and cold tested with an RF polarizer. $S-$parameters testing is used to observe the cavity quality factor. With a coupling coefficient, $\beta = 5$ for the desired modes, it is observed that the Al cavity did not meet the $Q-$factor specifications. The process for polished copper cavity fabrication presented in the chapter, gave a high unloaded $Q_0 = 85,000$ while being cost-efficient. This cavity could be utilized in systems requiring high power to be attained through pulse compression.

Chapter 6

Design and Analysis of Single Element Grooved Based Slotted Waveguide Antenna

6.1 Introduction

HPM technology is being actively explored [93–96] and has achieved significant importance in both military and commercial applications [97]. The selection of antenna elements is very important in the HPM system to achieve good far-field radiation characteristics along with high power handling capability [98]. The HPM antennas are usually deployed at the end terminal device of the HPM system. SWAs are mostly used in HPM applications, which include radar navigation and communication [99]. These SWA systems are attractive due to their high-gain/directivity, simplicity of design, robustness, light-weight, good reflection coefficient, and high-power handling capability [100]. SWAs are commonly made of rectangular waveguides. In SWA, slots are cut on the broad wall or narrow wall of the waveguide to radiate the electromagnetic energy in the targeted direction [101]. The most common slot types include longitudinal broad wall slots, inclined edge or sidewall slots, and cross-slot configuration [98, 102].

The SWAs are generally divided into two categories: resonant (standing-wave) and non-resonant (travelling-wave) antennas. The resonant SWAs are preferred to their complements due to short-circuit termination, which increases their efficiency without power loss. The resonant SWA configuration provides a normal beam in the targeted direction, which is independent of resonant frequency. However, the main limitation of resonant SWA is its narrow bandwidth. Travelling-wave SWAs have a wide impedance bandwidth but low efficiency due to the presence of a matched load to prevent wave reflection. In addition, a significant phase difference is realized between the radiating slots. The main beam direction is also frequency-dependent [97, 103]. The most effective technologies to improve the radiation performance of slotted antennas include: electromagnetic band gap (EBG) structures [104], electromagnetic metasurface [105], frequency selective surface (FSS) [106], partially reflecting surface (PRS) [107], dielectric radome, and corrugated groove structures [108]. The performance of the SWA configuration in this chapter is enhanced by using modified Gaussian slot distribution, inside-groove, and dielectric radomes. The inside-groove structures are usually placed around the slotted region to enhance the beaming effect in the SWAs. In addition, corrugated structures also suppress surface wave propagation [109]. The corrugation in the slotted aperture results in the re-distribution of electromagnetic waves, reflecting high field strength in the grooved surface and re-radiating the waves in the free space region as a secondary source [110]. A rectangular SWA configuration combined with a one-dimensional (1D) corrugated periodic groove is reported in [111]. The radiation performance of conventional antenna systems is enhanced by incorporating four periodic corrugated groove structures. The corrugated groove period, width, and depth play an important role in controlling the SWA performance and suppression of back-lobe.

In [112], a high-gain in SWA is attained by integrating the inside-groove structure along with a single FSS. The addition of identical grooves on both sides of the SWA aperture provides a measured peak gain of 15.1 dBi. Moreover, the addition of a symmetric groove reduces the half-power beam-width (HPBW) in a single plane to contribute to high gain achievement. Another antenna configuration with a

periodic groove arrangement is used to obtain a significant improvement in gain [113]. The authors utilized six multiple grooves in the waveguide aperture to enrich the radiation performance. The six pairs of grooves on the narrow slit provide a gain of 11 dBi and offer a narrow beam-width in the E-plane. In another study [108], a symmetric groove arrangement was applied on both sides of the slots to achieve a gain enhancement of 9 dBi. Additionally, the non-grooved region in SWA is covered with a high dielectric medium to achieve a high gain. However, SLLs are degraded due to the presence of high dielectric medium, which disturbs the surface current propagation. The inside-groove structures in the SWA system are used to enhance the isolation of array elements [114].

The distribution of slots in the SWA configuration is very important to controlling the far-field radiation characteristics. The window distribution can be categorized into uniform and non-uniform distributions. The uniform distribution in the array configuration provides high SLLs, which are undesirable in military and defence applications. Therefore, non-uniform distribution is required to improve the radiation characteristics in the single element and array configuration. Different types of non-uniform distributions include but are not limited to: Chebyshev, Taylor, and Binomial, etc. These window distributions are applied in slotted waveguides to achieve the desired SLL in H-plane [102]. In this chapter, a modified Gaussian window distribution has been designed and investigated to achieve the lowest possible SLLs. For the proposed SWA, the window function is designed in such a way that it provides an SLL of less than 20 dB in the H-plane. The performance parameters of SWA are typically influenced by the radome shape, position, and dielectric material [115, 116]. Therefore, electromagnetic analysis of the radome structure combined with the SWA system is required to overcome the degradation effect in far-field characteristics. In addition, the HPM antennas are usually sealed properly to protect them from environmental effects and to pressurize them for high power handling capability [97, 117, 118]. Therefore, to achieve the desired milestones (high gain and high-power handling capability), the Gaussian dielectric radome must be designed, sealed properly, and pressurized. The radome structure

used in the proposed design contributes to dual purpose, i.e., high power handling capability and radiation pattern improvement without affecting the other performance parameters.

In this chapter, an improved high-gain SWA system with inside-groove and Gaussian dielectric radome is designed for HPM applications. The use of the inside-groove structure offers a gain enhancement of 3.63 dBi, while the use of modified Gaussian slot distribution offers SLLs of less than 20 dB in both principal radiation planes. Moreover, a dielectric radome is placed over the SWA aperture for sealing and pressurizing to be compatible with the HPM applications without affecting the other antenna performance parameters. The proposed SWA system has been designed and analyzed by using the commercially available CST Microwave Studio 2019. The rest of the chapter is organized as follows: section 6.2 briefly outlines the design configuration and analysis of slot-position, shape, and displacement. The analysis of modified Gaussian slot distribution along with Gaussian dielectric radome is also discussed in this section. The simulated results are elaborated in Section 6.3. section 6.4 presents the parametric analysis of the proposed SWA system. The fabrication process and measured results are discussed in section 6.5.

6.2 Design and Analysis of SWA System

In this section, SWA layout and design configuration are discussed. Fig. 6.1 shows the design configuration of the SWA with a Gaussian radome and an inside-groove structure. First, a conventional SWA system is designed by using a modified Gaussian slot distribution. In the second step, inside-grooves are introduced in the design to achieve high gain and low SLLs. In the last, a high-density polyethylene (HDPE) Gaussian radome is placed on the designed SWA system to be compatible with HPM applications without affecting the performance parameters. The placement of a Gaussian radome further enhances the gain of the antenna system to some extent.

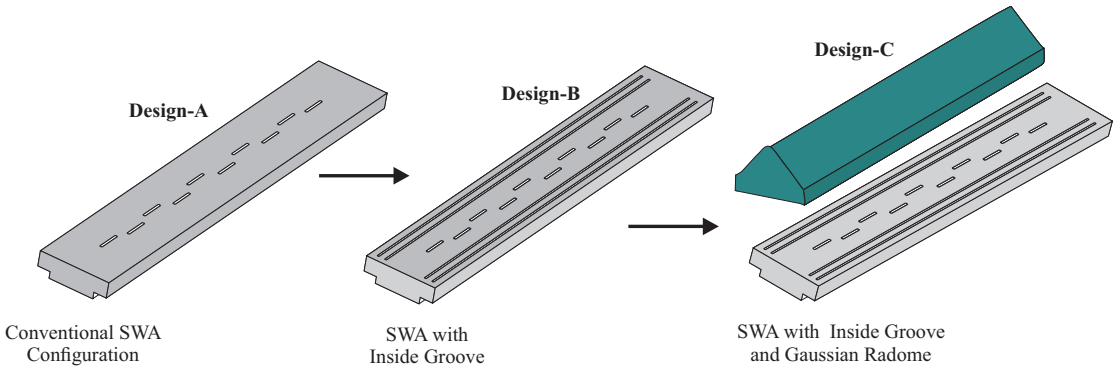

FIGURE 6.1: Design methodology of proposed SWA system with HDPE radome.

A systematic design procedure is followed in the SWA system to achieve the desired SLLs at the 3 GHz frequency band. Initially, the dimensions and positions of all radiating slot elements are determined. A modified Gaussian slot distribution is used to find the displacements of all slots from the central line of the waveguide [see Fig. 6.2 (a)] to attain the desired SLL values. The WR-284 waveguide, operating in the S-band ($2-4$ GHz) and resonating at 3 GHz, is used to achieve the intended milestones. A standard WR-284 waveguide has dimensions of $a = 2.84$ inches and $b = 1.37$ inches. The waveguide structure is fed from one side [see Fig. 6.2 (b)], while the other end is terminated properly with shorted plate [97, 119, 120].

Initially, the conventional SWA configuration with 10-slots is employed to achieve the desired gain, as shown in Fig. 6.2 (a). The radiation performance of conventional SWA can be improved with structural modification to radiate efficiently in the E-plane. For this purpose, inside-groove structures (see Fig. 6.2 (c)) are integrated on the broad wall around the main radiating region. These corrugated structures suppress the unwanted surface currents, resulting in the re-distribution of electromagnetic waves in the targeted direction. This radiating secondary source creation improves the overall radiation performance of the SWA system. After that, a dielectric Gaussian radome, as shown in Figs. 6.2 (d) and (e), is installed to be compatible with HPM applications without affecting the performance parameters and also enhance the gain of the antenna system. The rest of the overall design parameters are listed in Table 6.1, while the complete design procedure is provided in the following subsections.

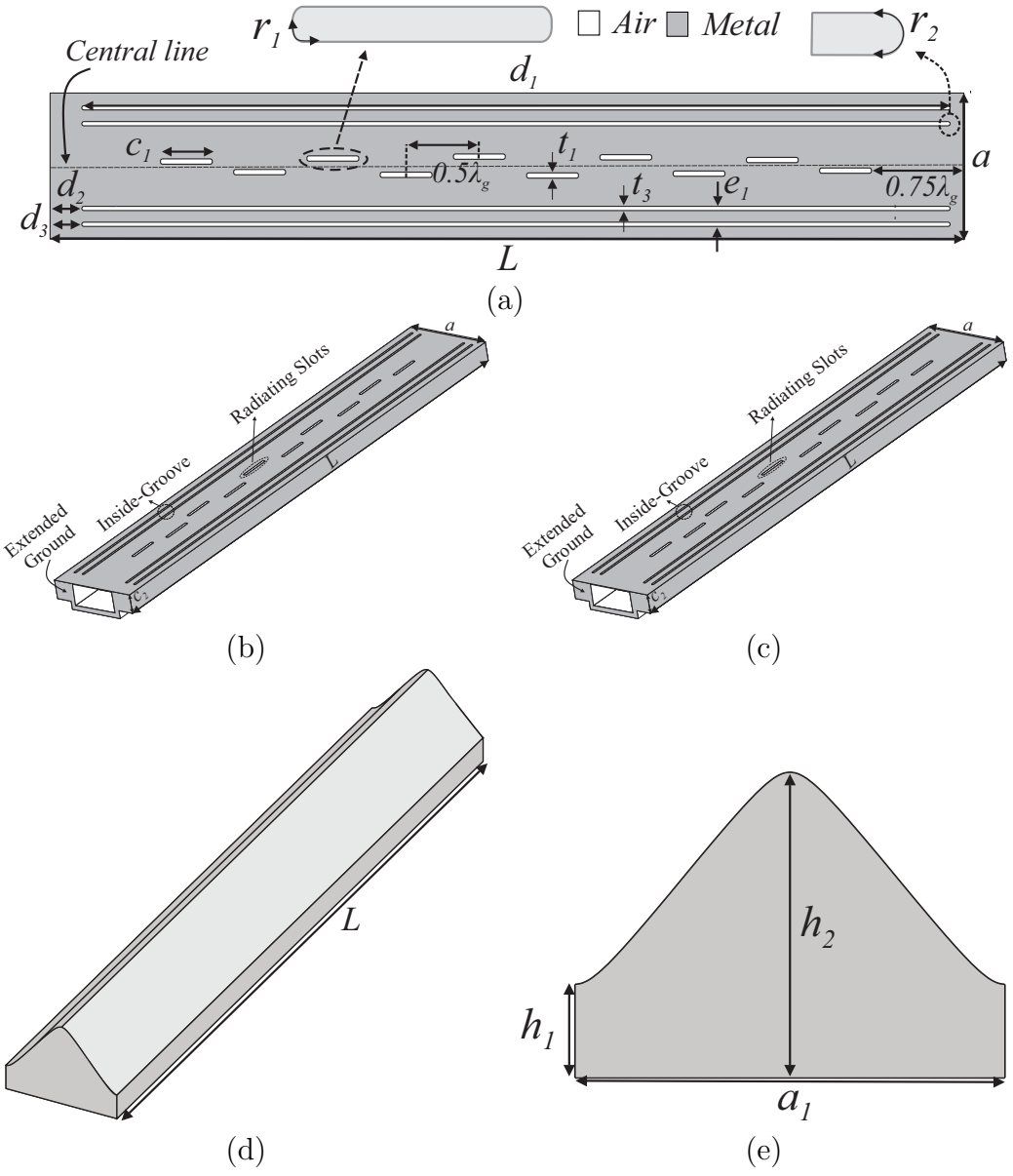

FIGURE 6.2: Design configuration of SWA with Gaussian radome and inside-groove structure (a) topview; (b) side-view (feed side); (c) 3D-view; (d) Gaussian dielectric radome 3D-view; (e) Gaussian radome front-view.

TABLE 6.1: Optimized Parameters for SWA with inside groove and Gaussian radome.

Parameter	**Value (λ_0)**
a	0.72
b	0.34
c_1	1.38
c_2	0.49
c_3	0.30
c_4	0.88
c_5	0.13
H_1	0.23
H_2	0.25
W_1	0.02
r_1	0.02
r_2	0.05
d_1	8.17
e_1	0.11
L	8.46
λ_g	1.387
t_1	0.05
t_2	0.03
t_3	0.04
H_2	0.208
W_2	0.02

6.2.1 Position of Longitudinal Slot

The following steps are taken into consideration for slots' placement on the broad-side wall of the waveguide: the first slot is placed at a distance of $3\lambda_g/4$ from the feeding point [see Fig. 6.2 (a)] and all other slots are placed at a distance of $\lambda_g/2$, as shown in Fig. 6.1. For SWA design, the guided wavelength (λ_g) is calculated as follows:

$$\lambda_g = \frac{\lambda_0}{\sqrt{1-\left(\frac{\lambda_0}{\lambda_{\text{cutoff}}}\right)^2}} = \frac{c}{f} \times \frac{1}{\sqrt{1-\left(\frac{c}{2a.f}\right)^2}} \tag{6.1}$$

where λ_0 and λ_{cutoff} are the operating and cut-off wavelengths of SWA, respectively. c is the speed of light and f is the resonant frequency. For the desired resonant frequency (3 GHz), λ_g = 138.5 mm. For the longitudinal slot configuration, the waveguide acts as a transmission line model. Therefore, by employing

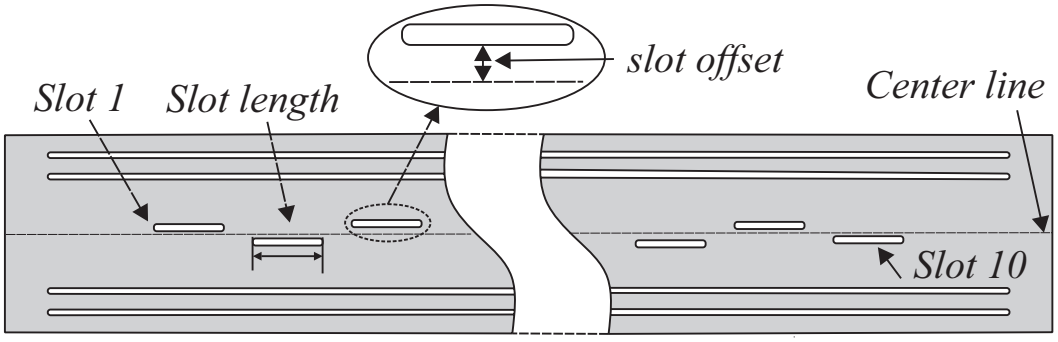

FIGURE 6.3: SWA design configuration with slot size and offset position.

the concept of a transverse electric field in each slot, TE_{10} mode scattering is considered to be symmetrical in this configuration [97, 102, 120].

6.2.2 Shape and Dimensions of Slot

The shape and geometry of the slot play an important role in the design of the HPM antenna. The conventional rectangular slot configuration integrated with the HPM source could heighten electrical breakdown problems due to electric field enhancement at sharp corners [102]. This rapid field enhancement in the slotted region can lead to self-induced microwave breakdown of the air in the slot. Therefore, sharp corners are avoided to overcome this issue in HPM applications. A round-edged slot configuration (see Fig. 6.3) was chosen to improve the power handling capability with less manufacturing difficulty compared to the rectangular slot (sharp 90° angle at corners). In the round-edged slot configuration, the length is optimized to obtain the desired reflection coefficient in the 3 GHz frequency band. The width of the slot in the round-edged configuration in our design is taken to be equal to $\lambda_0/10$ due to design limitations related to available fabrication limitations. The thickness of the upper slotted plate is 3 mm, according to which specific slot thickness is considered to obtain a good impedance match at the desired frequency band [97, 101, 119, 121, 122].

6.2.3 Slot Offset

The slot offset plays an important role in controlling the SLLs of the SWA system. The distance between the broad wall centre-line and the slot-centre is indicated as the slot offset. There are two types of slot distribution: uniform and non-uniform. In uniform distribution, all slots are placed at the same offset from the central line and have equal excitations for all elements in the antenna array. The uniform distribution is easier to implement with a similar offset distance, but the major drawback is the higher SLLs in the array configuration. Therefore, non-uniform slot displacement is preferred to control the SLLs in the array configuration [102].

All the slot elements in SWA should radiate in phase to obtain higher efficiency. Therefore, slots are deployed in an alternating order on the broad side wall of the SWA around the central-line (see Figs. 6.2(a) and 6.3) [123, 124]. The non-uniform slot distribution approach for desired SLLs and slot displacement is illustrated in Figs. 6.4. The slot displacements around the central line are calculated as follows: firstly, required SLL values are chosen, and then slot conductance is determined using a modified Gaussian slot distribution. The obtained slot conductance is used to extract the value of slot displacement from the central line. The slot displacements basically control the excitation of every slot and are also used to control the SLL value of the entire SWA system. In [123, 125], different window functions, including Chebyshev, Taylor, and Binomial, have been implemented for specific SLLs in SWA design. In our proposed design configuration, a modified Gaussian window is chosen to calculate the slot displacement. The modified Gaussian curve is defined by the following equation:

$$W(z) = \mathrm{Exp}\left[-\frac{1}{2}\left(\frac{\alpha z}{{}^{(N-1)}/_{2}}\right)\right] \tag{6.2}$$

where, ${}^{-(N-1)}/_{2} \leq z \leq {}^{(N-1)}/_{2}$, N denotes number of points for Gaussian distribution, and α represents SLL controlling parameter.

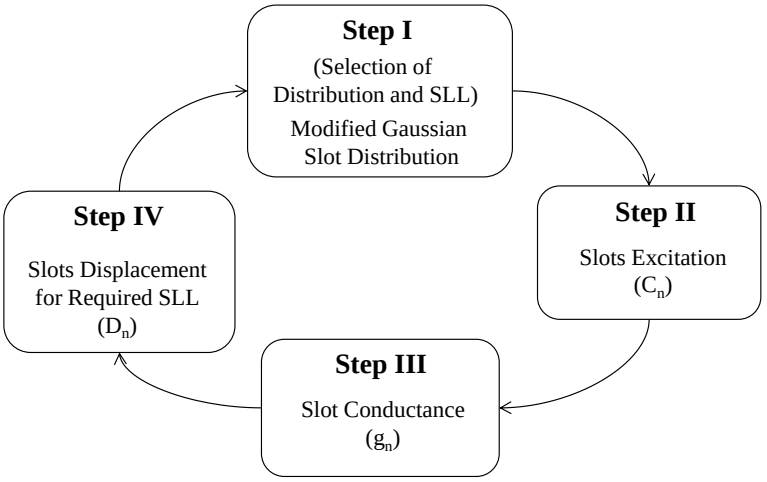

FIGURE 6.4: Methodology to obtain the required SLLs with modified Gaussian slot distribution.

TABLE 6.2: Gaussian distribution coefficients and slot displacement.

Slot	**Gaussian Effect**	**Slots Displacement**
1	1.000	0.9052
2	7.5588	2.4929
3	34.4584	5.3608
4	94.7376	9.0399
5	157.0855	11.8628
6	157.0855	11.8628
7	94.7376	9.0399
8	34.4584	5.3608
9	7.5588	2.4929
10	1.000	0.9052

Initially, a modified Gaussian window has been analyzed to generate different SLL values with the controlling parameter (α), as shown in Fig. 6.5. The Gaussian window distribution is optimized for 10-slots in SWA to achieve the desired SLL in the H-plane. By using the obtained Gaussian coefficients (listed in Table 6.2), an SLL value of 46.5 dB, which is 8 dB lower as compared to the Binomial distribution (38.8 dB SLL), with the same gain value of 15 dB being achieved [102, 126]. The slot displacements against these coefficients are obtained by using Eqs. 6.3 and 6.3 [97, 115, 123, 124], and are listed in Table 6.2.

The proposed modified SWA simulations have been performed in CST Microwave

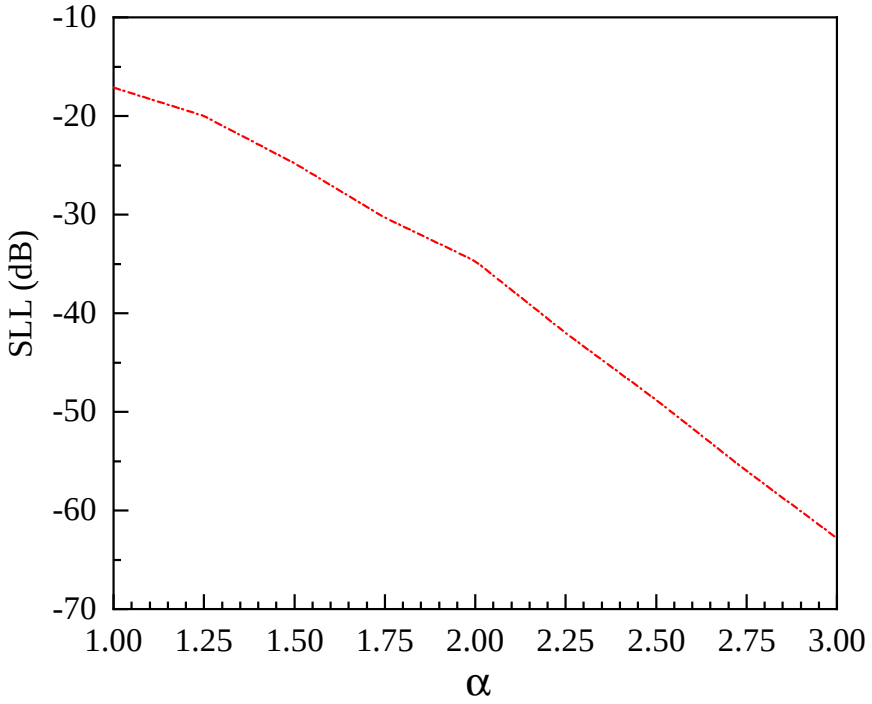

FIGURE 6.5: Modified Gaussian slot distribution with different SLL with controlling parameter (α)

Studio, which provides -19.5 dB SLLs and a gain of 16.5 dBi with a reflection coefficient of -32 dB. The proposed SWA gain performance with other reported distributions (uniform, Chebyshev, Taylor, and Binomial) in [102] is compared in Tables 6.3 and 6.4:

$$d_u = \frac{a}{\pi}\sqrt{\arcsin\left[\frac{1}{N \times G}\right]}, \tag{6.3}$$

where,

$$G = 2.09 \times \frac{a}{b} \times \frac{\lambda_g}{\lambda_0} \times \left[\cos\left(0.464\pi \times \frac{\lambda_0}{\lambda_g}\right) - \cos(0.464\pi)\right]^2 \tag{6.4}$$

6.2.4 Design of Inside-Groove Structure

The inside-groove structures are usually deployed around the slotted region to enhance the radiation performance of the conventional SWA system. The grooves are mostly used to re-radiate the surface wave radiation and suppress surplus surface currents at the extended ground edge of the SWA aperture. The edge diffraction

TABLE 6.3: 10-slots 2-groove configuration performance analysis with constraints of SLL (−20 dB).

Distribution Window	**Gain (dBi)**	**Return Loss (dB)**	**SLL (dB, H-plane)**
Gaussian	16.4	-32	-20
Chebyshev	16.1	-20	-20
Taylor	16.0	-20	-20

TABLE 6.4: Modified Gaussian Slot Distribution Performance analysis in terms of lowest SLL with constraint of same Gain (15 dB) (conventional Design).

Dist. Window	**Gain (dBi)**	**Bandwidth**	**Return Loss (dB)**	**Beam-width (E-plane)**	**SLL (dB, H-plane)**
Gaussian	15	≈120	−25	11.5°	−46.5
Binomial [121]	15	≈120	−23	11.1°	−38.6

currents are suppressed in the grounded region due to the presence of corrugated inner grooves around the slots. The dimensions of the grooving structure are very important to controlling the radiation performance. The radiation performance depends on the following parameters, which include: periodicity, depth, width, and length of grooving structure. The first groove is placed at the wall of the waveguide U-channel at $0.56\lambda_0$ distance from the centre of the waveguide (see Fig. 6.6) having a length of $8.71\lambda_0$, depth of $h_1 = 0.23\lambda_0$, and a width of $x_2 = 0.04\lambda_0$. The second groove is located $0.65\lambda_0$ from the center, $0.0761\lambda_0$ from the first groove, and has a length of $8.71\lambda_0$, a depth of $h_2 = 0.208\lambda_0$, and a width of $x_2 = 0.04\lambda_0$, as shown in Fig. 6.6.

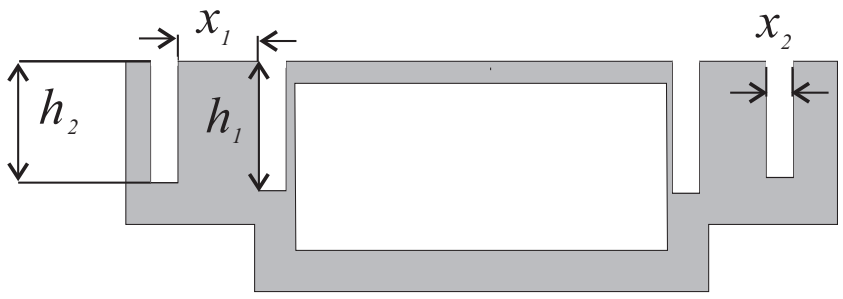

FIGURE 6.6: Side-view of WR-284 waveguide with inside-grooves.

6.2.5 Design of Dielectric Gaussian Radome

A transparent RF radiation dielectric radome is mostly placed on the SWA aperture in the HPM antenna design to contain vacuum or pressurized gas (N_2 or SF_6) for HPM capability. This dielectric enclosure protects the antenna aperture from external environmental effects, including dust, moisture, and rain. Moreover, the dielectric enclosure also provides aerodynamic support. To fulfil these required milestones, a Gaussian-profiled dielectric radome has been designed, which has the clear advantages of gain enhancement and beam-width suppression in the E-plane without affecting the reflection coefficient and radiation characteristics. The dielectric enclosure is used for the sealing of the 10-slot SWA aperture to hold the vacuum or pressurized to enhance E-field breakdown strength [127–129]. The dielectric radome is based on the Gaussian function and can be defined as:

$$W(z) = he^{-\frac{1}{2}\left(\frac{z}{\zeta}\right)^2} \tag{6.5}$$

where $-l/2 \leq z \leq l/2$, h is the height of the dielectric enclosure, l denotes the width of the profile, and ζ represents the beam shaping parameter. The analysis of ζ for normalized height and width is shown in Fig. 6.7. The radiated electromagnetic waves may be converged or diverged with the effect of diffraction based on the curvature profiling and thickness of the dielectric material. In the proposed design, a dielectric Gaussian radome is designed to converge the electromagnetic waves in the targeted direction at a height of 100 mm. The dielectric Gaussian-profiled curvature and thickness are optimized with the objective of improving the radiation patterns (i.e., gain enhancement and beamwidth reduction) along with vacuum/pressurized gas sealing for HPM capability without affecting the reflection coefficient. The HDPE dielectric material has been used for radome design with a dielectric constant of 2.1.

The following parameters are chosen for the radome: $h = 100$ mm, $l = 138.14$ mm, and $\zeta = 0.95$ with a thickness of 30 mm.

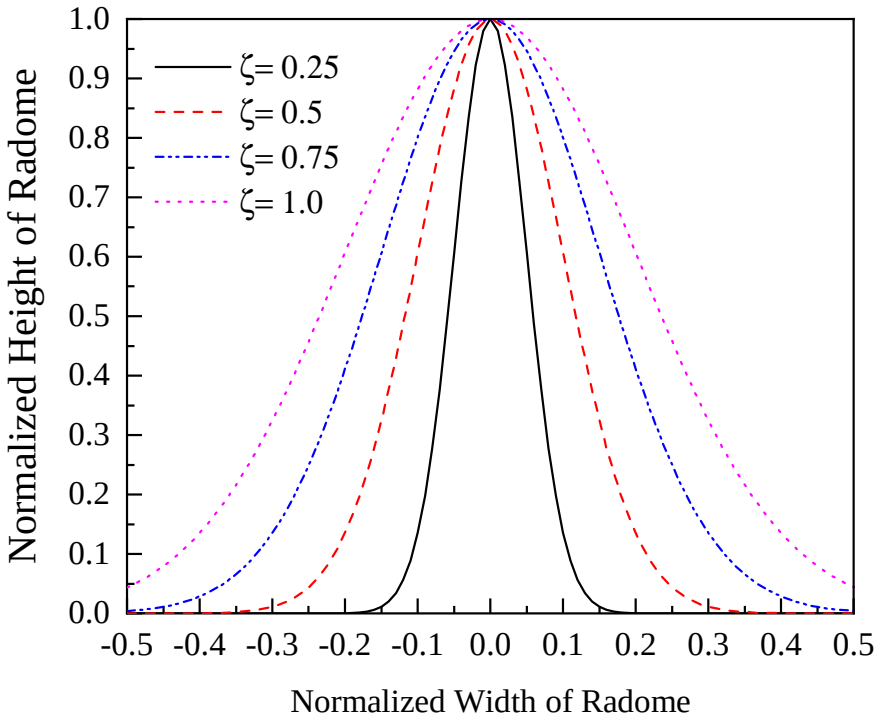

FIGURE 6.7: Effect of ζ on modified Gaussian radome shape.

6.3 Simulation Results and Discussion

The performance of a modified SWA configuration with inside-groove and dielectric radome is studied in terms of reflection coefficient, surface current distribution, and far-field radiation characteristics. The conventional SWA configuration provides a dip at 3 GHz with a reflection coefficient of 17 dB. The grooving region in the SWA is used for a dual purpose: to achieve better impedance matching along with gain enhancement. The proposed SWA system design methodology is shown in Fig. 6.1, and the corresponding reflection coefficient for each design step is demonstrated in Fig. 6.8. The addition of the first and second groove on the SWA broadside aperture improves the reflection coefficient from 17 dB to 35 dB. The dielectric radome is very important in HPM systems to pressurize the waveguide for HPM capability. The HDPE-based Gaussian-shaped dielectric radome is used for pressurization. The reflection coefficient of SWA is not shifted by applying the dielectric radome. However, the reflection coefficient magnitude is decreased by up to -25 dB by installing the dielectric radome.

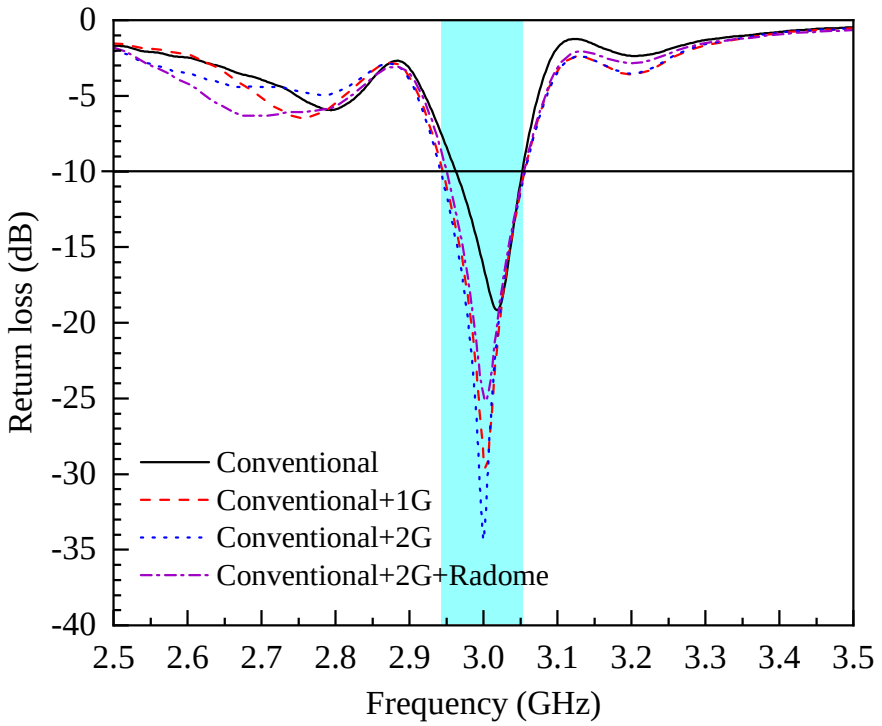

FIGURE 6.8: Reflection coefficient of the proposed SWA system with inside-groove and radome (1G: first groove, 2G: second groove).

The surface current distribution of a 10-slot configuration with one and two grooves is illustrated in Fig. 6.9. In the conventional SWA configuration, currents are converged and dominate around the slotted region. It can be seen that the current in the groove structure is strongly concentrated in the centre compared to the conventional SWA system. High surface currents are now localized around the edges of the slots in the modified geometry with 2-grooves. Moreover, a high current region is also observed inside the grooves. These high densities with localized current regions increase the gain of the proposed geometry from 16.4 dBi to 18.9 dBi. Due to the high-density localized currents around the slots and grooved region, the gain of the grooved integrated SWA increased, whereas the SLL was significantly reduced. The comparison of conventional SWA in terms of design methodology is given in Table 6.5.

The far-field E- and H-plane radiation characteristics of the proposed SWA system are shown in Fig. 6.10. The addition of the 1^{st} and 2^{nd} groove enhances the gain and reduces the E-plane beam-width. The E-plane of SWA is controlled by the structural changes (groove integration). Moreover, the addition of a dielectric

TABLE 6.5: Modified Gaussian Slot Distribution comparison and design approach.

Performance Enhancement Technique	**Gain (dBi)**	**Beam-width (E/H-plane)**	**SLL (dB) (E/H-plane)**	**Return Loss (dB)**	**Gain Enhan. (dB)**	**Remarks**
Conventional with Gaussian Window	16.4	84°/8.4°	−14.7/−19.9	−25	–	∼20 dB SLL in H-plane is achieved.
One Inside Groove	17.9	65.7°/8.1°	−26.2/−20.3	−22	1.5	Gain enhancement of 1.5 dB.
Two Inside Grooves	18.9	52.1°/8.1°	−21.7/−20.6	−35	2.5	Gain enhancement of 1.0 dB.
Two Inside Grooves + Gaussian Radome	20.1	42.4°/8.1°	−22.1/−21.0	−30	3.7	Gain enhancement of 1.0 dB.

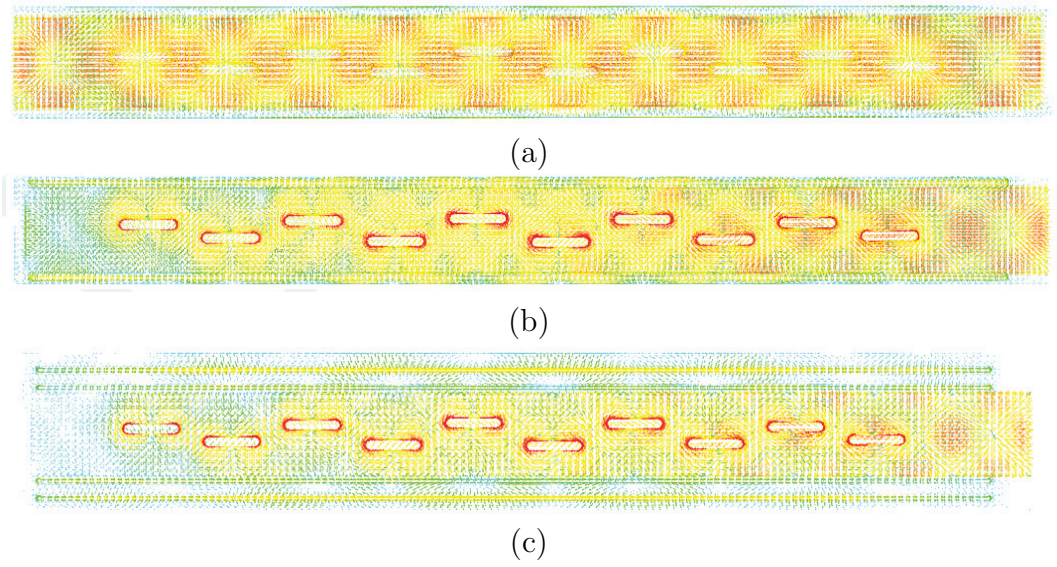

FIGURE 6.9: Vector surface current distribution on the SWA configuration (a) conventional SWA configuration; (b) 1-groove SWA configuration; (c) 2-groove SWA configuration.

radome increases the gain and directivity of the proposed SWA configuration. It is also possible to see that the radiation pattern has a confined beam in the desired direction with no significant side-lobes or back-lobes before and after the radome installation. The conventional SWA offers a gain of 16.4 dBi, which is further enhanced up to 18.9 dBi (see Fig. 6.10) with the help of inside-grooves. The dielectric Gaussian radome at the end is placed on the SWA aperture for beam shaping without affecting the other SWA performance parameters. The dielectric radome provides gain enhancement of 1.2 dB (see Fig. 6.10) along with an E-plane beam-width reduction of about 10°, as shown in Fig. 6.10 (a). Furthermore, there is no or minimal effect observed in the beam-width of the H-plane radiation pattern, as shown in Fig. 6.10 (b). The change in gain value and beam-width is also listed in Table 6.5.

The power handling capability of the SWA system integrated with inside-grooves is estimated to be able to withstand the electrical breakdown. To calculate the power handling capability, the electric field distribution on the aperture of the SWA system is simulated and illustrated in Fig. 6.11. The maximum electric field intensity on the aperture is 680 V/m when the structure is excited with 0.5 W

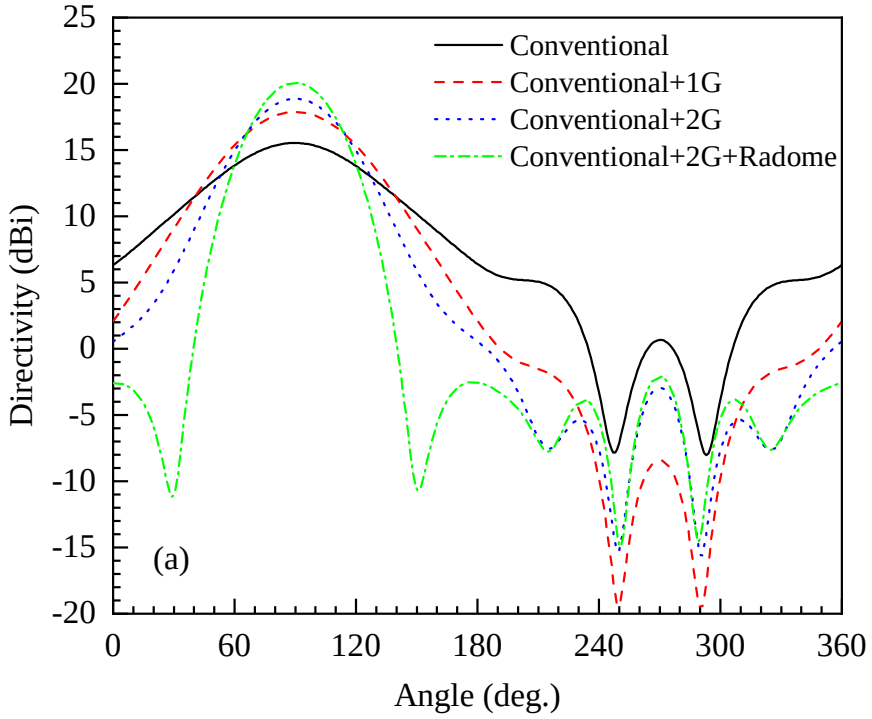

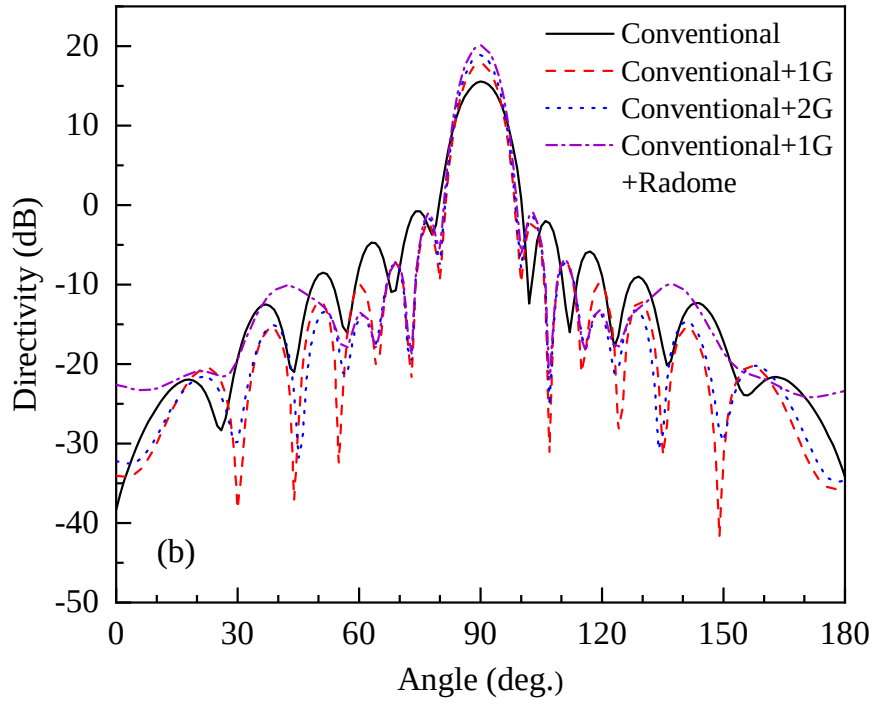

FIGURE 6.10: Radiation characteristics of SWA with Gaussian radome and inside-groove (a) E-plane; (b) H-plane.

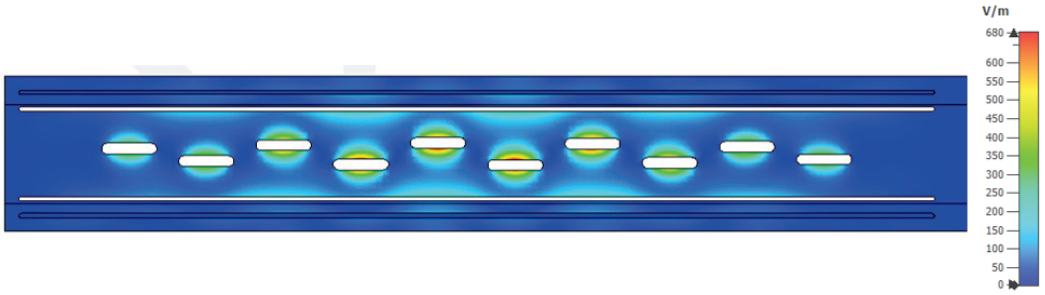

FIGURE 6.11: Maximum E-field on the aperture of SWA with integrated grooves.

of input power. According to the square relationship between power P and field intensity E, the power capability can be calculated as follows:

$$P = \left[\frac{E_{(Bd)}}{E_0}\right]^2 P_{in} \tag{6.6}$$

where, $E_{(Bd)}$ represents vacuum breakdown threshold of 10 MV/m in the S-band, E_0 is the maximum E field intensity (680 V/m), and Pin is the input power (0.5 W). Numerical analysis indicates that the power capacity of the whole SWA with groove structure is more than 100 MW.

6.4 Parametric Analysis

A parametric analysis has been performed to observe the effects of different design parameters of SWA with integrated groove. These parameters include: width, position, length, and depth of inside-groove. The variation of these design parameters during fabrication effects the reflection coefficient and far-field characteristics. The effect of groove length is discussed in Fig. 6.12. By decreasing the length of grooves from the corners, good impedance matching is achieved at $d_2 = d_3 = 0.4\lambda_0$.

The effect of groove position is discussed in Fig. 6.13 (a). By moving the groove position towards the corners of the waveguide, the resonance frequency shifts towards a higher band. An optimum position was chosen to achieve the better

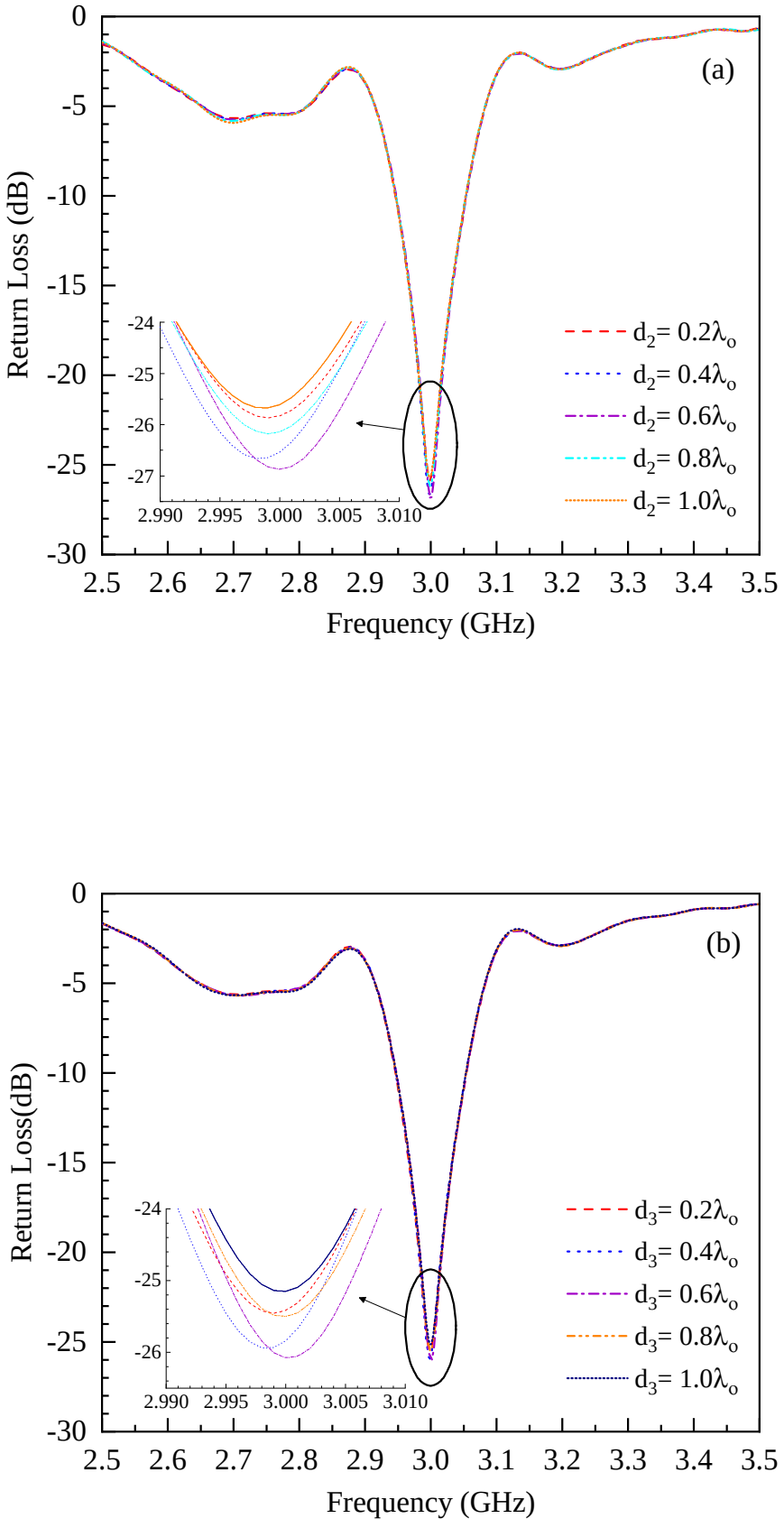

FIGURE 6.12: Effect of (a) d_2 and (b) d_3 on SWA reflection coefficient.

impedance matching at $P = 0.15\lambda_0$. The effects of first and second groove width are illustrated in Figs. 6.13 (b) and (c). The first and second groove widths do not significantly affect the reflection coefficient. A good return loss response of 28 dB is achieved at $W_1 = W_2 = 0.04\lambda_0$. The depth of both grooves (H_1 and H_2) is very critical in controlling the reflection magnitude. By increasing the depth of grooves, a higher reflection coefficient is achieved, as shown in Figs. 6.13 (d) and (e). However, in deeper hollow regions, fabrication difficulties are involved. By keeping the fabrication constrictions, an optimum depth was chosen for both grooves ($H_1 = 0.23\lambda_0$ and $H_1 = 0.208\lambda_0$). The effect of design parameters on the radiation patterns is illustrated in Fig. 6.14. The position of grooves in view of fabrication limitations is chosen, which does not affect the patterns by more than 0.7 dBi [see Fig. 6.13 (a)]. The width of both grooves is also optimized according to the fabrication limitations. The effect of W_1 and W_2 is shown in Figs. 6.14 (b) and (c). It is observed that the width has a minor effect on the gain of SWA. The most important and critical parameter is the depth of both grooves. By increasing the depth of grooves, gain is also increased, as shown in Figs. 6.14 (d) and (e).

6.5 Experimental Results

The fabrication process of the high gain SWA system consists of two parts. Firstly, the fabricated SWA prototype is made of aluminium material by using the milling process. The top round-edged radiating slots, along with waveguide walls, are made in a single piece and then coupled and sealed to the bottom SWA plate. The internal surface of the fabricated antenna is mirror finished to reduce the internal ohmic losses and improve the efficiency. Secondly, the Gaussian dielectric radome is made of HDPE material to be compatible for HPM applications and external environmental protection. The SWA and dielectric radome are separately illustrated in Fig. 6.15 (a). The full assembly of SWA with HDPE radome is shown in Fig. 6.15 (b).

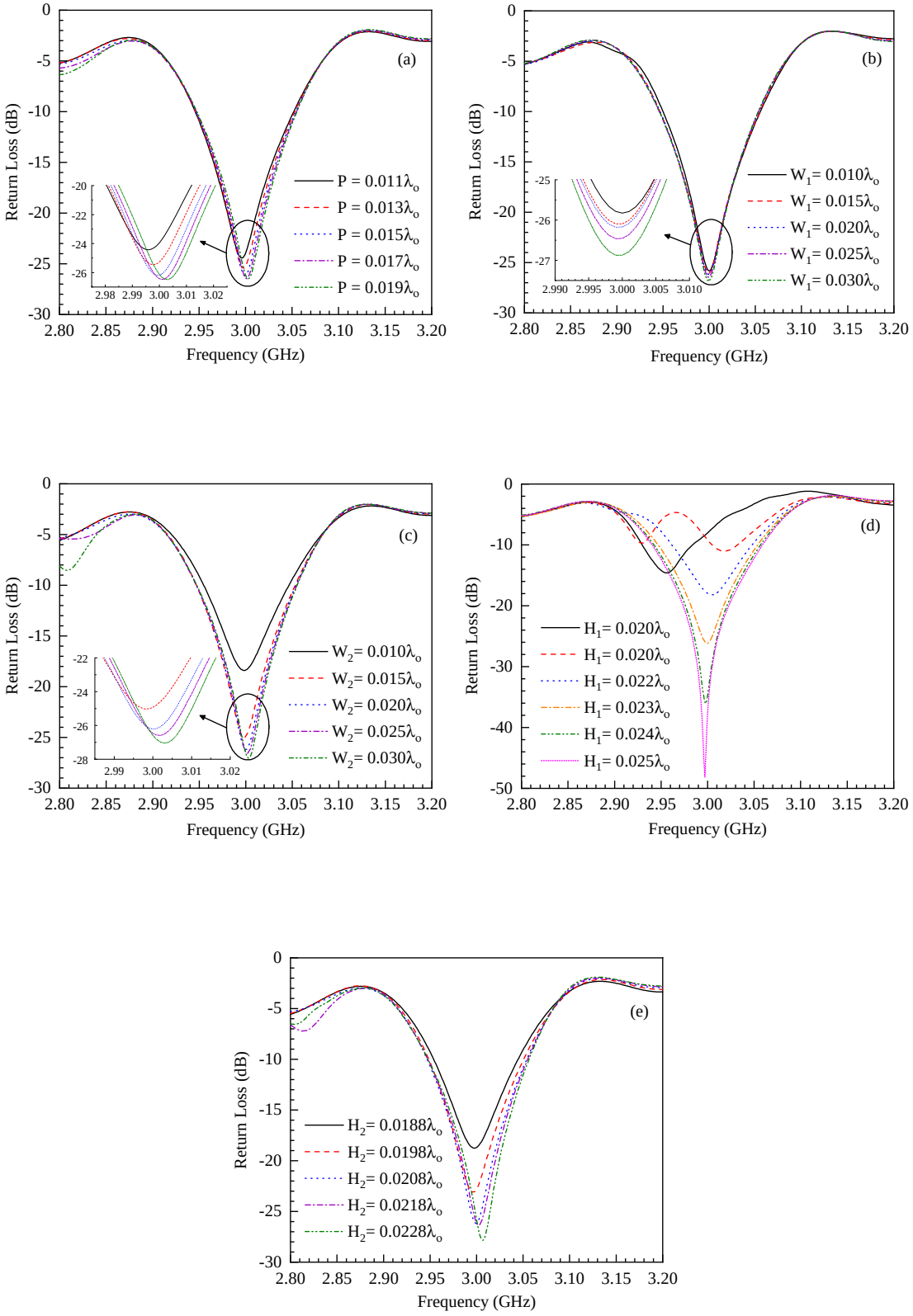

FIGURE 6.13: Effect of (a) groove position (P); (b) first groove width (W_1); (c) second groove width (W_2); (d) first groove depth (H_1); and (e) second groove depth (H_2) on SWA reflection coefficient.

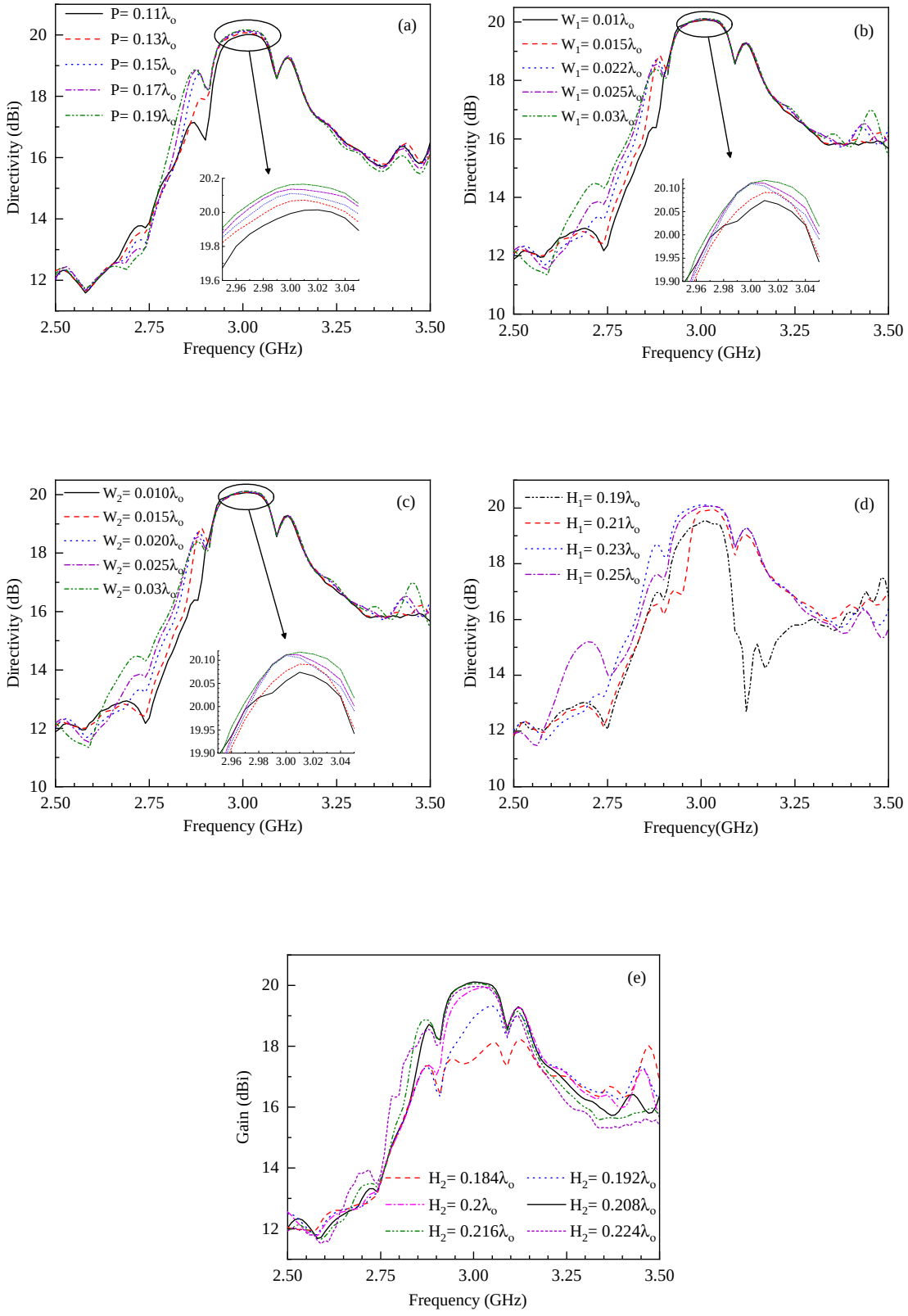

FIGURE 6.14: Effect of (a) groove position (P); (b) first groove width (W_1); (c) second groove width (W_2); (d) first groove depth (H_1); (e) second groove depth (H_2) on SWA gain.

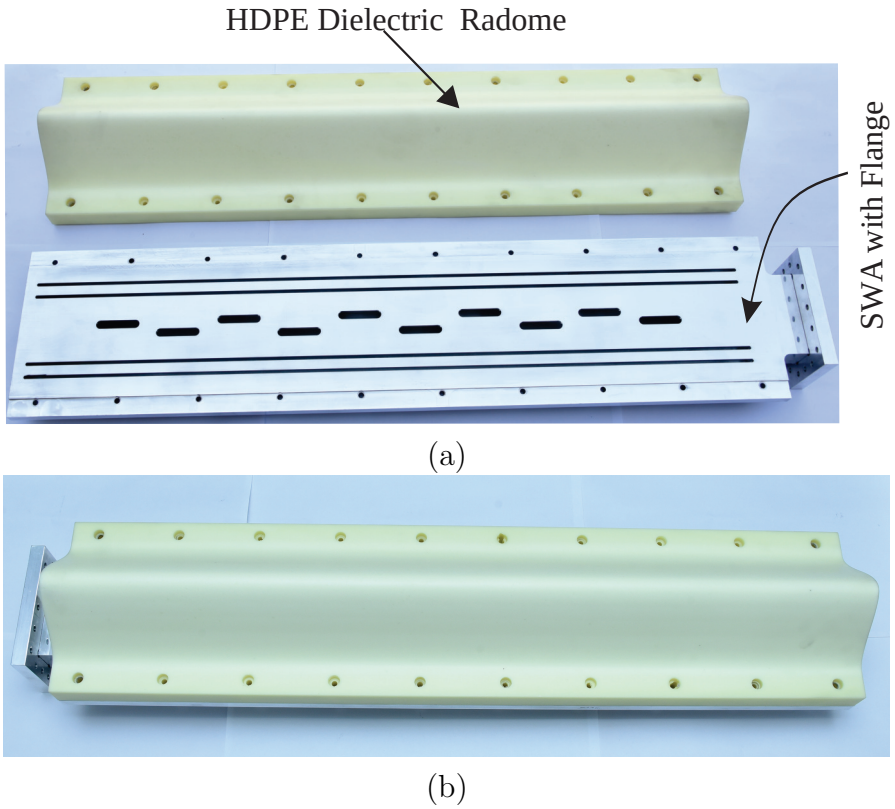

FIGURE 6.15: Fabricated (a) SWA and dielectric radome and (b) full assembly.

The simulated and measured reflection coefficient of the proposed SWA is depicted in Fig. 6.16. The ripples observed in the experimental data of S_{11} are presumably due minor RF leakages caused by the fabrication error in the structure. A measured reflection coefficient of more than 20 dB is achieved at the 3 GHz frequency band without a dielectric radome (see Fig. 6.16 (a)), while in the presence of a dielectric radome, a reflection coefficient value of 18 dB is achieved, as illustrated in Fig. 6.16 (b). The simulated SWA results have good agreement with the measured ones. A little shift in the reflection coefficient is observed due to the fabrication errors and tolerances.

The proposed SWA, with and without dielectric radome, far-field radiation performance is measured in the near-field antenna measurement setup under an anechoic environment as illustrated in Fig. 6.17. The aperture field distribution with and without dielectric is depicted in Fig. 6.18. It can be observed that all slots are radiating properly and contribute to far-field radiation characteristics.

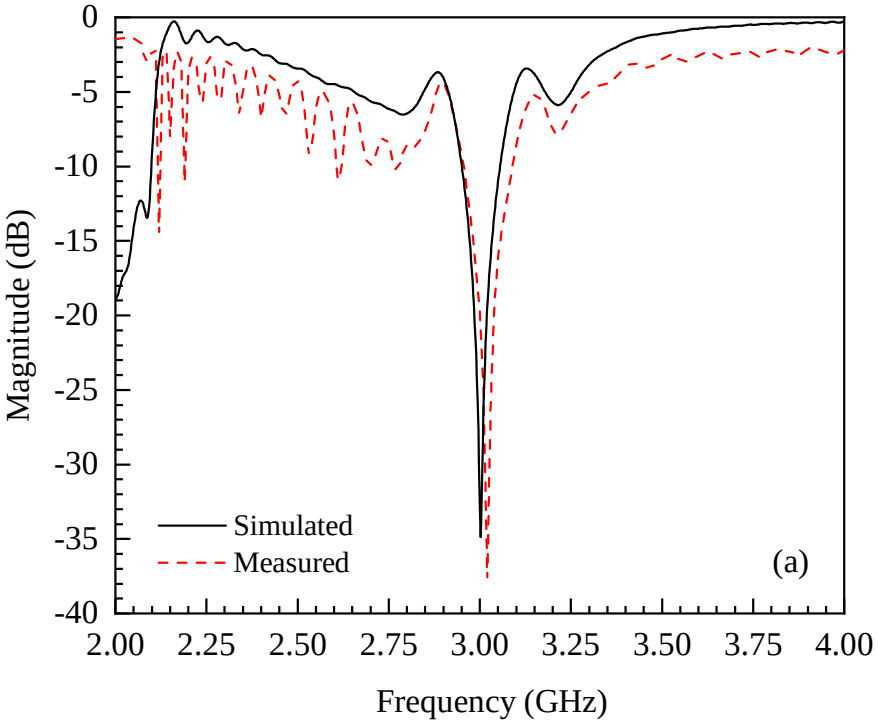

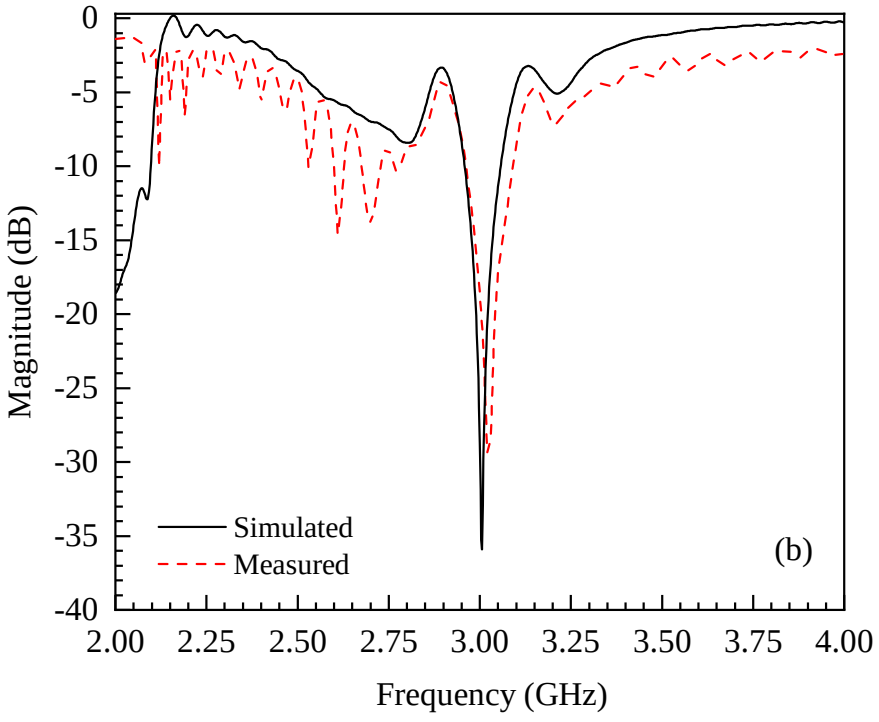

FIGURE 6.16: Simulated and measured reflection coefficient of proposed SWA antenna (a) without and (b) with dielectric radome.

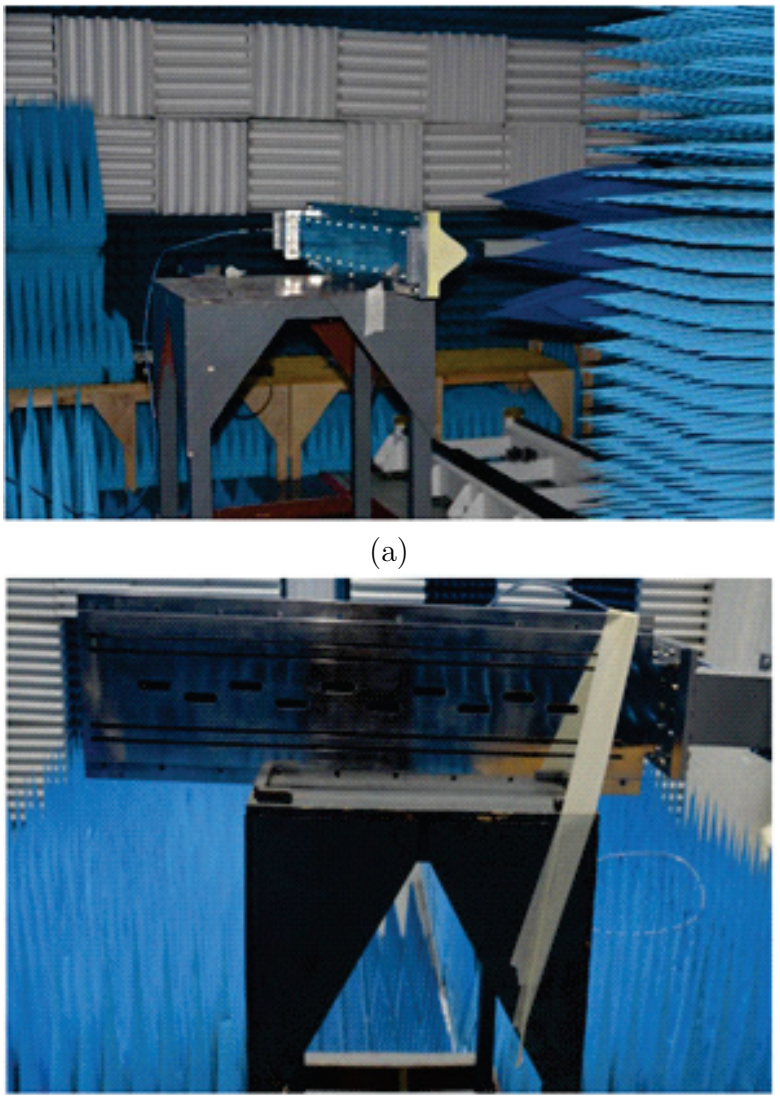

(a)

(b)

FIGURE 6.17: SWA prototype under testing (a) without and (b) with dielectric radome.

The simulated and measured E and H-plane radiation characteristics with and without dielectric radome are shown in Fig. 6.19 and 6.20. The radiation patterns in the H-plane are perfectly matched with minor distortion in some regions, which is within acceptable limits. However, a significant mismatch in E-plane is observed between simulated and measured patterns due to fabrication errors and measurement setup limitations. We have used the near field antenna measurement setup to assess the radiation pattern of SWA. This setup can only scan the front side i.e. -90 to $+90$ degree and did not allow full 3D scanning which limits the E-plane radiation pattern to $\pm 9^{\circ}$. Simulated and measured result comparison is

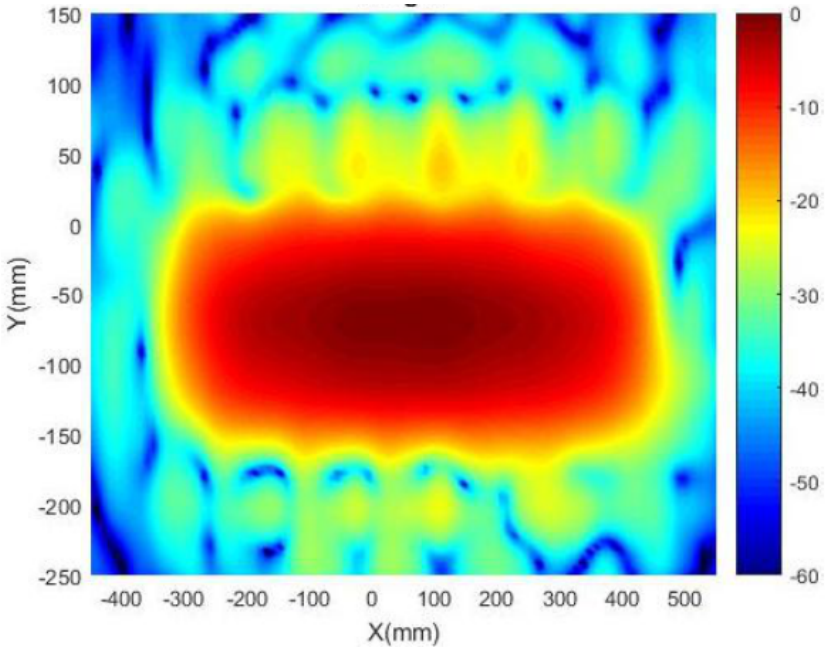

(a)

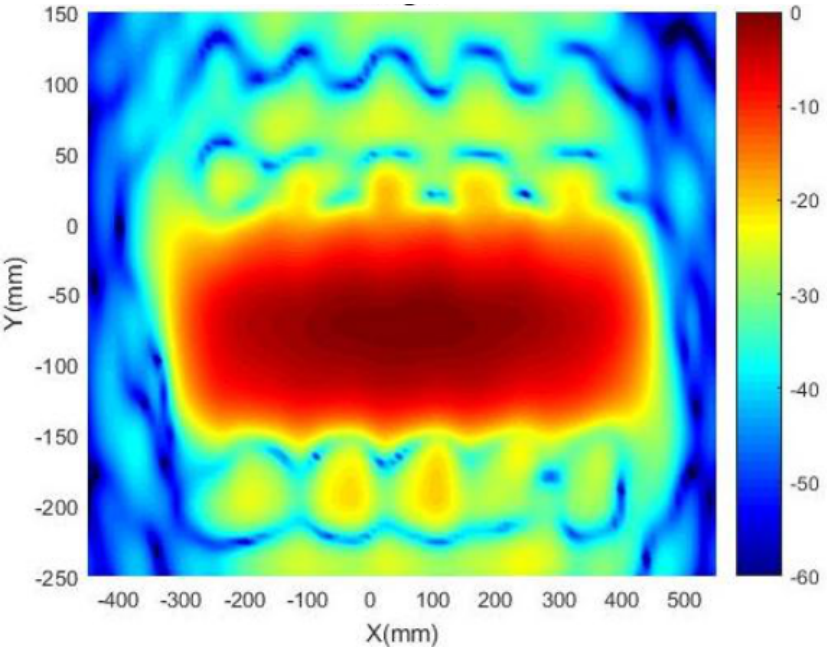

(b)

FIGURE 6.18: Aperture distribution of SWA prototype under anechoic environment (a) without and (b) with dielectric radome.

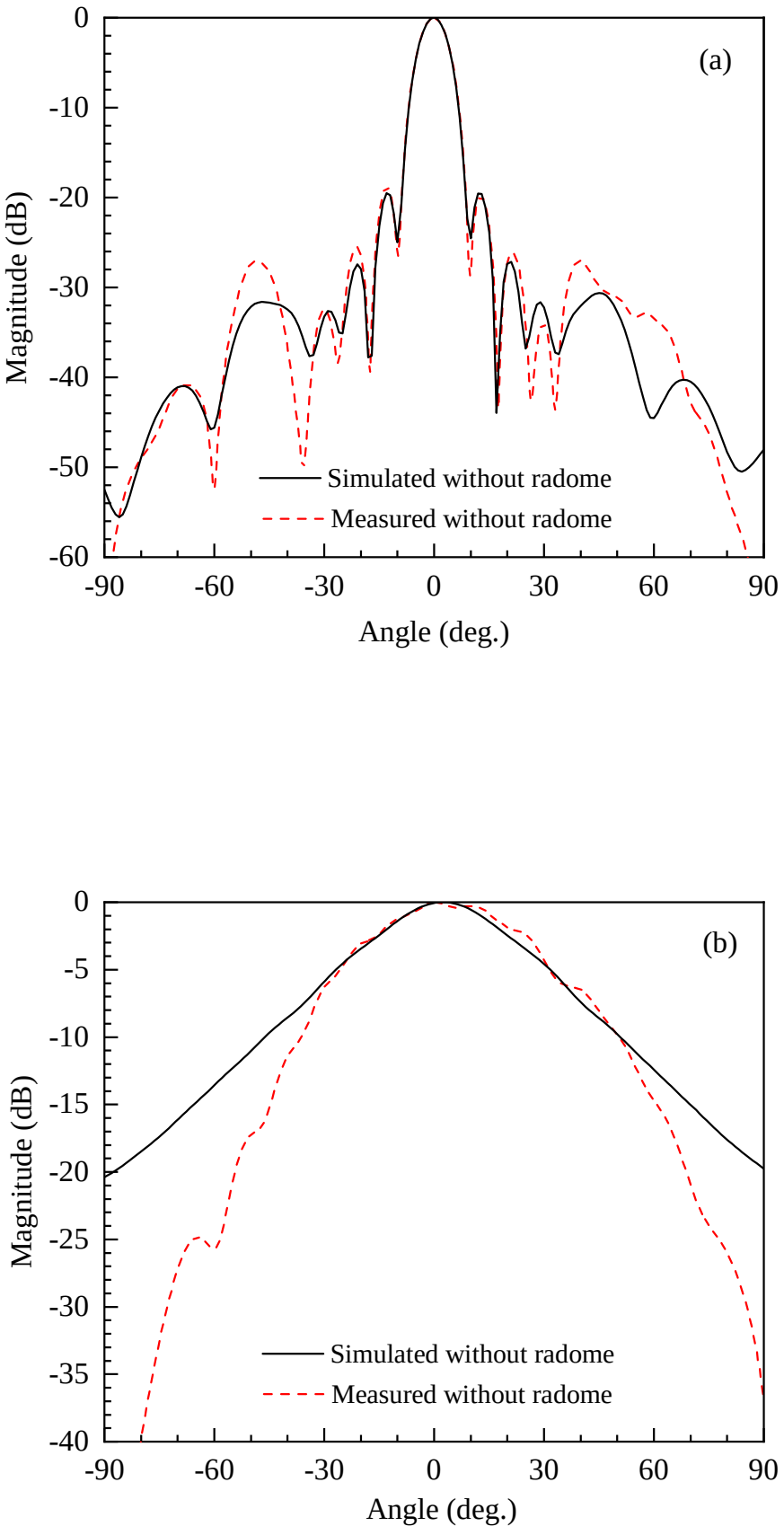

FIGURE 6.19: Simulated and measured (a) H- and (b) E-plane radiation characteristics without dielectric radome.

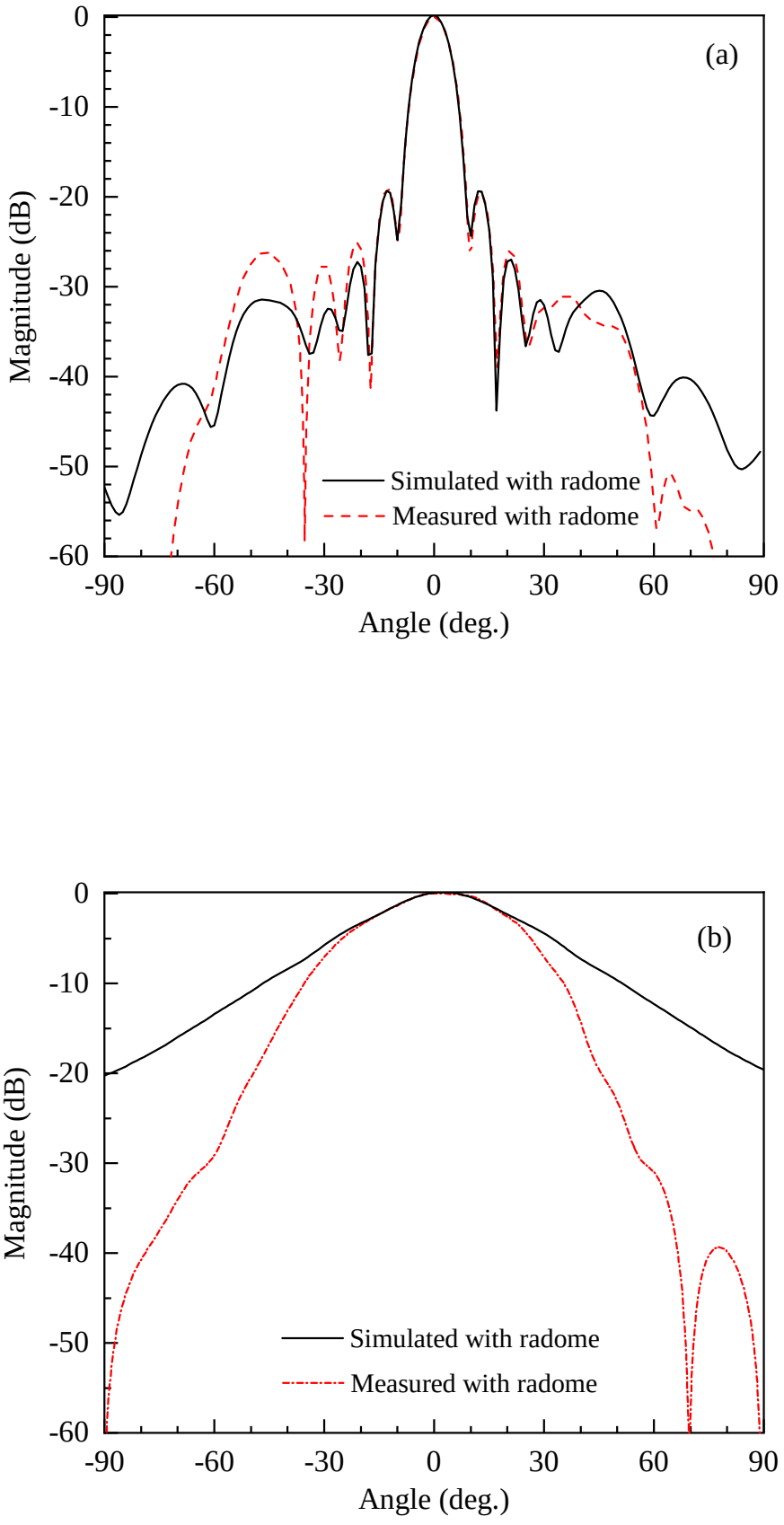

FIGURE 6.20: Simulated and measured (a) H and (b) E-plane radiation characteristics with dielectric radome.

TABLE 6.6: Simulated and measured SWA performance parameters comparison.

Performance Parameters	**SWA + Two Grooves**	**Two Grooves + Gaussian Radome**
Sim. Gain (dBi)	19.1	20.1
Mea. Gain (dBi)	19.24	19.95
Sim. Beam-width (E/H-plane)	52.1°/8.1°	42.4/8.1
Mea. Beam-width (E/H-plane)	46.65°/8.04°	39.48/8.02
Sim. SLL (dB) (E/H-plane)	−21.7/−20.6	−22.1/−21.0
Mea. SLL (dB) (E/H-plane)	−/−18.3	−/−19.4
Sim. Return Loss (dB)	−35	−30
Mea. Return Loss (dB)	−28	−26

given in Table 6.6.

6.6 Summary

In this chapter, an improved SWA system is proposed for HPM applications in S-band. To achieve a 20 dB SLL, 10 rounded-edged slots are etched on the broad side wall, and their displacement/offset around the centre-line is achieved by using a modified Gaussian distribution. The antenna design is based on the commonly used Elliot's slotted waveguide antenna design procedure. The gain of conventional SWA is enhanced by using the inside-groove and dielectric Gaussian dielectric radome. A peak gain of 20.1 dBi is achieved with SLL less than 20 dB in both planes, with no significant back and side lobes. The proposed design can be used for array antennas as the groove will play a vital role in minimizing the mutual coupling between the elements as well as for efficient beamforming and steering capability.

Chapter 7

Slotted Waveguide Array Antenna

7.1 Introduction

In the past few years, high-power microwave (HPM) technology has become popular for both civilian and military applications. There are many HPM devices and systems in the world, like active denial systems which are used as a non-lethal weapons to fortify a defence system. Electronic devices and circuits can be damaged/disrupted by HPM weapons since many commercial applications such as WiFi modules, wireless CCTV cameras, UAVs and Bluetooth devices typically operate in S-band. Maximum damage occurs when the frequency of the HPM device is the same as that of the target device. Additionally, due to the relatively large size of the transmit antenna, a gigawatt (GW) HPM signal can be achieved in S-band without breakdown. [130, 131].

In an HPM system, the transmit antenna has a very crucial role [97, 103, 132]. It is an established fact that the efficiency of an entire HPM system depends upon its radiating antenna. The antenna elements handle HPM pulses and transmit them in the air without attaining breakdown. The most popular antenna in an HPM system is the horn antenna, which is widely employed due to its simpler design.

However, it cannot provide an efficient beam directivity and its beam scanning capability is also limited [133]. A controlled beam scanning with high power handling capacity and low SLL are considered crucial parameters for an HPM system. A practical realization of such a system is a challenging task, because of the design complexity and mechanical movement of the antenna. Furthermore, the movement of a large mechanical structure defining an HPM system causes large power consumption in addition to an associated inertia which may generate a delay to hit the target [133]. To overcome these limitations, different HPM antenna array systems have been proposed in [57, 134–137]. But one of the major restrictions in these designs is large SLL both in azimuth and elevation planes.

A 4-element grooved structure based SWA configuration is reported in [135]. In this design, unwanted coupling between the elements of antenna was addressed by employing grooves in between the elements of array. This technology restrained the mutual coupling (MC) of the slots. A significant improvement in beam scanning was also achieved by integrating the choked region without making any compromise on 3 dB gain.

The groove structures in the slotted array configuration is used for a dual purpose i.e., MC reduction and gain enhancement. The MC among the array elements degrades the beam scanning ability of the system and causes backward power flow i.e., towards the source. These are the critical issues in the design of a phased array antenna with large beam steering requirements [134]. The unwanted MC among the array elements is overcome by using different techniques including but not limited to inter-element spacing, metal wall integration, frequency selective surfaces, metamaterial structures, and grooved regions [101, 112, 138]. Finding an optimum slot spacing eliminates nulls and grating lobes, and is considered a challenging task in the design of an HPM phased array antenna. The transmission and beaming effects of SWAs can be enhanced by incorporating grooved structures near the slots, which result in improved radiation characteristics by reducing MC. These customized regions help in suppressing the surface wave propagation as observed in choke structures. The re-distribution of electromagnetic waves in the

slotted regions produces high surface currents and MC, which can be suppressed effectively by incorporating a grooved structure appropriately [114, 139].

A 10-slot based rectangular SWA configuration integrated with non-periodic grooves and dielectric radome is reported in [138]. The integration of one-dimensional corrugated grooves re-radiate the EM waves to the targeted direction by properly optimizing the period, width, position, and depth. This antenna configuration offered a gain of 20.1 dBi with significant suppression in the back-lobe of the antenna. Moreover, dielectric radome was also deployed to maintain the radiation characteristics without compromising the performance parameters. A beam steerable SWA is presented in [112]. The C-shape slots were cut on the narrow wall of the waveguide to feed the spiral helical unit elements to achieve circular polarized waveform. A gain of 26.3 dBi was achieved with wide angle beam scanning capability, whereas, a maximum of 2 dBi gain degradation was reported during the beam scanning [136].

In [140], the authors proposed a leaky wave antenna array to improve gain and impedance matching. The array configuration was properly coupled with a 48-way power divider for an efficient far-field radiation pattern. An optimized SWA integrated grooved structure can be employed to avert impedance matching issues, especially in the presence of a secondary source. The grooved structure in an array formation suppresses the undesirable surface currents which as a result improves isolation. Properly decoupled array elements provide efficient wide angle beam scanning capabilities with minimum grating lobes emergence.

In SWA, high power handling might require that the system should be operated in vacuum or in the presence of a suitable gaseous environment such as SF_6 or N_2 to improve E-field breakdown. For this purpose, SWA should be enclosed with a suitable structure that should help in maintaining the high amplitude radiation characteristics of SWA [141–143]. Such a structure could be a radome provided it would not disturb the radiation characteristics of the array. If such a radome is appropriately designed, it would also contribute to immune the system from its vicinity. Therefore, a proper design of the radome is required to reduce the impact

on high magnitude radiation parameters and to improve the performance of the HPM system. Moreover, proper analysis of radome structure along with antenna structure design is required to improve the radiation performance of the system in totality.

In this chapter, an efficient SWA has been designed, fabricated and tested for HPM applications. To achieve HPM capabilities, rectangular waveguide loaded with optimally designed grooves along with high density polyethylene (HDPE) radome have been investigated. It has been demonstrated that the integration of grooves in an array configuration reduces MC, improves radiation patterns and provides a wide-range beam scanning ability. Moreover, a dielectric radome is designed to allow the HPM functionalities of the SWA aperture under a specific ambient. The organization of the remaining parts of the chapter is that section 7.2 briefly outlines the design of the grooved SWAA system whilst section 7.3 gives details pertaining to SWAA fabrication and measurements. Finally, the conclusions drawn from this research are presented in section 7.4.

7.2 Inside-Grooved Slotted Waveguide Array Antenna

The purpose of this section is to design and analyze SWAA with grooved structures. To assess the role of a radome in achieving controlled radiation ambient at the aperture of SWAA, and to develop a 1×4 waveguide based PD to realize a complete system. Also, a comparison is made between the conventional and proposed design of SWAA by considering directivity, SLL, MC and beam steering. The target variables to realize a good SWAA system, have been identified and listed in Table 7.1. The reason for selecting the slotted waveguide antenna element for array configuration is low mutual coupling between the elements due to inside groove structure and efficient beam scanning capability compared to conventional SWA array configuration. The radiation pattern of E and H-plane is at

TABLE 7.1: Target design parameters of slotted waveguide array antenna (SWAA) for high power microwave applications.

Design Variables	Target Values
Operating frequency	3 GHz
Directivity	Higher than 25 dBi
Return loss	Less than −20 dB
Mutual coupling	Less than −20 dB
SLL in H-plane	Less than −20 dB
Number of slots	10
Number of elements	04

same angle (90°) and the proposed design offers high power handling capability which is essential for HPM devices like magnetron.

7.2.1 One to Four (1×4) Power Divider (PD)

Power dividers are widely employed in communication systems and RADAR with the purpose to feed elements of an array antenna. The main requirement for designing a PD is that it should have low insertion loss, equal power division, same output phase, and the ability to handle high power such as GW. Due to high power handling requirements, waveguide based PD is employed to feed an antenna array system meant for HPM applications.

As listed in Table 7.1, the required 1×4 PD was designed using standard WR-284 waveguide dimensions. The main designing constraints of the target PD were, the amplitudes and phases of signals at its output ports relative to the signal given at its input. To ensure equal output amplitude, which in this case was −6 dB, the length of waveguides was chosen equal to the wavelength of central frequency (λ_0). Under this condition, the output phases will also be the same, however, a possible mismatch between input and output ports due to non-equal prorogation delay is controlled by placing a septum (small cylindrical rod) at a particular position. This resulted in minimum reflections and maximum transmission from input to output, hence ensuring synchronized output signals [144–146]. The simulation has been performed in CST microwave studio (MWS). The top and cut-view of 1×4

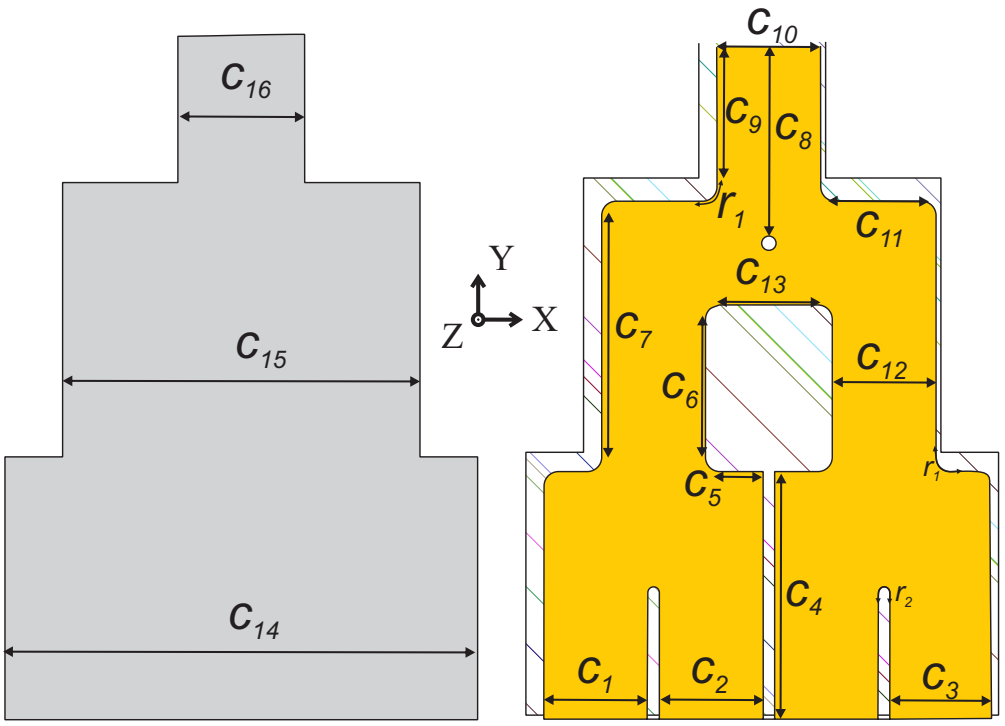

FIGURE 7.1: Top and cut-view of waveguide based 1×4 power divider (PD) to feed slotted waveguide array antenna (SWAA).

PD are shown in Fig. 7.1, whereas, the dimensions of the proposed design are explained in Table 7.2.

The magnitude of reflection parameter S_{11} along with various transmission parameters $(S_{12}, S_{13}, S_{14}, S_{15})$ are shown in Fig. 7.2. The plots of Fig. 7.2 show $S_{11} = -40$ dB with an output amplitude of -6 dB from all output ports of the PD. This confirms that, from input to output, the power has been divided in equal parts. For efficient beam forming the signals at the output ports of the PD should be in phase. Fig. 7.3 shows the output phases of 1×4 PD, which are almost overlapping and hence, the phases are synchronized. The position of the septum was optimized by doing parametric analysis as shown in Fig. 7.4(a). The graph shows that for $C_8 = 137$ mm, there were minimal reflections and maximum transmission from input to output, thus ensuring synchronized output signals with equal power division at the output ports of the PD [144–146]. Additionally, the power flow pattern of the designed PD is illustrated in Fig. 7.4(b). It can be seen from the

TABLE 7.2: Various dimensions (mm) of a 1×4 waveguide based power divider (PD) as shown in Fig. 7.1.

Variable	Value
C_1	72.14
C_2	72.14
C_3	72.14
C_4	180.14
C_5	30.07
C_6	95.86
C_7	168
C_8	137
C_9	100.92
C_{10}	72.14
C_{11}	60.14
C_{12}	72.14
C_{13}	68.14
C_{14}	328.56
C_{15}	248.42
C_{16}	88.14
r_1	10
r_2	4

figure that the power is equally distributed from input to output, which exhibits a uniform power flow across each port of the PD.

7.2.2 Design of Inside-Grooved Based Slotted Waveguide Array Antenna (SWAA)

The proposed slotted waveguide array antenna consists of 4 elements and 10 slots. Each element is separated by an inside groove to minimize MC and to increase the directivity of SWAA. In this section, first the single element of grooved SWAA will be discussed followed by the complete design of SWAA along with its simulated results.

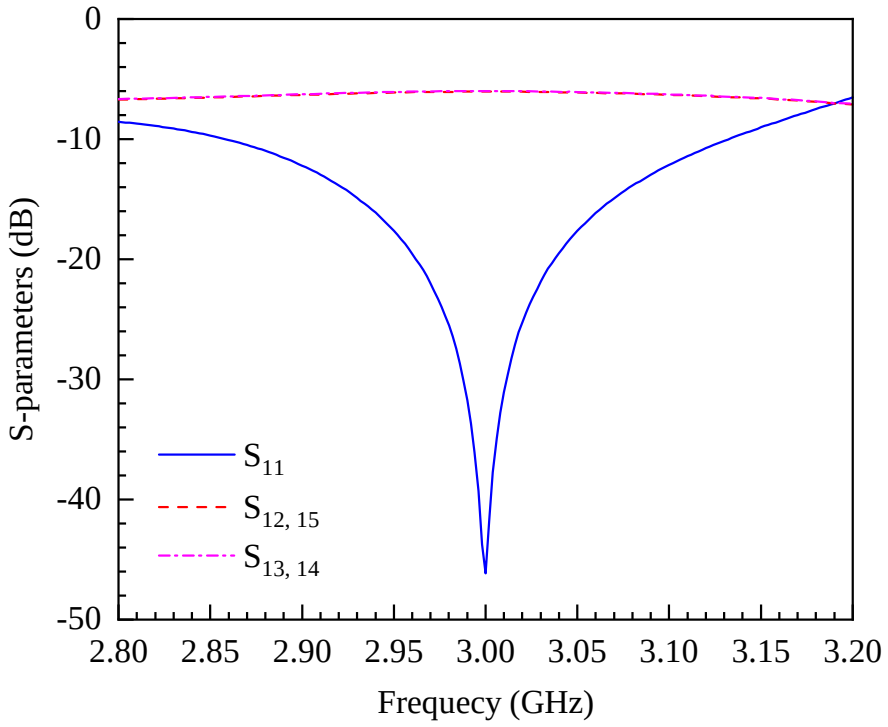

FIGURE 7.2: Reflection (S_{11}) along with transmission parameters ($S_{12}, S_{13}, S_{14}, S_{15}$) of a 1×4 power divider

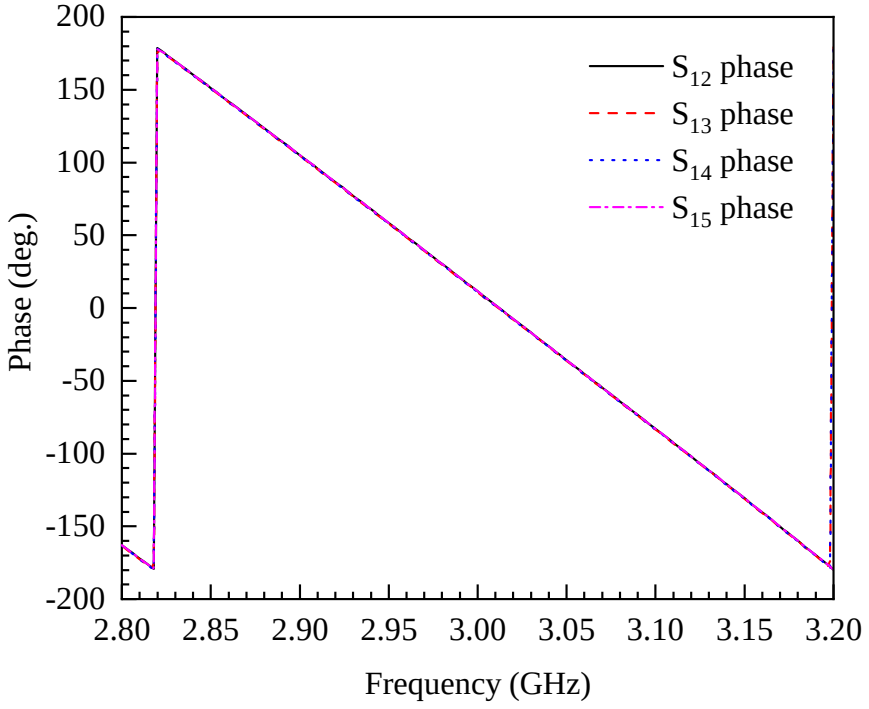

FIGURE 7.3: Output phases of a 1×4 power divider

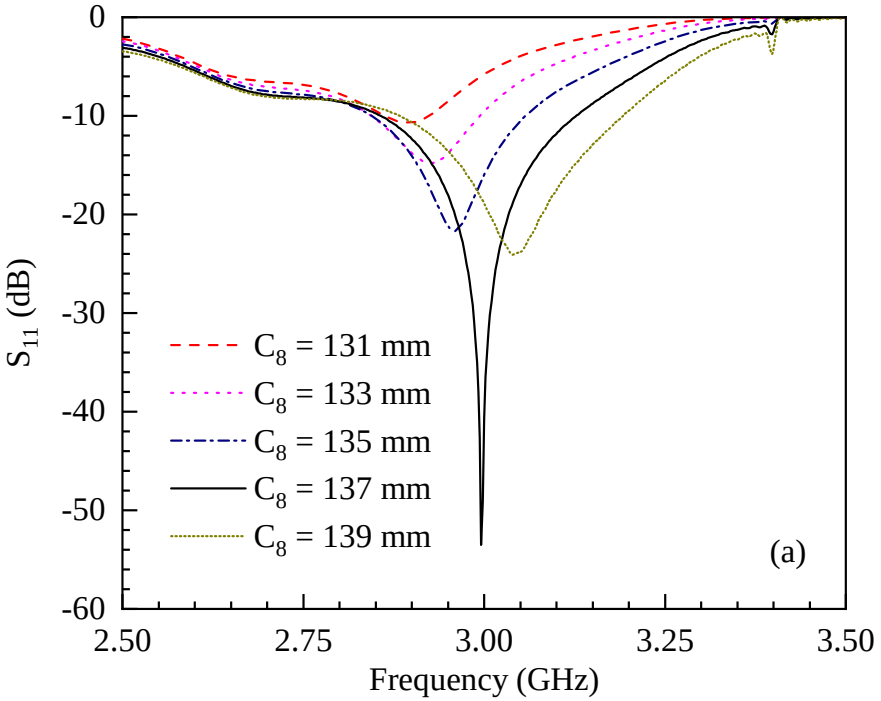

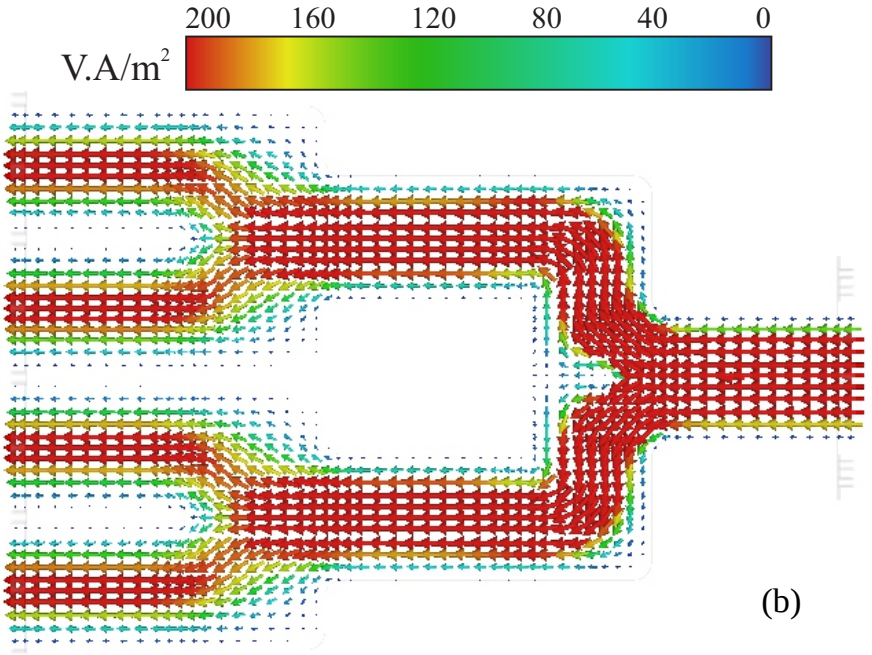

FIGURE 7.4: Simulation of 1:4 Power divider (a) Affect of Septum on S_{11} (b) Power flow distribution

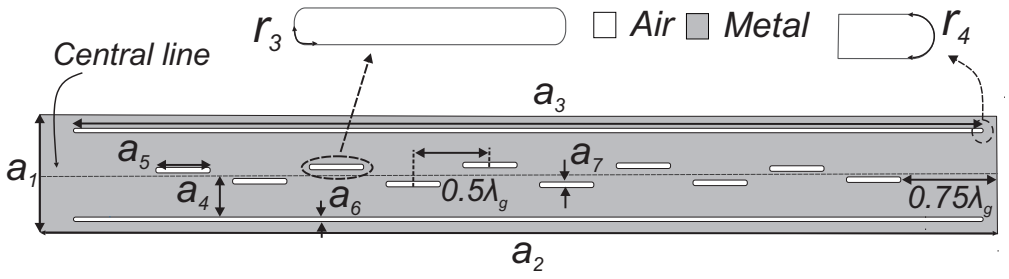

FIGURE 7.5: Single element of a grooved slotted waveguide antenna (SWA) (a_1 = 88.14 mm, a_2 = 890 mm, a_3 = 817 mm, a_4 = 40.07 mm, a_5 = 49.42 mm, a_6 = 4 mm, a_7 = 10 mm, λ_g = 138.5, r_3 = 5 mm, r_4 = 2 mm)

7.2.2.1 Single Element Grooved SWA

In this section, the single inside grooved-based slotted waveguide antenna has been analyzed. The detailed design and analysis of grooved structure in slotted waveguide antenna, its significance for suppression of surface current on the aperture, designing equations and slots distribution using Gaussian profile to achieve desired SLL with optimum directivity are discussed in [138, 147]. In [147], the authors also described that the use of Gaussian shape dielectric radome enhances power handling capability along with the directivity of SWA.

A standard WR-284 (a = 72.14 mm, b = 34.04 mm) waveguide is used to design and simulate the single grooved-based slotted waveguide antenna for 3 GHz frequency as shown in Fig. 7.5. The depth of the groove on wall of the waveguide is about 0.23 λ_0 with 0.04 λ_0 and 8.17 λ_0 as its width and length, respectively. The technique results in surface current suppression on the aperture of the antenna. The Gaussian profile slots distribution has been applied to achieve the desired SLL of at least −20 dB. The coefficient and the corresponding position of 10 slots are given in Table 7.3 [138]. The slots have round edges to avoid electric field concentration and local scattering. The guided wavelength for WR284 waveguide at f_0 = 3 GHz is 138.5 mm, which is calculated using Eq. 7.1 :

$$\lambda_g = \frac{\lambda_0}{\sqrt{1 - (\lambda_0/\lambda_{cutoff})^2}} \tag{7.1}$$

TABLE 7.3: Gaussian distribution coefficients and slot displacement from the central line of SWA

Slot	Gaussian Coefficients	Slots Displacement (mm)
1	1.000	4.5936
2	1.4474	5.5432
3	2.3194	8.3332
4	3.1914	8.9273
5	3.6388	8.9273
6	3.6388	8.3332
7	3.1914	5.5432
8	2.3194	7.0599
9	1.4474	5.5432
10	1.000	4.5936

7.2.2.2 Grooved Slotted Waveguide Array Antenna (SWAA)

The SWA elements are placed with a gap of less than half of the operating wavelength, to avoid grating lobes in the radiation pattern. The prime purpose of the grooved structure is to constraint surface current distribution within the respective surface area of the array element with the aim to improve directivity and reduce MC between the adjacent elements. The design, therefore, has 4 radiating elements with 7 grooves in total. The side and top view of the 4 elements array antenna used for CST simulation, is shown in Fig. 7.6.

The RL plot of SWAA is shown in Fig. 7.7. It can be seen that at the target frequency i.e., 3 GHz, the antenna gives minimum reflections; validating the perceived design. It can also be seen from the plots of the figure that the S_{22} and S_{33} values, which represent the middle two elements, are although within well allowed margin yet they are relatively poor. It is further observed that the magnitude of S_{22} and S_{33}, as a function of frequency, is identical and their associated central frequency is slightly shifted relative to S_{11} and S_{44}. A plausible explanation of this minor variation between two sets of reading, i.e. [S_{22}, S_{33}] and [S_{11}, S_{44}], could be associated with the variation in their respective structure. Array elements at the shoulder of the antenna have two side grooves, as evident from Fig. 7.6, whereas, two middle elements of the array contain one groove on each side. Hence, there

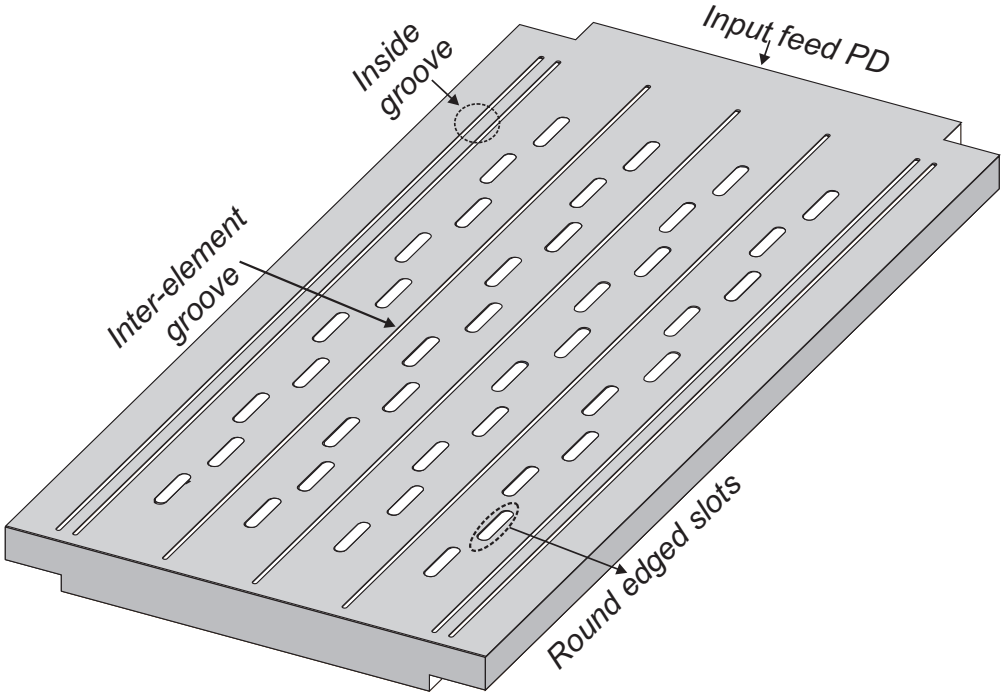

(a)

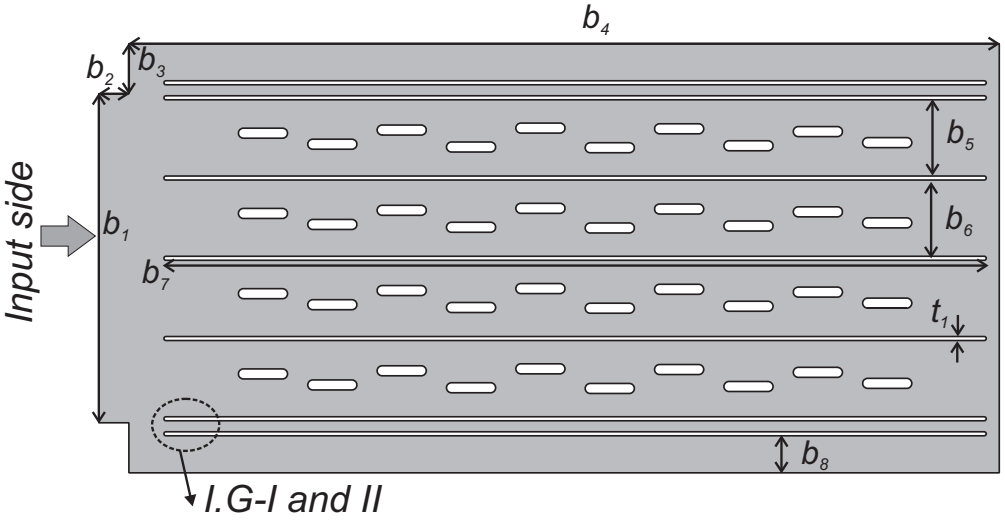

(b)

FIGURE 7.6: (a) 3D view and (b) top view of grooved slotted waveguide array antenna (SWAA) for high power microwave systems. The dimensions of various variables shown in the figure are: depth of I.G-I = 23 mm, I.G-II = 20.8 mm, b_1 = 328 mm, b_2 = 30 mm, b_3 = 50 mm, b_4 = 869 mm, $b_{5,6}$ = 76.14 mm, b_7 = 817 mm, b_8 = 37 mm, t_1 = 4 mm

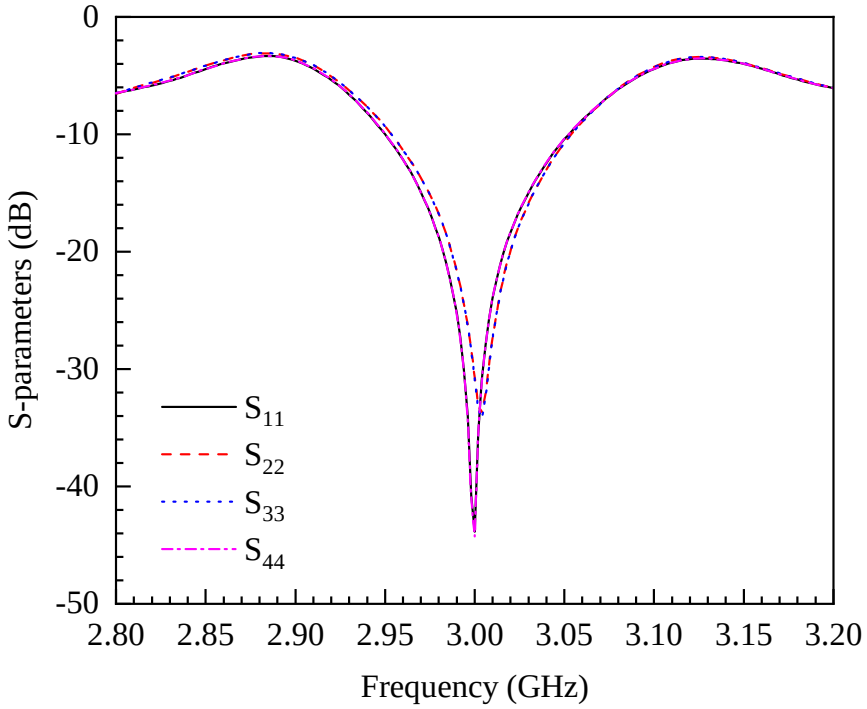

FIGURE 7.7: Reflection (S_{11}) plot of slotted waveguide array antenna (SWAA)

are two sets of responses that are identical to each other, i.e S_{22} is the same as S_{33} likewise S_{11} and S_{44}. Since majority of the input power is transmitted by the antenna as RL of the antenna is less than -30 dB (Fig. 7.7), therefore, the magnitude of residual power in the band of interest is supposed to be very low and hence, its contribution to reflect the propagating signal is assumed to be negligible.

Fig. 7.8 shows MC values between the elements of SWAA which around the frequency of interest is below -22.4 dB. These values of MC are realized by appropriately introducing the groove structure inside the wall of the waveguide. It can be seen from the plot of Fig. 7.8 that MC between elements 2 and 3 is relatively higher compared to element 1 and 4. However, the attained values are still reasonably well within the allowed margin of targeted design values. The associated reason of this variation could be the same as that offered in the case of reflection coefficients variation earlier. It is pertinent to mention here that reduction in MC is considered an essential component of an array antenna design to achieve high directivity and efficient beam forming. It has been noticed that the introduction of a groove in SWAA structure reduces the propagation of surface

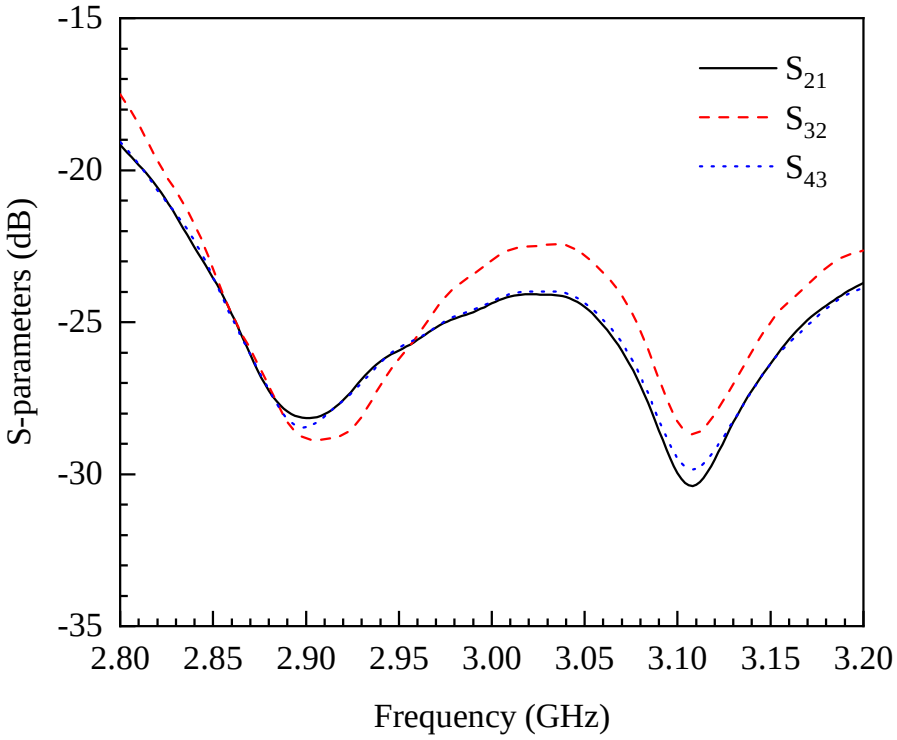

FIGURE 7.8: Mutual coupling (MC) between different elements of slotted waveguide array antenna (SWAA)

current between the elements as shown in Fig. 7.9. To compare the conventional SWAA with the proposed groove-based SWAA, the surface current propagation between the two designs has been simulated by exciting element 3 of both the design and shown in Fig. 7.9(a,b). It can be seen that there is a significant surface current spread in conventional SWAA [Fig. 7.9(a)], especially at the center of the waveguide, which eventually increases MC between the elements. The same is restricted to the respective element in the case of grooved geometry as evident in Fig. 7.9(b). To observe the holistic view of surface current confinement, all four inputs of the grooved structure have been excited simultaneously and the effect is shown in Fig. 7.9(c). This figure clearly demonstrates that the groove structure constraints surface current reasonably well in their respective regions and resultantly, there would be a reduction in MC between array elements. The additional groove is added to further reduce surface current propagation at the edges of the antenna array to prevent radiation pattern deterioration.

To have a comparative analysis of the two designs, a) the un-grooved design referred to as the conventional design, and the grooved one, the MC profile of the

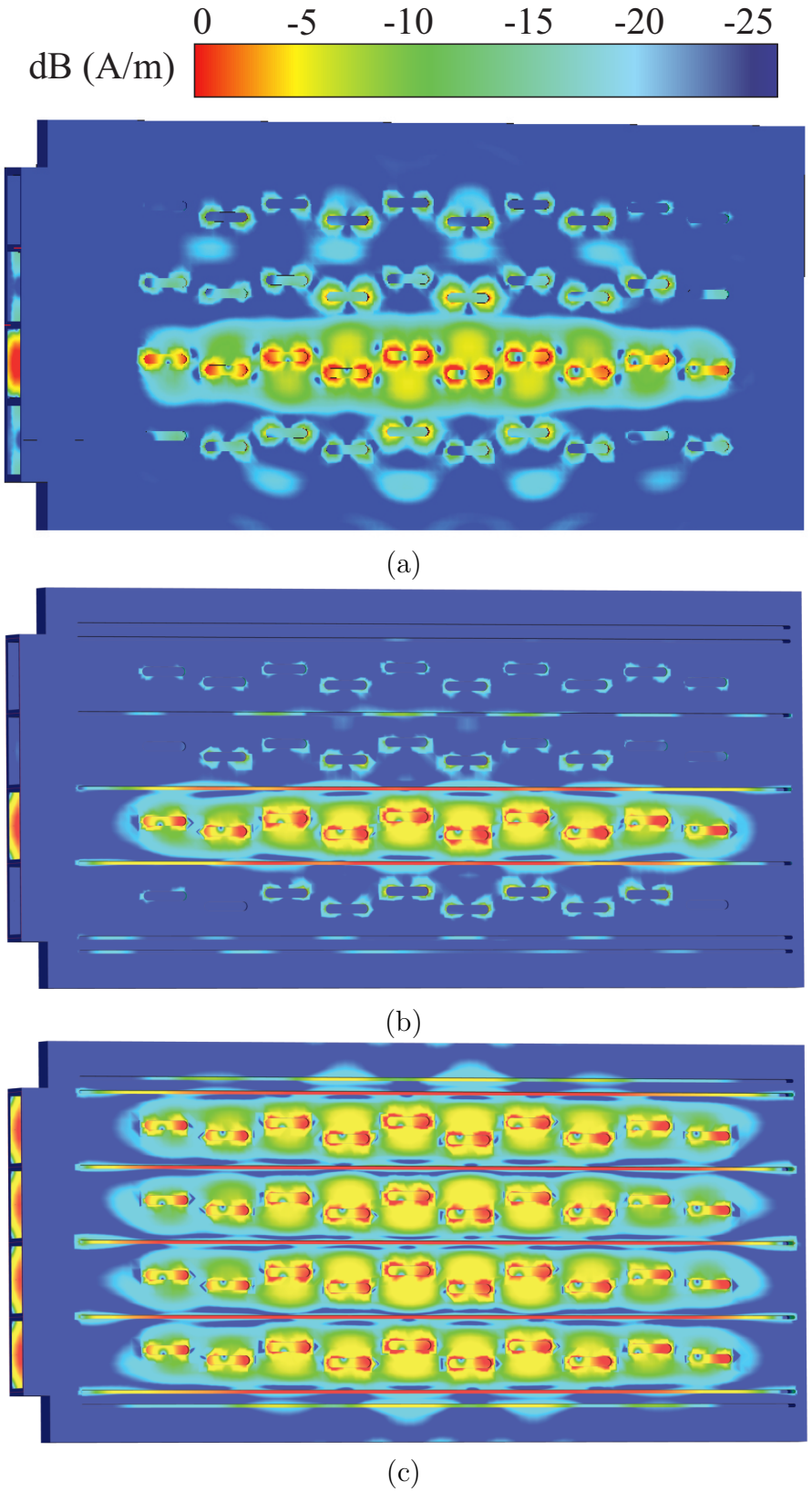

(a)

(b)

(c)

FIGURE 7.9: Surface current distribution pattern, in a four elements slotted waveguide array antenna, when only 3rd element of the array is excited (a) without (b) with groove structure and (c) when all elements are excited

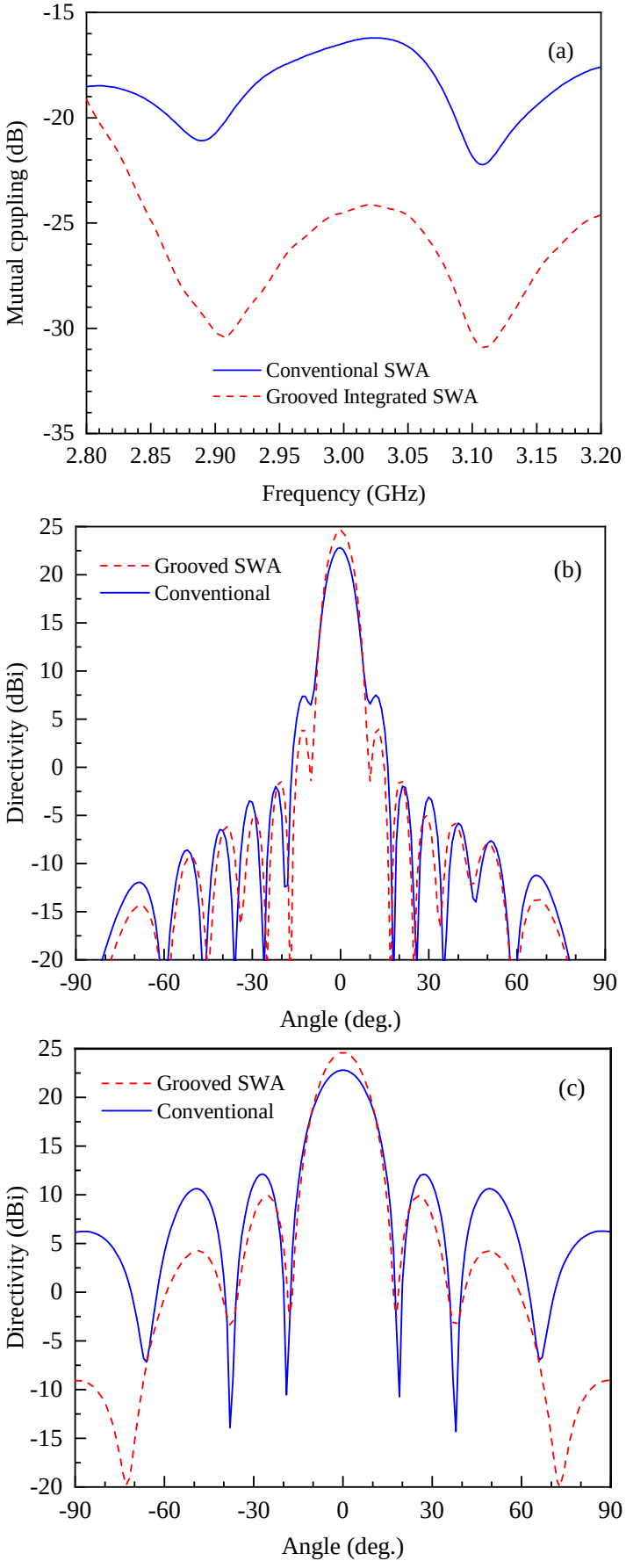

FIGURE 7.10: (a) Mutual coupling, (b) H-plane and (c) E-plane radiation patterns of conventional vs grooved slotted waveguide array antenna (SWAA)

designed antenna element 3 and 4, is shown in Fig. 7.10(a). It can be seen from the plot that in the grooved structure, the MC is less than −22 dB whereas, the conventional structure offers −16 dB at the frequency of interest. This is 37% higher than the grooved design. Such a high value of MC could eventually lead to deteriorated directivity of the system.

The H and E-plane radiation patterns of conventional and grooved SWAA are shown in Fig. 7.10(b,c). It can be seen that the H-plane radiation pattern of conventional SWAA has 8.8% less directivity than the grooved SWAA. Additionally, the main lobe profile is affected by the two upper lobes appearing in the shoulders of the main lobe. As shown in Fig. 7.10(c), the E-plane radiation pattern for the conventional SWAA also has a high value of grating lobes compared to the proposed design. In the nutshell, it can be said that in the given physical SWA structure, the proposed design, without adding any additional components, could enhance the operational performance of SWA, simply by manoeuvring the slot design and its surroundings.

The beam steering capability of the proposed SWAA design has also been analyzed and shown in Fig. 7.11(a). The beam steering was achieved by applying progressive phase shift from element-1 to element-4. It can be seen that the main lobe direction changes its position from 0° to 22° with minimal grating lobes. The variation in gain because of beam steering for the two designs under discussion is shown in Fig. 7.11(b). It can be seen from the plot that at the given beam steering, the directivity of proposed SWAA is better than the conventional SWAA by 2.1 dBi with low magnitude of grating lobes as well. This shows that the proposed design offers 13% improved performance than the conventional design. The performance summary of the two designs has been tabulated and presented in Table 7.4. In Ref. [135], Yong et.al. presented a 4-element waveguide-based array antenna for L-band high power applications. The reported values of Yong *et al.* design are also listed in Table 7.4. It can be seen from the data that the proposed design is 16.6% better in RL relative to Yong's design, 7.4% at zero angle directivity and it offers 9.7% improved directivity at 22°.

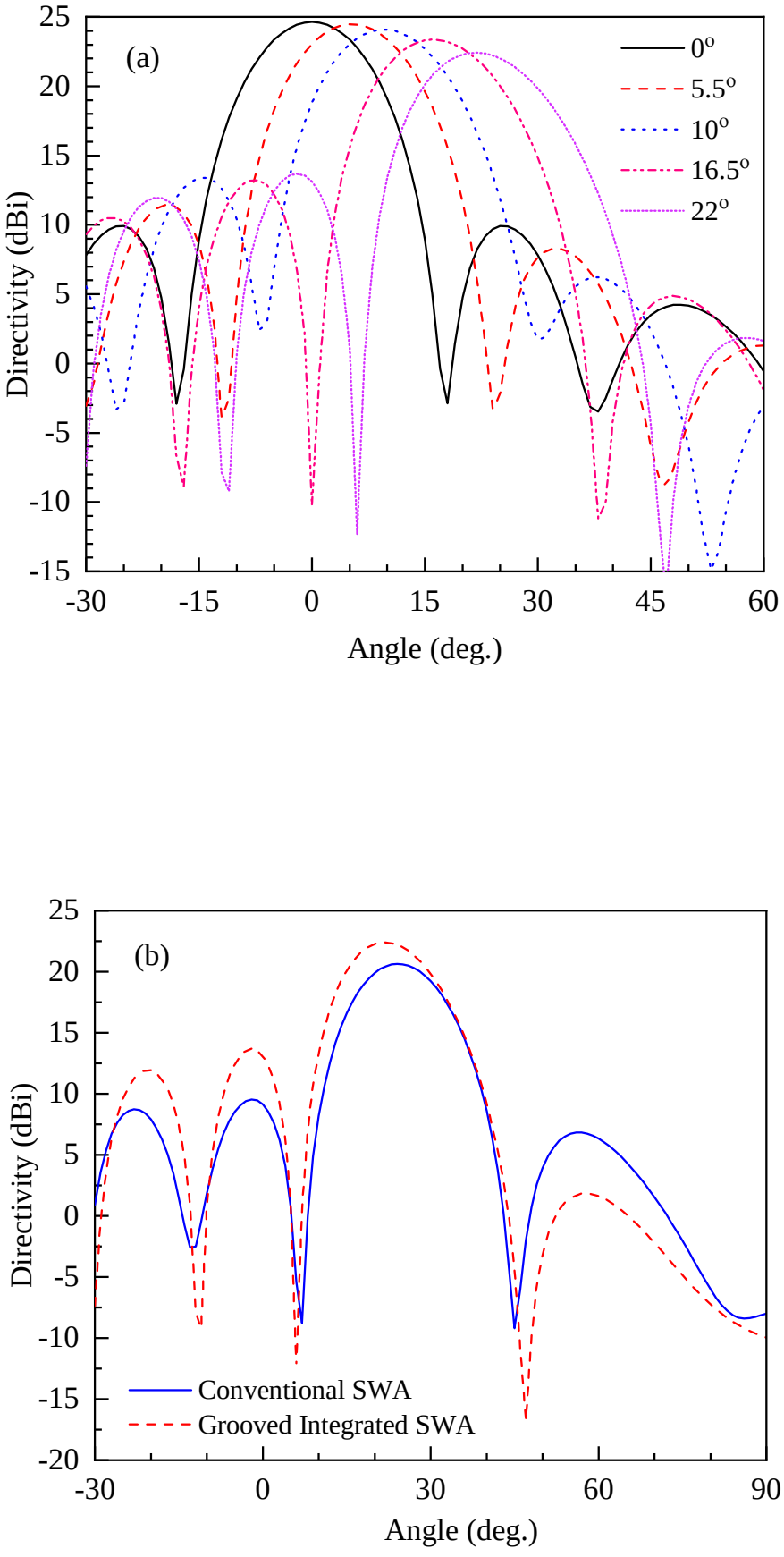

FIGURE 7.11: (a) Beam steering capability of a four element slotted waveguide array antenna (SWAA) system and (b) conventional (without grooved) vs proposed (with grooved) slotted waveguide array antenna (SWAA)

TABLE 7.4: Comparison of performance parameters of slotted waveguide array antenna (C-SWAA) vs the proposed grooved slotted waveguide array antenna (G-SWAA)

Antenna Type	RL (dB)	MC (dB)	Dir. at 0 ° (dBi)	Dir. at 22 ° (dBi)
C-SWAA	−28	−16.5	22.6	20.46
G-SWAA	−30	−25	24.6	22.54
Ref. [135]	−25	–	22.91	20.5

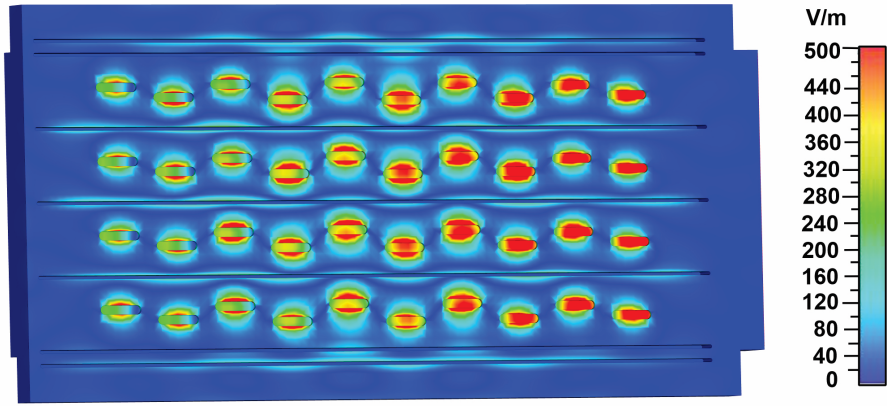

(a)

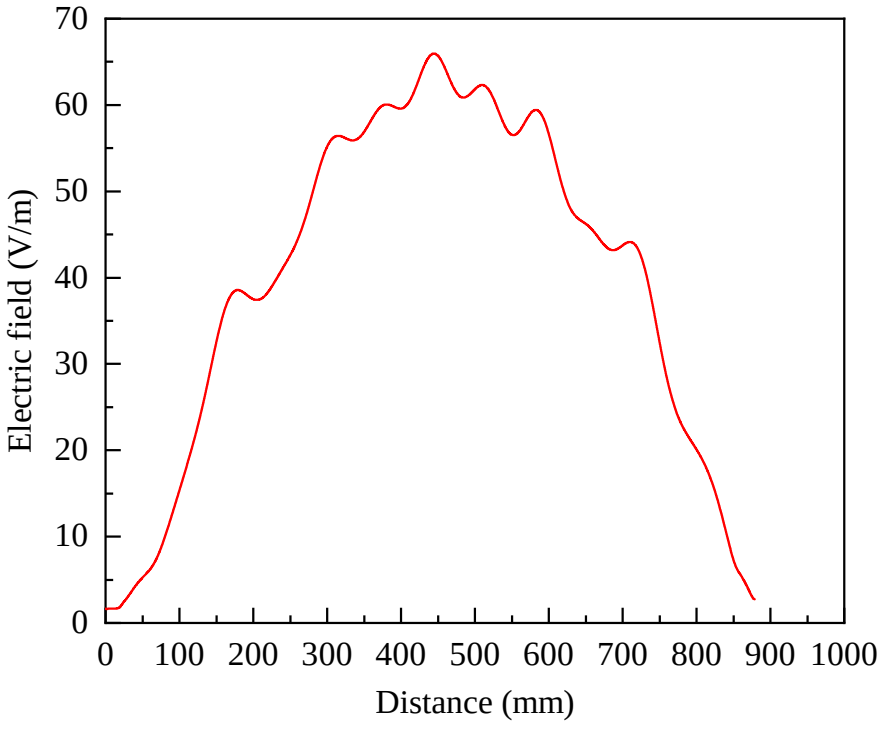

(b)

FIGURE 7.12: Electric field variation (a) at aperture and (b) at radome of a 4-element array antenna when excited with 0.5 W input signal

To calculate power handling capacity; the electric field distribution on the aperture of SWAA is simulated and shown in Fig. 7.12. The maximum electric field intensity on the antenna aperture is 500 V/m (Fig. 7.12a) when the structure is excited with an input power $P_{in} = 0.5$ W. This leads to power handling capacity at the aperture, P_A, as

$$P_A = \frac{P_{in}(E_{GB})^2}{(E_{ant})^2} = \frac{0.5 \times (25 \times 10^6)^2}{(500)^2} = 1.25 \text{ GW} \tag{7.2}$$

where E_{GB} represents waveguide breakdown field.

In SWA, high power handling sometime may require the holding of the antenna under vacuum or in a specific gas ambient such as SF_6 or N_2 to prevent early E-field breakdown or to improve the high power capacity of the system. For this purpose, SWA slots could be covered with an appropriate material such as a dielectric structure, which should maintain the radiation characteristics of the designed SWA array with improved high power handling capabilities. In this regard, a radome based on HDPE material ($\epsilon_r = 2.1$) was designed for the SWA array which could be employed either to create specific environment around the radiating array by injecting an appropriate gas or to create low pressure. The designed radome is shown in Fig. 7.13 along with its various dimensions. The radome is flat above the section where slots are situated to avoid unwanted reflections. The radome is called Gaussian due to its end section shape, as it has been designed by applying Gaussian curve to maintain radiation pattern characteristics. Figure 7.12(b) shows a variation in the electric field on the surface of the radome having its maximum value as 65 V/m, which leads to the power handling capacity, P_R, of the system as:

$$P_R = \frac{P_{in}(E_{AB})^2}{(E_{ant})^2} = \frac{0.5 \times (3 \times 10^6)^2}{(65)^2} = 1.06 \text{ GW} \tag{7.3}$$

where E_{AB} represents air breakdown field.

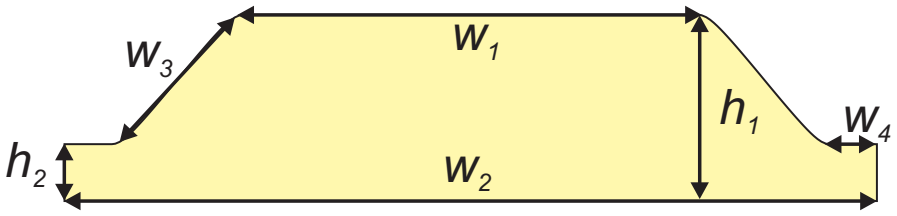

FIGURE 7.13: Dielectric radome for grooved slotted waveguide array antenna (W_1 = 240 mm, W_2 = 428 mm, W_3 = 68 mm, W_4 = 25 mm, h_1 = 98 mm, h_2 = 30 mm)

7.3 Fabrication, Measurements and Discussion

A 50 mm thick aluminum slab was used for the fabrication of waveguide power divider and array antenna. The designed SWA was fabricated on the chosen aluminum slab by using milling and surface finishing tools of a multitasking MANDELLI machine. The complete model of the grooved SWAA system with and without radome is shown in Fig. 7.14. As explained before, the purpose of a radome is to keep the radiating waveguide under a controlled environment to manoeuvre the high power handling capacity of the system. The fabricated 1×4 waveguide based power divider along with 4-element based antenna is shown in Fig. 7.15. In this image, Fig. 7.15(a) shows the top view of the power divider whereas, its cut-view is shown in Fig. 7.15(b). The fabricated slotted waveguide having four elements separated by inside grooved is shown in Fig. 7.15(c). The antenna physical size in terms of wavelength (λ_0 = 100 mm) is $8.46\lambda_0 \times 4.3\lambda_0 \times 1.47\lambda_0$. An assembled SWAA by integrating all the parts explained in Fig. 7.15, is shown in Fig. 7.16, in an anechoic chamber for experimentation. In this figure, Fig. 7.16(a) shows fabricated SWAA without radome whereas, Fig. 7.16(b) gives a pictorial view of fabricated SWAA with installed dielectric radome.

Rohde & Schwarz network analyzer, R&S ZNB20 was used to assess AC response of the array antenna. Near-field radiation pattern measurements were made using KEYCOM Model No. ANM01. Fig. 7.17 shows measured and simulated RL, E-plane and H-plane response of a fabricated without radome of a 4-element array antenna. The plot of Fig. 7.17(a) shows that experimental data though show some deterioration in S_{11} characteristics but yet it maintains the magnitude of S_{11} below

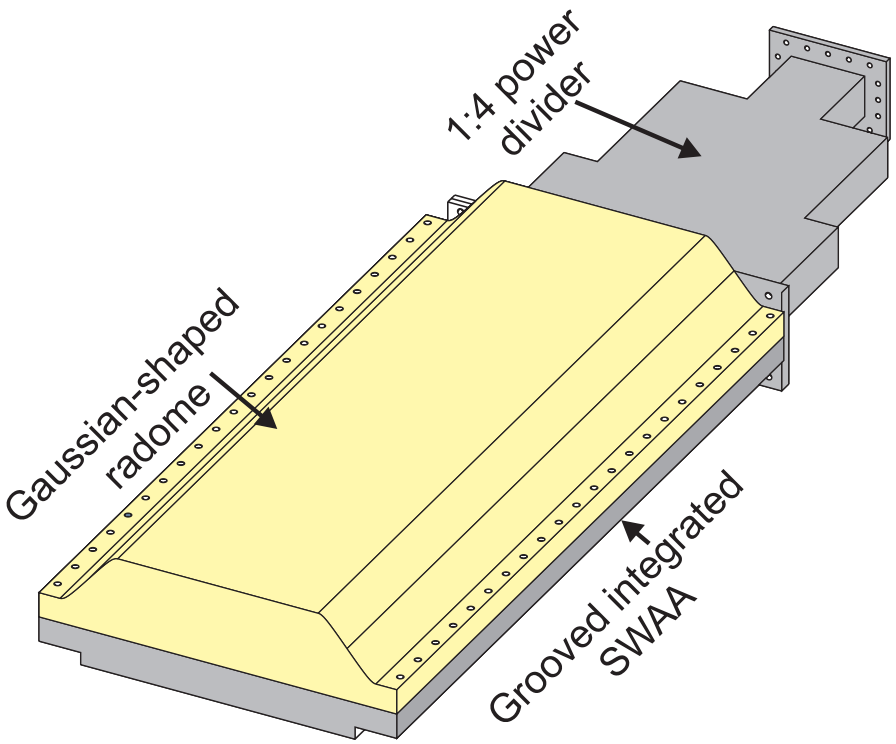

(a)

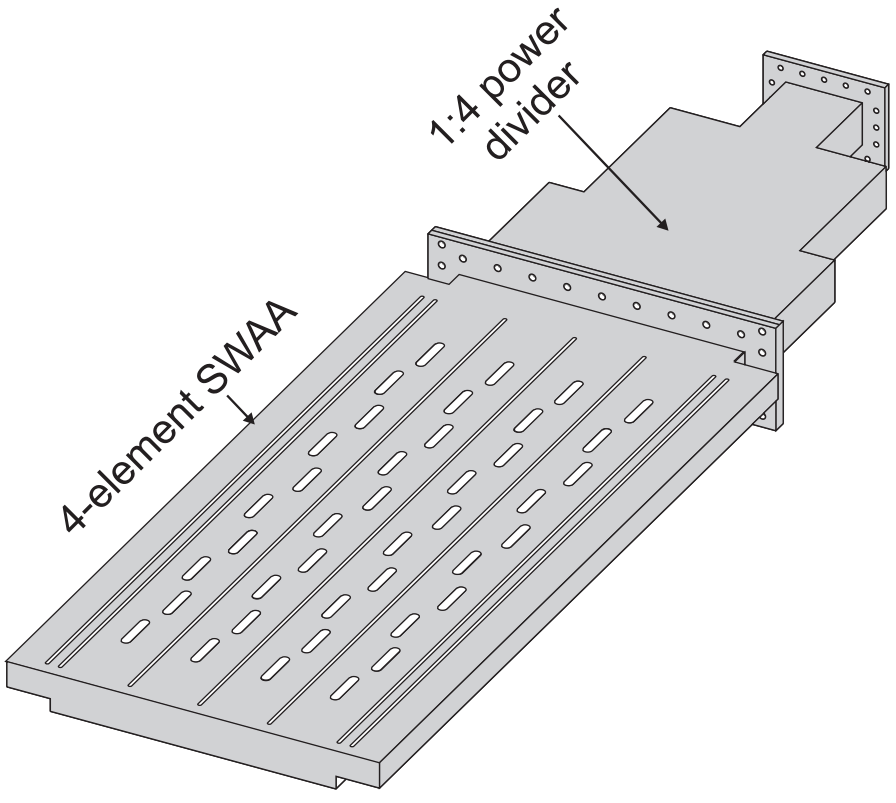

(b)

FIGURE 7.14: Complete physical illustration of a slotted waveguide array antenna (SWAA) (a) with and (b) without dielectric radome

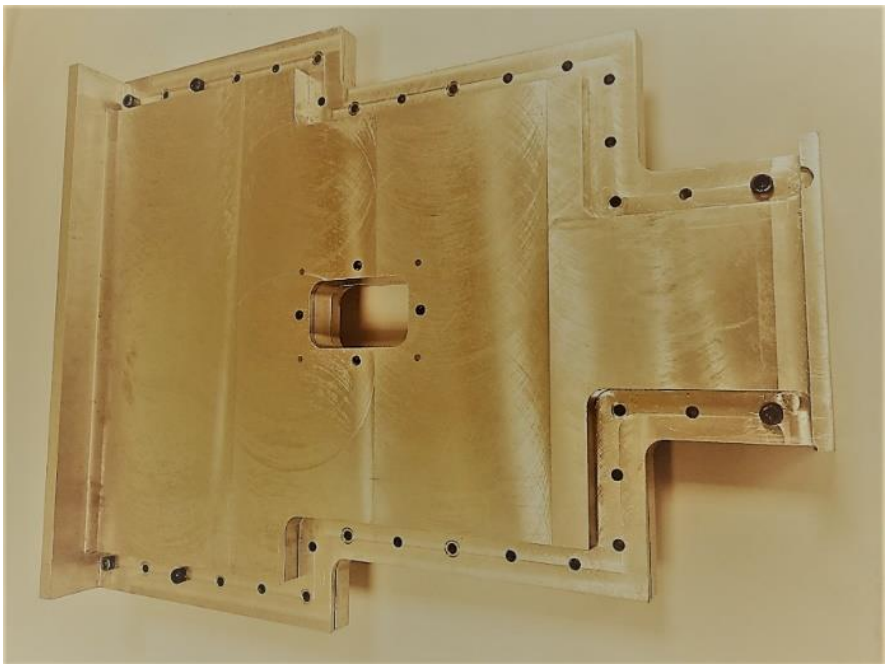

(a)

(b)

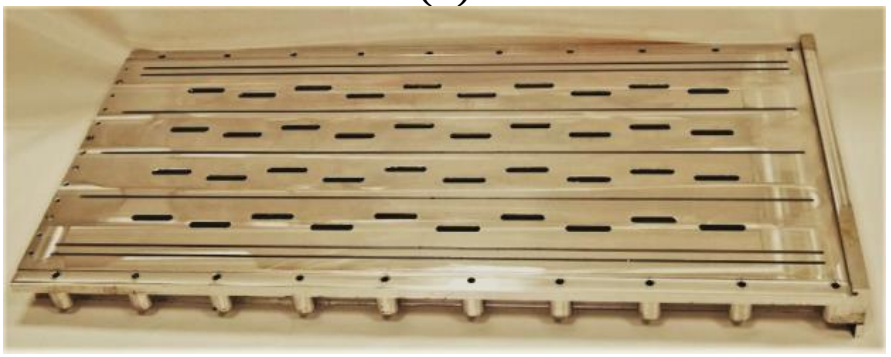

(c)

FIGURE 7.15: Components of fabricated slotted waveguide array antenna (SWAA): (a) top view of a 1:4 power divider, (b) crossectional view of the power divider and (c) 4-element slotted waveguide array with 7 inside horizontal groove

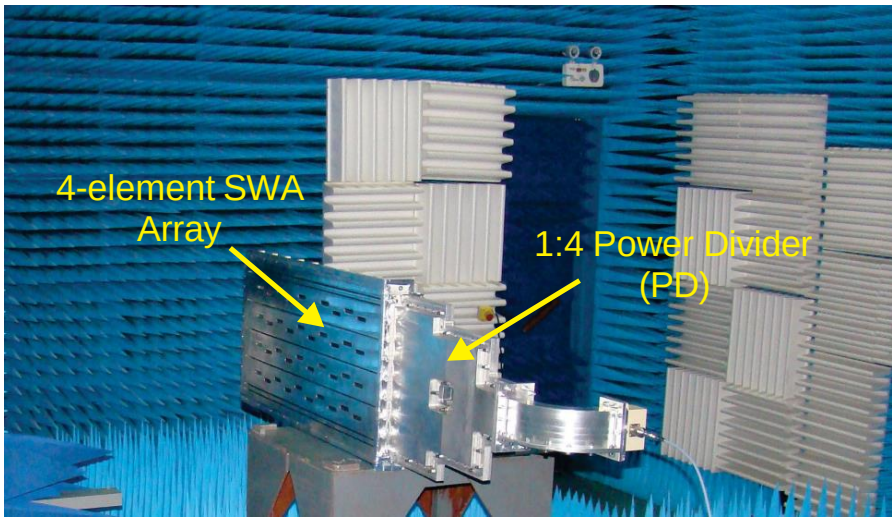

(a)

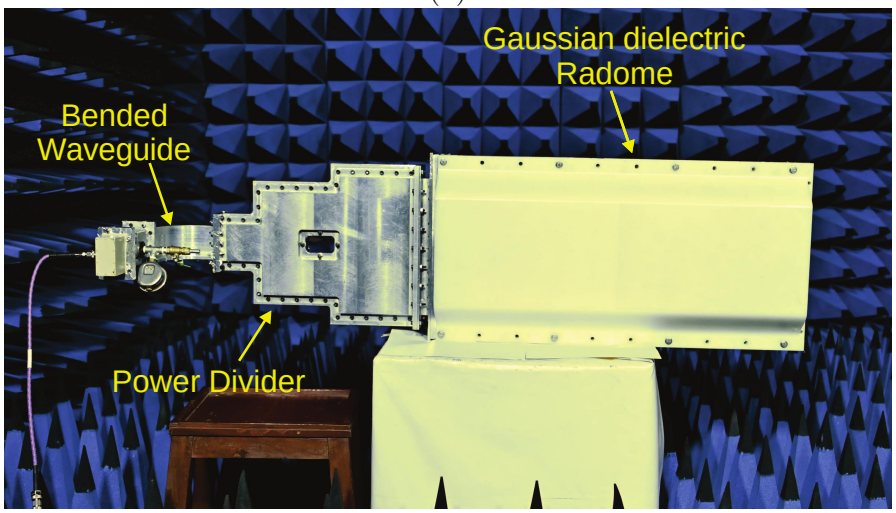

(b)

FIGURE 7.16: Pictorial view of an assembled slotted waveguide array antenna (a) without radome (b) with radome in an anechoic chamber for measurements

−20 dB at the central frequency for which it has been designed. The mismatch between simulated and observed characteristics could be associated to fabrication error tolerance and could be improved by improving fabrication technology. Plots of Fig. 7.17(b,c) also demonstrate that the simulated data is complying reasonably well with experimental measurements. Hence, this shows the proof of concept, and the proposed design can potentially be employed in HPM applications requiring GW energy.

On the other hand, Fig. 7.18 shows RL, electric and magnetic field radiation patterns of SWAA equipped with a dielectric radome as shown in Fig. 7.16(b).

The plots of the figure once again demonstrate that SWAA with radome maintains system characteristics and the observed S_{11} magnitude is about -25 dB, which is better than the one observed in Fig. 7.17(a). However, in this case, a slight shift in the experimental peak relative to simulated data of S_{11} is noted, as shown in Fig. 7.18(a). The shift is minor and may not cause a significant change in the overall performance of the system. The main lobes both for E-and H-plane radiation patterns, as shown in Fig. 7.18(b,c), comply well with experimental characteristics. This shows that the ambient defined by the natural gases around the array can be further controlled to customize maximum power handling capacity of the system.

Experimental and simulated gain as a function of frequency is shown in Fig. 7.19. As ascertained before both simulated and observed characteristics are matching reasonably well and the system at its central frequency exhibits a gain of $\sim$25 dBi, which showed 7% improvement relative to Yong's design [135].

A comparison has been made between the preposed design and earlier similar published work by using central frequency f_0, size of the antenna, aperture efficiency, η, and the associated gain. The data in this respect is shown in Table 7.5. The magnitude of η is evaluated using [148]

$$\eta = \frac{\lambda^2 G}{4\pi S_A} \tag{7.4}$$

where G is the gain and S_A is the surface area of the antenna. Examining the data of Table 7.5, it can be seen that the proposed SWAA offers a competitive performance and could be a considered a potential design for high power microwave applications. The aperture efficiency of the proposed design is relatively better than the other designs listed in Table 7.5. This improved performance could be associated with the reduced MC values (-25 dB) due to optimally designed grooved structure on the broad-side walls of the waveguides.

The cold test of the array antenna beam steering measurements were performed using JFW Industry programmable phase shifter assembly 50PSA-102-06, and

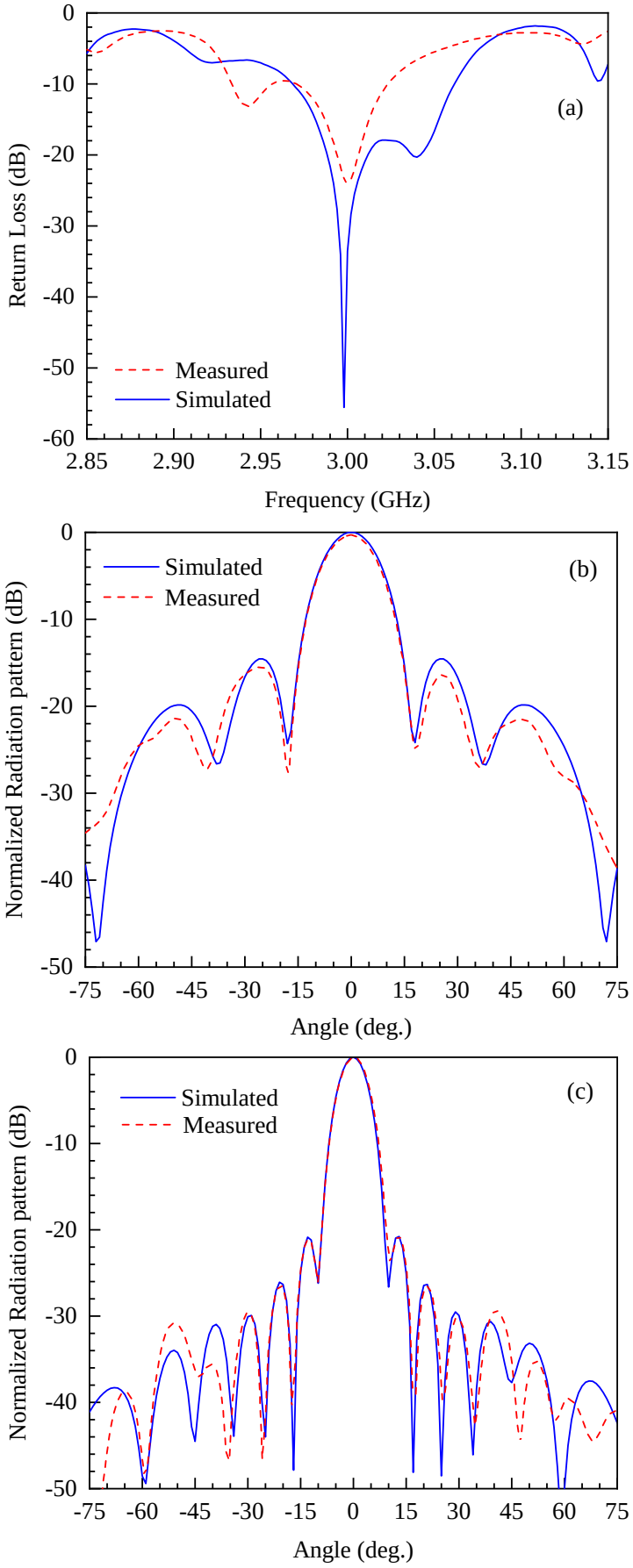

FIGURE 7.17: Measured and simulated radiation pattern of a 4-element slotted waveguide array antenna (without radome): (a) return loss, (b) E-field (c) H-field

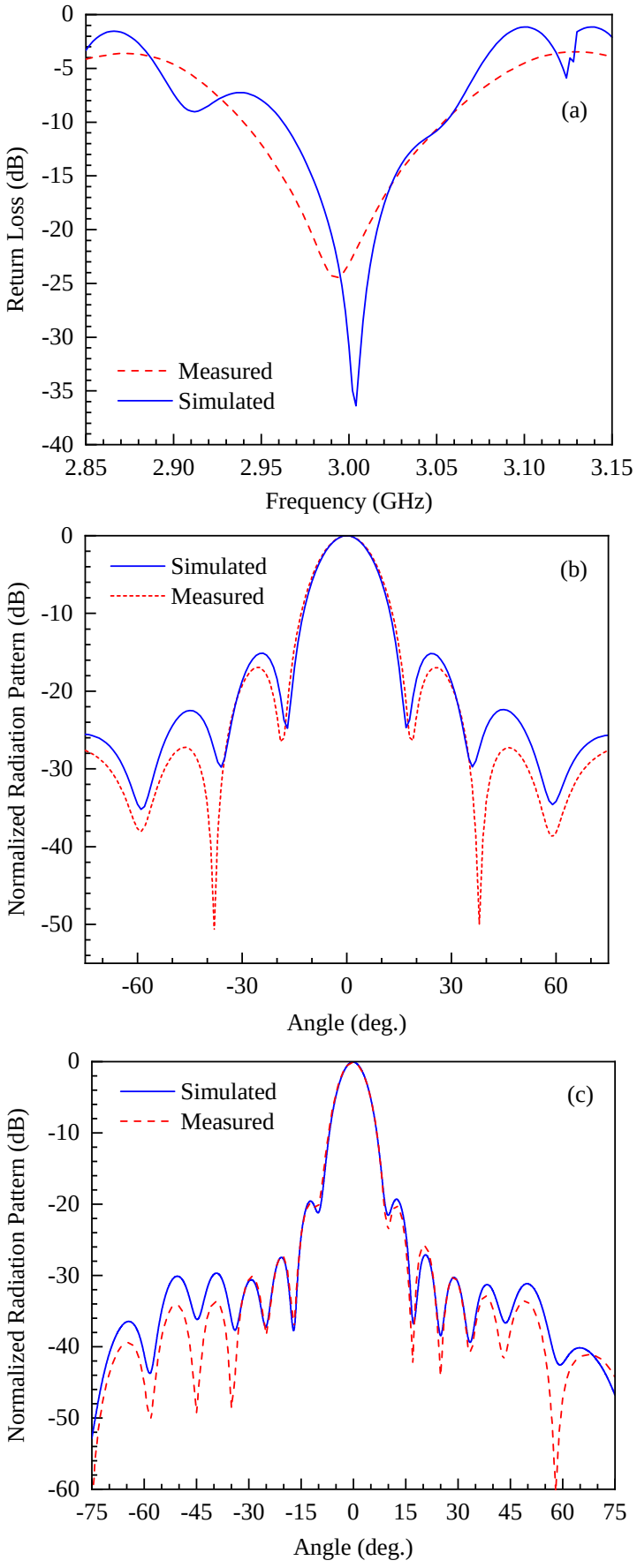

FIGURE 7.18: Measured and simulated response of a 4-element slotted waveguide array antenna with radome: (a) return loss, (b) E-field (c) H-field

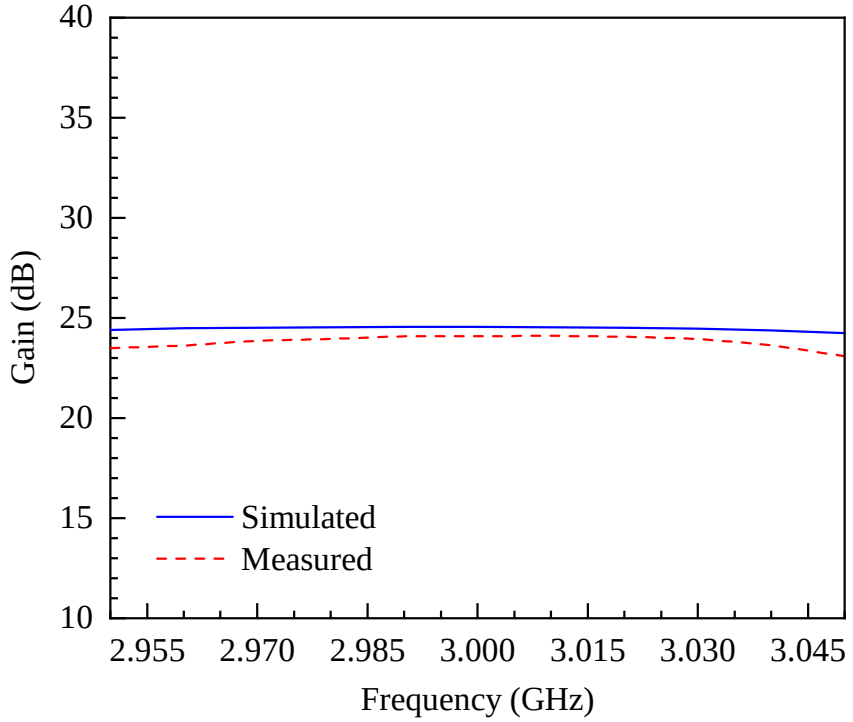

FIGURE 7.19: Observed and simulated gain of a 4-element slotted wave guide array antenna (SWAA) across its central frequency, f_0 =3 GHz

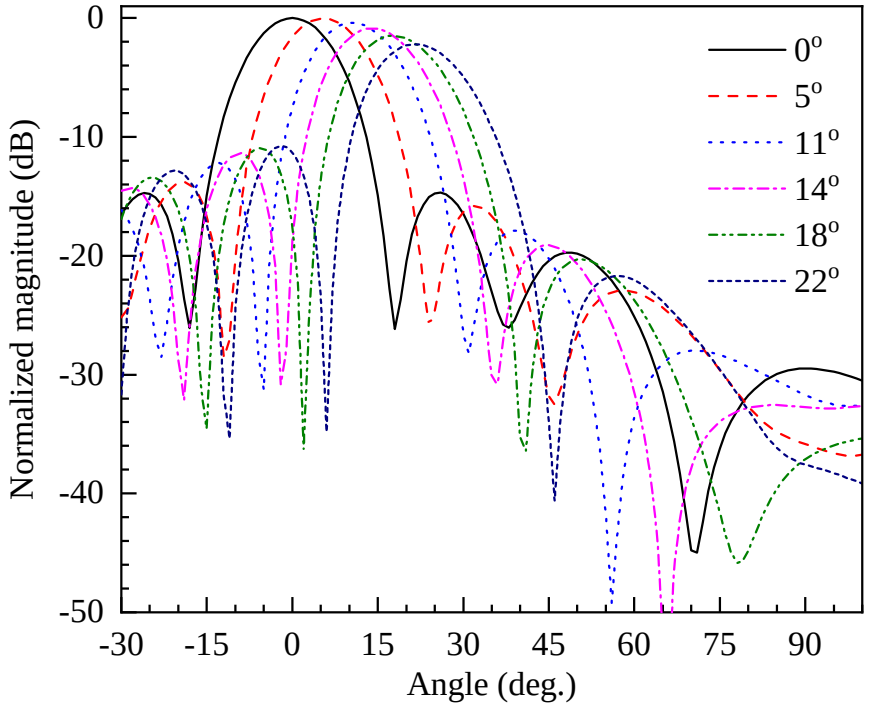

FIGURE 7.20: Measured beam steering results of a 4-element slotted waveguide array antenna (SWAA) system

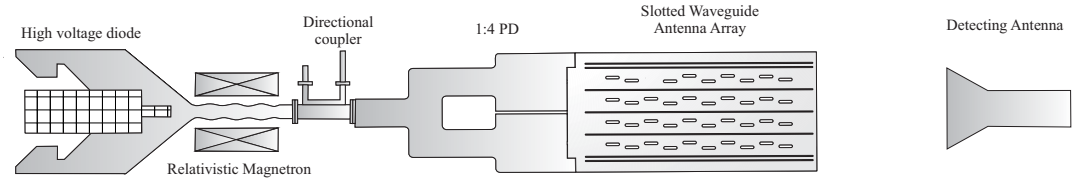

FIGURE 7.21: High power microwave test configuration of an array antenna

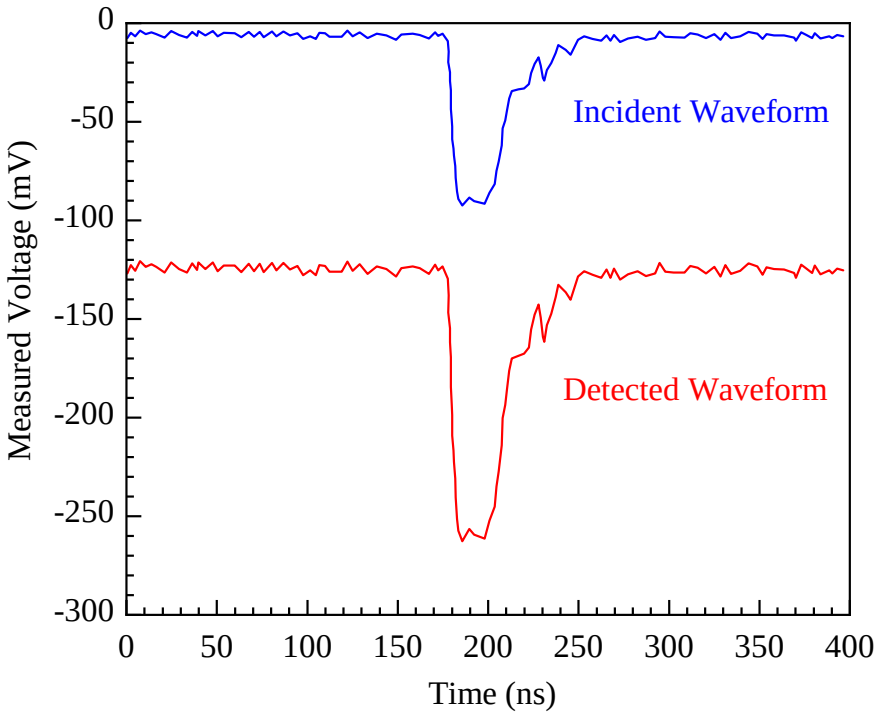

FIGURE 7.22: Incident and detected waveforms of an HPM test using the configuration shown in Fig. 7.21

the measured steered beam patterns are shown in Fig. 7.20. By simultaneously observing the data of Fig. 7.11(a) and Fig. 7.20, one can comfortably conclude that the observed and simulated data are in good harmony, which demonstrates the proof of concept.

In order to perform a high power microwave test to analyze power handling capacity of the SWAA, a setup was developed as shown in Fig. 7.21. The SWAA was covered with the radome filled with SF_6. The relativistic magnetron was used to generate 1.2 GW pulses for an output frequency of 3.0 GHz with pulse repetition rate of 10 Hz. The directional coupler was used before the antenna array to measure the incident waveform. On the other hand, a detector antenna was used to measure the radiated waveform in the far field region, as shown in Fig.

TABLE 7.5: Comparison of high power S-Band microwave antenna

Ref.	f_0 (GHz)	Dimensions (mm^2)	Aperture efficiency(%)	SLL (dB)	Gain (dBi)	Power
[149]	3.17	416×34.04	50.25	-10	9.91	1.15 MW
[124]	3.15	1204×1215	43.5	–	27.70	500 kW
[102]	3.40	500×72	48.4	-15	14.5	–
[150]	2.40	350×740	60	-21	21.64	–
[98]	3.95	480×515	53.33	-22	24.60	6.25 MW
This work	3.00	846×430	63	-15	24.60	1.06 GW

7.21. By examining the incident and the detected waveforms (Fig. 7.22), it can be concluded that there is no pulse shortening and that the two measured results had the same forms, which confirms that the system has the capacity to handle energy of at least 1.2 GW in S-band.

7.4 Summary

In this chapter, a slotted waveguide array antenna (SWAA) is developed for high-power microwave (HPM) applications in S-band. The array is developed by employing four slotted waveguide antenna of identical nature. The electromagnetic modeling was performed in CST MWS. The developed SWAA contained 4 elements, each has 10 rounded-edged leaky slots fabricated on the broad-side wall of an S-band waveguide. The array was designed at a central frequency of 3 GHz with power handling capacity greater than 1.0 GW. Slots of the array were distributed in a Gaussian profile to improve gain and to reduce side lobe levels (SLLs). In a four elements array each set of radiating slots are separated by a grooved line to reduce mutual coupling by controlling surface current. At the outer shoulder of the waveguide two additional grooves were fabricated to improve the radiation characteristics of the array. The designed SWAA was energized using a 1×4 power divider (PD) by ensuring equal power division with identical phase at each output port of the PD. To make the system robust and consistent, a dielectric radome is

also designed and tested. A complete fabricated system is then characterized in an anechoic chamber with and without radome. The results so obtained were compared with the simulated data to demonstrate the validity of the design. Return loss of -25.5 dB at $f_0 = 3$ GHz is obtained when the system is measured without radome, whereas its value is 24.46 dB with radome. Experimentally, observed E and H planes radiation patterns showed a good degree of consistency with the simulated data. The fabricated system exhibited a gain of 24.11 dBi at 3.00 GHz whereas, the simulated data represented a gain of 24.55 dBi at 2.99 GHz. Additionally, SLL magnitude less than -20 dB in H-plane with no significant back and side lobes are observed. The developed technique exhibited a 7% increase in gain when compared with conventional (un-grooved) SWA. This enhancement in gain is associated with reduced mutual coupling using inside grooves and by employing Gaussian distribution in slots placement. The proposed technology exhibited a maximum of 33% reduction in mutual coupling in-between array elements when compared with the conventional design. The array provided $\pm 22^\circ$ beam steering with a nominal gain reduction of 2.2 dBi. The developed technique can be used in high-power microwave applications wherein its power handling capabilities can be adjusted as per the need of an application by inducing an appropriate ambient inside the radome.

Chapter 8

Conclusion and Future Work

8.1 Conclusion

High-power microwave (HPM) technology has become popular for both civilian and military applications. There are many HPM devices and systems in the world, such as active denial systems that are used as a non-lethal system for the benefit of a society. The HPM system investigated in this dissertation consists of:

1. Microwaves pulse compression (MPC);
2. Waveguide based GW antenna design and development;
3. Realization of four element GW array antenna.

In order to enhance RF peak power, a microwave pulse compression technique has been employed using an RF polarizer. The output of the RF polarizer is fed into the storage cavity. Different types of RF storage cavities are used to store the RF energy. These storage cavity types include, but are not limited to: rectangular cavity and spherical shape cavity. The basic problem with rectangular cavity is that it can store RF energy of short duration, for longer pulse storage, the size of rectangular cavity becomes very large in terms of wavelength. On the other hand, the spherical cavity also offers storage of longer RF pulse duration, as well

as, high perturbation Q-factor which play very vital role for efficiently storing of RF energy in the cavity. (Chapter 3)

Dual circular RF polarizer-based pulse compressor uses a single spherical cavity for charging low power RF. The fundamental concept behind the discharge is the phase reversal of 180°, at the input side, at a particular instant in time. A novel technique to discharge the cavity, based on changing the stroke length of the polarizer with a plunger, is proposed. The general scattering matrix of an S-band (3 GHz) dual circular RF polarizer is developed by simulating it in the CST Microwave Studio. An aluminum prototype polarizer is fabricated and cold tested with a vector network analyzer (VNA). Experimental results exhibited a good agreement with the simulated data, hence, validating the proposed concept. (Chapter 4)

Experimental validation of RF-plasma interaction behaviors for the purposes of wave transmission and reflection, was also carried out in this research. Wave reflection from plasma is of interest as it finds applications in pulse compression and RF polarizer-based systems. Simulations were performed using a combination of Magic3D and COMSOL Multiphysics to characterize the plasma-wave interaction and discharge tube properties. The goal was to generate plasma with characteristics that wholly reflect the incident electromagnetic wave. A glass tube of inner diameter 22 mm and length 100 mm, with 12 mm brass electrodes, was fabricated for plasma generation. Argon-based DC glow discharge was sustained at 500 volts at a pressure of 3.8 Torr. Plasma density was calculated to be $2.529 \times 10^{19}\mathrm{m}^{-3}$, with a corresponding plasma frequency of 7.18 GHz. Due to this higher frequency, a 3 GHz incident RF wave was reflected, as measured through S-parameter measurements using a network analyzer. Off and on states of the tube correspond to $S_{11} = -40$ dB and $S_{11} = -13$ dB, which show wave transmission and reflection, respectively. When the plasma column was ignited, the reflected wave had a phase difference of 180°. (Chapter 5)

For transmission, an efficient slotted waveguide antenna (SWA) system was designed for S-band HPM applications. The designed SWA comprised of 10-slot

elements placed on the broad-side wall of the waveguide having dimensions a = 72.136 mm and b = 34.036 mm loaded with two inside-grooves, and a Gaussian dielectric radome made from high density polyethylene (HDPE) material. The inside-grooves were introduced to suppress the surface current of the waveguide, which resulted in a relatively high gain and reduced side lobe level (SLL). The modified Gaussian slots distribution controls the SLLs, and the unique Gaussian profile shape radome offered constant radiation characteristics. The proposed antenna system, within existing size constraints, offers a high gain of 20.1 dBi in conjunction with a high-power handling capability of greater than 100 MW. The designed SWA system had compact dimensions of $8.46\lambda_0 \times 1.38\lambda_0 \times 1.50\lambda_0$, with SLLs of -20 dB and -22 dB in the H$-$ and E$-$plane, respectively. The HPM antenna system, radiating at 3 GHz, is fabricated on aluminum material using the milling process. The simulated SWA system has good agreement with measured results. Moreover, the proposed SWA system offered clear advantages in terms of its robustness, design simplicity, high power handling capability, and high gain. (Chapter 6)

To improve the gain of the antenna further and to achieve beam scanning capabilities, the work is extended and a slotted waveguide array antenna (SWAA) was developed for HPM applications in S-band. The array was developed by employing four slotted waveguide antenna of identical nature. The electromagnetic modeling was performed in CST MWS. The developed SWAA contained four elements, each has 10 rounded-edged leaky slots fabricated on the broad side-wall of an S-band waveguide. The array was designed at $f_0 = 3$ GHz with power handling capacity greater than 1.0 GW. In a four elements array each set of radiating slots were separated by a grooved line to reduce mutual coupling by controlling surface current. At the outer shoulders of the waveguide, two additional grooves were fabricated to improve the radiation characteristics of the array. The designed SWAA was energized using a 1×4 power divider (PD) by ensuring equal power division with identical phase at each output port of the PD. To make the system robust and consistent, a dielectric radome was also designed and tested.

A complete fabricated system was then characterized in an anechoic chamber, both with and without a radome. The results so obtained were compared with the simulated data to demonstrate the validity of the design. Return loss of -25.5 dB at $f_0 = 3$ GHz was obtained when the system was measured without radome, whereas its value was 24.46 dB with radome. Experimentally, observed E and H planes radiation patterns showed a good degree of consistency with the simulated data. The fabricated system exhibited a gain of 24.11 dBi at 3.00 GHz whereas, the simulated data represented a gain of 24.55 dBi at 2.99 GHz. Additionally, SLL magnitude less than -20 dB in H-plane with no significant back and side lobes are observed. The developed technique exhibited a 7% increase in gain when compared with conventional (un-grooved) SWA. This enhancement in gain is associated with reduced mutual coupling using inside grooves and by employing Gaussian distribution in slots placement. The proposed technology exhibited a maximum of 33% reduction in mutual coupling in-between array elements when compared with the conventional design. The array provided $\pm 22^\circ$ beam steering with a nominal gain reduction of 2.2 dBi. The developed technique can be used in high-power microwave applications wherein its power handling capabilities can be adjusted as per the need of an application by inducing an appropriate ambient inside the radome. (Chapter 7)

8.2 Future Work

The current research can be extended further into following possible areas:

1. The MPC design may be improved by employing a Relativistic Magnetron of more than 1.0 GW and of relatively longer pulse duration. Such an HPM device could possibly radiate 3 to 5 times enhanced power, thus, eliminating the need of high voltage supply/generator.

2. The existing design of plasma based switch may be replaced, after appropriate research, with a more efficient switch based on laser triggering mechanism. In this way the output of MPC may be improved considerably; since, its efficiency is mainly determined by the response time of the switch.

3. The spherical cavity for RF storage may be replaced by a corrugated rectangular cavity having high $Q-$factor and more storage to accommodate longer pulses. Now a day's new research has been conducted on corrugated rectangular cavity for RF storage to achieve high peak RF power. It offers almost equal $Q-$factor but with more compactness compared to spherical cavity. However, the design robustness is still to be investigated.

4. The design of slotted waveguide array antenna may be extended to achieve higher directive (40 dBi) with efficient 1×48 power divider to feed the array configuration. Additionally, the impact of Gaussian radome requires further investigation and experimental support to assess precisely the breakdown field under various ambient conditions. An optimum environment for various applications may be determined for target electrical parameters.

5. In the designed array, the observed beam scanning was $\pm 22^{\circ}$. To improve the scanning area by maintaining the gain of the array, further investigation on the developed design would be a beneficial extension, which could potentially be employed in high power RADAR technology.

6. Due to the shortage of time, the associated phase shifter which is an integral part of the entire design, could not be realized. It is therefore, proposed that the work may be extended involving design and implementation of an efficient phase shifter.

Bibliography

[1] E. Schamiloglu, "High power microwave sources andapplications," *Microwave Symposium Digest, 2004 IEEEMTT-S International*, vol. 2, pp. 1001–1004, 2004.

[2] R. J. Barker and E. Schamiloglu, *High power microwave sources and technologies*. Wiley-IEEE Press, 2001.

[3] A. D. R. P. S. V. Samsonov, V. L. Bratman, G. Burt, G. G. Denisov, A. W. Cross, K. Ronald, W. He, and H. Yin, "Compression of frequency-modulated pulses using helically corrugated waveguides and its potential for generating multigigawatt RF radiation," *Physical Review Letters*, vol. 92, no. 11, 2004.

[4] A. B. K. Simonov, I. Golenitskiy, A. Mamontov, A. Yunakov, and O. Morozov, "Principles for design of high power pulsed microwavedevices and devices with low operating voltage foraccelerators," in *5th International Particle Accelerator Conference*, IPAC2014. Dresden, Germany: JACoW Publishing, 2014.

[5] Z. D. Farkas, H. A. Hogg, G. A. Leow, and P. B. Wilson, "SLED: A method of doubling SLAC's energy," in *Proceedings of 9th International Conference on High EnergyAccelerators*, 1974, p. 576.

[6] P. B. Wilson, Z. D. Farkas, and R. D. Ruth, in *Proceedings of the 22^{n}d 1990 LINAC Conference*, . IEEE, New York, Ed., Albuquerque, NM, 1990.

[7] D. Farkas, "Binary peak power multiplier and its applicationto linear accelerator design," *IEEE Trans. Microwave Theory Tech.*, vol. 34, p. 1036, 1986.

[8] R. J. Vidmar, "On the use of atmospheric pressure plasmas as electromagnetic reflectors and absorbers," *IEEE Transactions on Plasma Science*, vol. 18, no. 4, pp. 733–741, 1990.

[9] M. Laroussi and J. R. Roth, "Numerical calculation of the reflection, absorption, and transmission of microwaves by a nonuniform plasma slab," *IEEE Transactions on Plasma Science*, vol. 21, no. 4, pp. 366–372, 1993.

[10] W. Shen, J. E. Scharer, N. T. Lam, B. G. Porter, and K. L. Kelly, "Properties of a vacuum ultraviolet laser created plasma sheet for a microwave reflector," *Journal of applied Physics*, vol. 78, no. 12, pp. 6974–6979, 1995.

[11] C. Yeh and W. Rusch, "Interaction of microwaves with an inhomogeneous and anisotropic plasma column," *Journal of Applied Physics*, vol. 36, no. 7, pp. 2302–2306, 1965.

[12] Y. Zhang, X. He, J. Chen, Y. Chen, X. Zeng, X. Ni, J. Lu, and Z. Shen, "Experimental and numerical investigations on microwave absorption by the cold collisional capacity-coupled-plasma," *IEEE Transactions on Plasma Science*, vol. 42, no. 9, pp. 2253–2258, 2014.

[13] M. Moisan, J. Hubert, J. Margot, G. Sauvé, and Z. Zakrzewski, *Microwave Discharge: Fundamentals and Applications*. New York: Plenum, 1992.

[14] A. Al-Shamma'a, S. Wylie, J. Lucas, and C. Pau, "Design and construction of a 2.45 GHz waveguide-based microwave plasma jet at atmospheric pressure for material processing," *Journal of Physics D: Applied Physics*, vol. 34, no. 18, p. 2734, 2001.

[15] Y. C. Hong and H. S. Uhm, "Abatement of CF_4 by atmospheric-pressure microwave plasma torch," *Physics of Plasmas*, vol. 10, no. 8, pp. 3410–3414, 2003.

[16] Y. Kabouzi, D. B. Graves, E. Castanos-Martinez, and M. Moisan, "Modeling of atmospheric-pressure plasma columns sustained by surface waves," *Phys.*

Rev. E, Stat. Phys. Plasmas Fluids Relat. Interdiscip. Top, vol. 75, no. 1, pp. 016 402–1–016 402–14, Jan. 2007.

[17] H. Nowakowska, M. Jasi'nski, and J. Mizeraczyk, "Modelling of discharge in a high-flow microwave plasma source (MPS)," *Eur. Phys. J. D*, vol. 67, no. 7, pp. 133–1–133–8, Jul. 2013.

[18] P. Deng, W. Xiao, F. Wang, and Z. Zhang, "Design of a novel microwave plasma source based on ridged waveguide," *Progress In Electromagnetics Research Letters*, vol. 101, pp. 19–27, 2021.

[19] H. B. Joshi, N. R. Babu, A. Gahlaut, R. Kumar, and A. R. Tanna, "A computer modelling and its partial experimental validation to study the attenuation of electromagnetic waves in plasma using CST microwave studio," *Journal of Plasma Physics*, vol. 96, no. 1, pp. 1–8, 2022.

[20] S. Y. Moona and W. Choeb, "Parametric study of atmospheric pressure microwave-induced Ar/O_2 plasmas and the ambient air effect on the plasma," *Physics of Plasmas*, vol. 13, p. 103503, 2006.

[21] W. Zhang, L. Wu, K. Huang, and J. Tao, "Propagating modes of the travelling wave in a microwave plasma torch with metallic enclosure," *Phys. Plasmas 26*, no. 042101, 2019.

[22] T. Farouk, B. Farouk, D. Staack, A. Gutsol, and A. Fridman, "Simulation of DC atmospheric pressureargon micro glow-discharge," *Plasma Sources Sci. Technol.*, vol. 15, pp. 676–688, 2006.

[23] A. A. Garamoon, A. Samir, F. F. Elakshar, and E. F. Kotp, "Electrical characteristics of a DC glow discharge," *Plasma Sources Science and Technology*, vol. 12, pp. 417–420, 2003.

[24] J. T. Gudmundsson and A. Hecimovic, "Foundations of DC plasma sources," *Plasma Sources Science and Technology*, vol. 26, no. 12, p. 123001, 2017.

[25] P. Mathew, J. George, T. Sajith Mathews, and P. J. Kurian, "Experimental verification of modified Paschen's law in DC glow discharge Argon plasma," *AIP Advances 9*, vol. 025215, pp. 1–5, 2019.

[26] O. Goossens, T. Callebaut, Y. Akishev, A. Napartovich, N. Trushkin, and C. Leys, "The DC glow discharge at atmospheric pressure," *IEEE Transactions On Plasma Science*, vol. 30, no. 1, 2002.

[27] Z. Machala, E. Marode, C. O. Laux, and C. H. Kruger, "DC glow discharges in atmospheric pressure air," *Journal of Advanced Oxidation Technologies*, vol. 7, no. 2, 2004.

[28] J.-P. Boeuf, "A two-dimensional model of DC glow discharges," *Journal of applied physics*, vol. 63, no. 5, pp. 1342–1349, 1988.

[29] A. Derzsi, P. Hartmann, I. Korolov, J. Karacsony, G. Ban, and Z. Donk, "On the accuracy and limitations of fluid models of the cathode region of DC glow discharges," *Journal Of Physics: Applied Physics*, vol. 42, p. 225204, 2009.

[30] T. Kimura, K. Akatsuka, and K. Ohe, "Experimental and theoretical investigations of DC glow dischargesin Argon-Nitrogen mixtures," *Phys. D Appl. Phys.*, vol. 27, pp. 1664–1671, 1994.

[31] S. N. Artemenko, S. A. Gorev, and V. S. Igumnov, "High-power microwave pulse compressors with a variable geometry of accumulative resonant cavity," *IEEE*, 2016.

[32] M. McStravick, S. V. Samsonov, K. Ronald, S. V. Mishakin, W. He, G. G. Denisov, C. G. Whyte, V. L. Bratman, A. W. Cross, A. R. Young, P. MacInnes, W. Robertson, and A. D. R. Phelps, "Experimental results on microwave pulse compression using helically corrugated waveguide," *Journal of Applied Physics*, p. 054908, 2010.

[33] L. Zhang and *et al.* , "Experimental study of microwave pulse compressionusing a five-fold helically corrugated waveguide," *IEEE Trans. Microw.Theory Techn.*, vol. 63, no. 3, pp. 1090–1096, 2015.

[34] G. Shu, F. Zhao, N. Song, J. Zhang, M. Hou, S. Pei, and X. Zhang, "Design, fabricate and cold test of a C-band barrel opencavity pulse compressor," in *Proceedings of IPAC2017*, Copenhagen, Denmark, 2017.

[35] B. Woolley, I. Syratchev, and A. Dexter, "Control and performance improvements of a pulse compressor in use for testing accelerating structures at high power," *Physical Review Accelerators and Beams*, vol. 20, no. 10, p. 101001, 2017.

[36] P. J. B. Clarricoats and A. D. Olver, *Corrugated horns for microwave antennas*. IET, 1984, no. 18.

[37] G. Burt and *et al.* , "Microwave pulse compression using a helically corrugated waveguide," *IEEE Trans. Plasma Sci.*, vol. 33, no. 2, pp. 661–667, 2005.

[38] Y. Jiang and *et al.* , "Design and measurement of the X-band pulse compressor for TTX," *Key Laboratory of Particle and Radiation Imaging of Ministry of Education*, pp. 7–10, 2018.

[39] Y. Jiang, H. Zha, P. Wang, J. Shi, H. Chen, W. L. Millar, and I. Syratchev, "Demonstration of a cavity-based pulse compression system for pulse shape correction," *Physical Review Accelerators and Beams*, vol. 22, no. 8, p. 082001, 2019.

[40] Z. B. Drikas, B. D. Addissie, V. M. Mendez, and S. Raman, "A compact, high-gain, high-power, ultrawideband microwave pulse compressor using time-reversal techniques," *IEEE Transactions on Microwave Theory and Techniques*, vol. 68, no. 8, pp. 3355–3367, 2020.

[41] Y. Jiang, H. Zha, J. Shi, M. Peng, X. Lin, and H. Chen, "A compact x-band microwave pulse compressor using a corrugated cylindrical cavity," *IEEE Transactions on Microwave Theory and Techniques*, vol. 69, no. 3, pp. 1586–1593, 2021.

[42] Z. Zhang, D. Gao, and H. Gao, "Design and analysis of high-gain over-moded microwave pulse compression system," 2023.

[43] C. Chang and *et al.* , "Design and experiments of the GW high-power microwave feed horn," *Progress In Electromagnetics Research*, 2010.

[44] H. M. E. Misilmani, M. Al-Husseini, K. Y. Kabalan1, and A. El-Hajj, "Improved Vlasov antenna with curved cuts for high power microwaves," in *HPC Sim.*, 2013.

[45] A. Godard, L. Desrumaux, V. Bertrand, J. Andrieu, M. Lalande, B. Jecko, V. Couderc, M. Brishoual, and R. Guillerey, "A transient UWB antenna array used with complex impedance surfaces," *International Journal of Antennas and Propagation*, vol. 2010, no. 243145, 2010.

[46] L. Yu, C. Yuan, J. He, X. Zhao, Y. Sun, and C. Shen, "Design of a slot-coupled radial line helical array antenna for high power microwave applications," *AIP Advances*, vol. 7, no. 095101, 2017.

[47] S. Peng, C.-W. Yuan, T. Shu, J. Ju, and Q. Zhang, "Design of a concentric array radial line slotantenna for high-power microwave application," *IEEE Transactions On Plasma Science*, vol. 43, no. 10, 2015.

[48] S. B. Pottier, F. Hamm, D. Jousse, P. Sirot, F. T. Talom, and R. Vézinet, "High pulsed power compact antenna for high-power microwaves applications," *IEEE Transactions On Plasma Science*, vol. 42, no. 6, 2014.

[49] C.-W. Yuan, S.-R. Peng, T. Shu, Z.-Q. Li, and H. Wang, "Designs and experiments of a novel radial line slot antenna for high-power microwave application," *IEEE Transactions On Antennas And Propagation*, vol. 61, no. 10, 2013.

[50] L. Guo, W. Huang, C. Chang, J. Li, Y. Liu, and R. Meng, "Studies of a leaky-wave phased array antennafor high-power microwave applications," *IEEE Transactions On Plasma Science*, 2016.

[51] J. Li, W. Huang, T. Liang, H. Huang, and K. Wang, "Design and simulation of X-band HPM antenna based on leaky waveguide," *High Power Laser And Particle Beams*, vol. 23, no. 8, 2011.

[52] A. Kaur, "Electronically steerable planer phased array antenna," *International Journal of Engineering Trends and Technology*, vol. 3, no. 6, 2012.

[53] A.Chauloux, F. Colombel, M.Himdi, J. L. Lasserre, P. Bruguiere, P. Pouliguen, and P. Potier, "High gain and low losses antenna array for high power microwave applications," in *The 8th European Conference on Antennas and Propagation (EuCAP 2014)*, 2014.

[54] S. S. Saleem, M. M. Ahmed, U. Rafique, and U. F. Ahmed, "Optimization of linear antenna array for low SLL and high directivity," *IEEE*, 2016.

[55] X.-Q. Li, Q.-X. Liu, J.-Q. Zhang, and L. Zhao, "16-element single-layer rectangular radial line helical array antenna for high-power applications," *IEEE Antennas And Wireless Propagation Letters*, vol. 9, 2010.

[56] X. Zhao, C. Yuan, L. Liu, S. Peng, Q. Zhang, L. Yu, and Y. Sun, "All-metal beam steering lens antenna for high power microwave applications," *IEEE Transactions On Antennas And Propagation*, vol. 65, no. 12, 2017.

[57] Y. Yang, C. Yuan, and B. Qian, "A beam steering antenna for X-band high power applications," *AEU-International Journal of Electronics and Communications*, vol. 68, no. 8, pp. 763–766, 2014.

[58] X.-Q. Li, Q.-X. Liu, X.-J. Wu, L. Zhao, J.-Q. Zhang, and Z.-Q. Zhang, "A GW level high-power radial line helical array antenna," *IEEE Transactions On Antennas And Propagation*, vol. 56, no. 9, 2008.

[59] H. Arai, "Radial line slot antennas," *Handbook of Antenna Technologies*, 2015.

[60] L.-Z. Yu, C.-W. Yuan, J.-T. He, and Q. Zhang, "Beam steerable array antenna based on rectangular waveguide for high-power microwave applications," *IEEE Transactions On Plasma Science*, 2018.

[61] M. Al-Husseini, A. El-Hajj, and K. Y. Kabalan, "High-gain S-band slotted waveguide antenna arrays with elliptical slots and low sidelobe levels," in *Progress In Electromagnetics Research Symposium Proceedings*, 2013.

[62] R. Meng, Y. Xia, Y. Guo, and Q. Zhu, "An X-band 48-way leaky waveguide antenna with high aperture efficiency and high power capacity," *IEEE Transactions on Antennas and Propagation*, 2018.

[63] L. Yong, M. Fanbao, X. Gang, X. Ping, and M. Hongge, "Analysis of wide-angle scanning of HPM waveguide slot array antenna," *High Power Laser And Particle Beams*, vol. 30, no. 3, 2018.

[64] G. A. Casula, G. Mazzarella, G. Montisci, and G. Muntoni, "A review on improved design techniques for high performance planar waveguide slot arrays," *Electronics*, vol. 10, p. 1311, 2021.

[65] C. Huang, Z. Zhao, Q. Feng, C. Wang, and X. Luo, "Grooves-assisted surface wave modulation in two-slot array for mutual coupling reductionand gain enhancement," *IEEE Antennas And Wireless Propagation Letters*, 2009.

[66] E. C. V. Boas, R. Mittra, and A. C. S. Jr., "A low-profile high-gain slotted waveguide antenna array with grooved-structures," *IEEE Antennas And Wireless Propagation Letters*, 2020.

[67] J. W. Wang, S. G. Tantawi, C. Xu, M. Franzi, P. Krejcik, G. Bowden, S. Condamoor, Y. Ding, V. Dolgashev, J. Eichner *et al.*, "Development for a supercompact X-band pulse compression system and its application at SLAC," *Physical Review Accelerators and Beams*, vol. 20, no. 11, p. 110401, 2017.

[68] Y. Jiang, J. Shi, P. Wang, H. Zha, Z. Wang, X. Wu, H. Chen, C. Cheng, and W. Gai, "Design and measurement of the X-band pulse compressor for TTX," in *Proceedings of the 9th International Particle Accelerator Conference*, 2018, pp. 4745–4748.

[69] M. Franzi, J. Wang, V. Dolgashev, and S. Tantawi, "Compact RF polarizer and its application to pulse compression systems," *Physical Review Accelerators and Beams*, vol. 19, no. 6, p. 062002, 2016.

[70] J. Lei, X. He, G.-X. Pei, M. Hou, H. Wang, and J.-B. Zhao, "Design and cold test of an S-band waveguide dual circular polarizer," *Radiation Detection Technology and Methods*, vol. 1, no. 2, pp. 1–7, 2017.

[71] H. Sattari, T. Graziosi, M. Kiss, T. J. Seok, S. Han, M. C. Wu, and N. Quack, "Silicon photonic MEMS phase-shifter," *Optics Express*, vol. 27, no. 13, pp. 18 959–18 969, 2019.

[72] F. Guo, Y. Zhang, J. Lin, J. Kong, S. Zhu, Z. Lai, and Z. Zhu, "MEMS phase shifters on low-resistivity silicon wafer," in *2006 International Conference on Mechatronics and Automation*. IEEE, 2006, pp. 497–501.

[73] P. Romano, O. Araromi, S. Rosset, H. Shea, and J. Perruisseau-Carrier, "Tunable millimeter-wave phase shifter based on dielectric elastomer actuation," *Applied Physics Letters*, vol. 104, no. 2, p. 024104, 2014.

[74] A. Nikitin, A. Ustinov, A. Semenov, and B. Kalinikos, "A microwave phase shifter based on a planar ferrite-ferroelectric thin-film structure," *Technical Physics Letters*, vol. 40, no. 4, pp. 277–279, 2014.

[75] P. Wang, J. Shi, H. Zha, D. Cao, M. Peng, Z. Liu, C. Cheng, and H. Chen, "Development of an S-band spherical pulse compressor," *Nuclear Instruments and Methods in Physics Research Section A: Accelerators, Spectrometers, Detectors and Associated Equipment*, vol. 901, pp. 84–91, 2018.

[76] J. Lei, X. He, M. Hou, G. Shu, G.-X. Pei, X.-P. Li, and H. Wang, "Rf design of an s-band spherical cavity pulse compressor," *Radiation Detection Technology and Methods*, vol. 1, no. 2, p. 16, 2017.

[77] C. Chang, L. Guo, S. G. Tantawi, Y. Liu, J. Li, C. Chen, and W. Huang, "A new compact high-power microwave phase shifter," *IEEE Transactions on Microwave Theory and Techniques*, vol. 63, no. 6, pp. 1875–1882, 2015.

[78] O. Karsli, M. Dogan, F. Ahiska, and O. O. Surel, "Implementation of high power microwave pulse compressor," *IEEE Transactions on Plasma Science*, vol. 47, no. 6, pp. 2823–2831, 2019.

[79] S. K. Somayajula, A. T. Sriram, and V. M. Shelar, "Study of Argon and Xenon gas properties on DC-glow discharge plasma," *First International Conference on Advances in Physical Sciences and Materials*, no. 1706(2020)012030, 2020.

[80] W. Benstâali and A. Belasri, "Discharge efficiency improvement in PDP cell via a 1-D PIC/MCC method," *IEEE Transactions on Plasma Science*, vol. 39, no. 6, pp. 1460–1465, 2011.

[81] B. Chiad, T. Al-Zubaydi, M. Khalaf, and A. Khudiar, "Construction and characterization of a low pressure plasma reactor using DC glow discharge," *Journal of Optoelectronics and Biomedical Materials*, vol. 1, no. 3, pp. 255–262, 2009.

[82] M. S. Omran, S. Mirzanejhad, H. Zakeri-Khatir, and F. Sohbatzadeh, "Pressure and gas type effects on the plasma limiter operation at the s-band," *Brazilian Journal of Physics*, vol. 52, no. 5, p. 165, 2022.

[83] P. Ghosh and B. Chaudhury, "A novel self-aware dynamic mesh refinement technique for plasma fluid simulations of microwave breakdown," in *2022 IEEE International Conference on Plasma Science (ICOPS)*. IEEE, 2022, pp. 1–1.

[84] V. Anitha, P. Rathod, A. Patel, U. Goswami, V. Patel, and A. Vyas, "Confinement of washer-gun plasma and tailoring of location and scale length of electron density gradient to meet the requisites of microwave plasma interaction," in *2022 IEEE International Conference on Plasma Science (ICOPS)*. IEEE, 2022, pp. 1–2.

[85] M. Desai, P. Ghosh, A. Kumar, and B. Chaudhury, "Deep-learning architecture-based approach for 2-d-simulation of microwave plasma interaction," *IEEE Transactions on Microwave Theory and Techniques*, vol. 70, no. 12, pp. 5359–5368, 2022.

[86] K. Wilson, P. MacInnes, C. Whyte, L. Selman, A. Young, A. Phelps, A. Cross, L. Zhang, B. Eliasson, D. Speirs *et al.*, "Development of a plasma experiment and microwave sources for wave-plasma interaction experiments," in *2020 IEEE International Conference on Plasma Science (ICOPS)*. IEEE, 2020, pp. 602–602.

[87] J. Yao, Z. Yu, C. Yuan, Z. Zhou, X. Wang, and A. Kudryavtsev, "The influence of plasma distribution on microwave reflection in a plasma-metal model," *IEEE Transactions on Plasma Science*, vol. 48, no. 2, pp. 359–363, 2019.

[88] Y. Cao, J. Leopold, Y. P. Bliokh, A. Li, G. Shafir, A. Fisher, G. Leibovitch, V. Rostov, and Y. E. Krasik, "The interaction of a high-power subnanosecond microwave pulse with plasma," *IEEE Transactions on Plasma Science*, vol. 48, no. 4, pp. 792–801, 2019.

[89] Y. Cao, Y. Bliokh, J. Leopold, G. Leibovich, and Y. Krasik, "Verifying the wakefield induced by an ultra-high-power microwave sub-nanosecond pulse in a plasma filled waveguide, with a probing electron beam," in *2022 IEEE International Conference on Plasma Science (ICOPS)*. IEEE, 2022, pp. 1–1.

[90] A. Piel, *Plasma physics: an introduction to laboratory, space, and fusion plasmas*. Springer, 2017.

[91] V. Lisovskiy, V. Koval, E. Artushenko, and V. Yegorenkov, "Validating the Goldstein–Wehner law for the stratified positive column of DC discharge in an undergraduate laboratory," *European journal of physics*, vol. 33, no. 6, p. 1537, 2012.

[92] Ö. Şahin, I. Tapan, E. N. Özmutlu, and R. Veenhof, "Penning transfer in Argon-based gas mixtures," *Journal of Instrumentation*, vol. 5, no. 05, p. P05002, 2010.

[93] N. S. Frolov, S. A. Kurkin, A. A. Koronovskii, A. E. Hramov, and A. O. Rak, "High efficiency virtual cathode oscillator with photonic crystal," *Applied Physics Letters*, vol. 113, no. 2, p. 023503, 2018.

[94] A. E. Dubinov, S. K. Saikov, and V. P. Tarakanov, "Multivircator as a new highly effective microwave generator with multiple virtual cathodes: Concept and PIC-simulation," *IEEE Transactions on Plasma Science*, vol. 48, no. 1, pp. 141–145, 2019.

[95] S. Mumtaz, H. Uhm, J. S. Lim, and E. H. Choi, "Output-power enhancement of vircator based on second virtual cathode formed by wall charge on a dielectric reflector," *IEEE Transactions on Electron Devices*, vol. 69, no. 4, pp. 2043–2050, 2022.

[96] S. Mumtaz and E. H. Choi, "An efficient vircator with high output power and less drifting electron loss by forming multivirtual cathodes," *IEEE Electron Device Letters*, vol. 43, no. 10, pp. 1756–1759, 2022.

[97] L. Josefsson and S. R. Rengarajan, *Slotted waveguide array antennas: theory, analysis and design.* SciTech Publishing, India, 2018.

[98] H. M. El Misilmani, M. Al-Husseini, and K. Y. Kabalan, "Design procedure for planar slotted waveguide antenna arrays with controllable sidelobe level ratio for high power microwave applications," *Engineering Reports*, vol. 2, no. 10, p. e12255, 2020.

[99] D.-J. Kim and J.-H. Lee, "Compact resonant slot array antenna using partial H-plane waveguide," *IEEE Antennas and Wireless Propagation Letters*, vol. 9, pp. 530–533, 2010.

[100] S. Sekretarov and D. M. Vavriv, "A wideband slotted waveguide antenna array for SAR systems," *Progress in electromagnetics research M*, vol. 11, pp. 165–176, 2010.

[101] M. Al-Husseini, A. El-Hajj, and K. Kabalan, "High-gain S-band slotted waveguide antenna arrays with elliptical slots and low sidelobe levels," *Progress In Electromagnetics Research*, vol. 1821, 2013.

[102] H. M. El Misilmani, M. Al-Husseini, and M. Mervat, "Design of slotted waveguide antennas with low sidelobes for high power microwave applications," *Progress In Electromagnetics Research C*, vol. 56, pp. 15–28, 2015.

[103] G. A. Casula, G. Mazzarella, G. Montisci, and G. Muntoni, "A review on improved design techniques for high performance planar waveguide slot arrays," *Electronics*, vol. 10, no. 11, p. 1311, 2021.

[104] S. Ebadi and A. Semnani, "Mutual coupling reduction in waveguide-slot-array antennas using electromagnetic bandgap (EBG) structures," *IEEE Antennas and Propagation Magazine*, vol. 56, no. 3, pp. 68–79, 2014.

[105] T. Shaw, D. Bhattacharjee, and D. Mitra, "Gain enhancement of slot antenna using zero-index metamaterial superstrate," *International Journal of RF and Microwave Computer-Aided Engineering*, vol. 27, no. 4, p. e21078, 2017.

[106] M. Ghorbani and H. Ghorbaninejad, "Design of a high gain bandwidth improved aperture antenna using a frequency selective surface," *The Applied Computational Electromagnetics Society Journal (ACES)*, pp. 318–324, 2017.

[107] M. W. Niaz, Y. Yin, S. Zheng, and Z. Zhao, "Dual-polarized low sidelobe Fabry-Perot antenna using tapered partially reflective surface," *International Journal of RF and Microwave Computer-Aided Engineering*, vol. 30, no. 3, p. e22070, 2020.

[108] C. Huang, Z. Zhao, Q. Feng, and X. Luo, "A high-gain antenna consisting of two slot elements with a space larger than a wavelength," *IEEE Antennas and Wireless Propagation Letters*, vol. 9, pp. 159–162, 2010.

[109] A. Sutinjo and M. Okoniewski, "A simple leaky-wave analysis of 1-D grooved metal structure for enhanced microwave radiation," *IEEE Transactions on Antennas and Propagation*, vol. 60, no. 6, pp. 2719–2726, 2012.

[110] M. Beruete, I. Campillo, J. Dolado, J. Rodríguez-Seco, E. Perea, and M. Sorolla, "Enhanced microwave transmission and beaming using a subwavelength slot in corrugated plate," *IEEE Antennas and Wireless Propagation Letters*, vol. 3, no. 16, pp. 328–331, 2004.

[111] C. Huang, Z. Zhao, and X. Luo, "The rectangular waveguide board wall slot array antenna integrated with one dimensional sub-wavelength periodic corrugated grooves and artificially soft surface structure," *Journal of Infrared, Millimeter, and Terahertz Waves*, vol. 30, no. 4, pp. 357–366, 2009.

[112] B. El Jaafari and J.-M. Floch, "Gain enhancement of slot antenna using grooved structure and FSS layer," *Progress in Electromagnetics Research Letters*, vol. 65, pp. 1–7, 2017.

[113] C. Huang, C. Du, and X. Luo, "A waveguide slit array antenna fabricated with subwavelength periodic grooves," *Applied Physics Letters*, vol. 91, no. 14, p. 143512, 2007.

[114] C. Huang, Z. Zhao, Q. Feng, C. Wang, and X. Luo, "Grooves-assisted surface wave modulation in two-slot array for mutual coupling reduction and gain enhancement," *IEEE Antennas and Wireless Propagation Letters*, vol. 8, pp. 912–915, 2009.

[115] M. Khosronejad and G. G. Gentili, "Beam-width and gain enhancement of horn antennas," in *2016 17th International Symposium on Antenna Technology and Applied Electromagnetics (ANTEM)*. IEEE, 2016, pp. 1–2.

[116] K. Anim, H. A. Diawuo, and Y.-B. Jung, "Compact slotted waveguide antenna array using staircase model of tapered dielectric-inset guide for shipboard marine RADAR," *Sensors*, vol. 21, no. 14, p. 4745, 2021.

[117] W. He, Q. Xie, C. Liu, Q. Ding, and Y. Zhang, "A stratified radome design for millimeter wave antennas," in *2020 IEEE Asia-Pacific Microwave Conference (APMC)*. IEEE, 2020, pp. 953–955.

[118] J. L. Volakis, *Antenna engineering handbook*. McGraw-Hill Education, 2007.

[119] W. Coburn, M. Litz, J. Miletta, N. Tesny, L. Dilks, and B. King, "A slotted-waveguide array for high-power microwave transmission," Army Research Lab Adelphi MD, Tech. Rep., 2001.

[120] H. El Misilmani, M. Al-Husseini, K. Y. Kabalan, and A. El-Hajj, "A design procedure for slotted waveguide antennas with specified sidelobe levels," in *2014 International Conference on High Performance Computing & Simulation (HPCS)*. IEEE, 2014, pp. 828–832.

[121] H. M. E. Misilmani, M. Al-Husseini, K. Y. Kabalan, and A. El-Hajj, "A design procedure for slotted waveguide antennas with specified sidelobe levels," *HPC Sim*, 2014.

[122] C. E. Baum, "Sidewall waveguide slot antenna for high power," *Sensor and Simulation Notes, Note*, vol. 503, 2005.

[123] A. Stevenson, "Theory of slots in rectangular waveguides," *Journal of Applied physics*, vol. 19, no. 1, pp. 24–38, 1948.

[124] C. Martel, "A rectangular slotted waveguide array for high power microwave applications," in *2020 IEEE International Symposium on Antennas and Propagation and North American Radio Science Meeting*. IEEE, 2020, pp. 343–344.

[125] A. E. Elmerie, "Filled slotted waveguide antennas," 2021.

[126] K.-L. Hung and H.-T. Chou, "A design of slotted waveguide antenna array operated at X-band," in *2010 IEEE International Conference on Wireless Information Technology and Systems*, 2010, pp. 1–4.

[127] G. Deschamps, "Ray techniques in electromagnetics," *Proceedings of the IEEE*, vol. 60, no. 9, pp. 1022–1035, 1972.

[128] S.-W. Lee, P. Cramer, K. Woo, and Y. Rahmat-Samii, "Diffraction by an arbitrary subreflector: GTD solution," *IEEE Transactions on Antennas and Propagation*, vol. 27, no. 3, pp. 305–316, 1979.

[129] S.-W. Lee, M. Sheshadri, V. Jamnejad, and R. Mittra, "Wave transmission through a spherical dielectric shell," *IEEE Transactions on Antennas and Propagation*, vol. 30, no. 3, pp. 373–380, 1982.

[130] R. J. Barker and E. Schamiloglu, *High-power microwave sources and technologies*. Wiley-IEEE Press, 2001.

[131] J. Benford, J. A. Swegle, and E. Schamiloglu, *High power microwaves*. CRC press, 2015.

[132] Y. Tyagi, P. Mevada, S. Chakrabarty, and R. Jyoti, "High-efficiency broadband slotted waveguide array antenna," *IET Microwaves, Antennas & Propagation*, vol. 11, no. 10, pp. 1401–1408, 2017.

[133] C. Chang, X. Zhu, G. Liu, J. Fang, R. Xiao, C. Chen, H. Shao, J. Li, H. Huang, Q. Zhang *et al.*, "Design and experiments of the GW high-power microwave feed horn," *Progress In Electromagnetics Research*, vol. 101, pp. 157–171, 2010.

[134] L. Guo, W. Huang, C. Chang, J. Li, Y. Liu, and R. Meng, "Studies of a leaky-wave phased array antenna for high-power microwave applications," *IEEE Transactions on Plasma Science*, vol. 44, no. 10, pp. 2366–2375, 2016.

[135] L. Yong, M. Fanbao, X. Gang, X. Ping, and M. Hongge, "Analysis of wide-angle scanning of HPM waveguide slot array antenna," *High Power Laser and Particle Beams*, vol. 30, no. 03, p. 033002, 2018.

[136] L.-Z. Yu, C.-W. Yuan, J.-T. He, and Q. Zhang, "Beam steerable array antenna based on rectangular waveguide for high-power microwave applications," *IEEE Transactions on Plasma science*, vol. 47, no. 1, pp. 535–541, 2018.

[137] X.-Q. Li, Q.-X. Liu, J.-Q. Zhang, and L. Zhao, "16-element single-layer rectangular radial line helical array antenna for high-power applications," *IEEE Antennas and Wireless Propagation Letters*, vol. 9, pp. 708–711, 2010.

[138] A. M. Khan, M. M. Ahmed, U. Rafique, A. Kiyani, and S. M. Abbas, "An efficient slotted waveguide antenna system integrated with inside-grooves and modified gaussian slot distribution," *Electronics*, vol. 11, no. 18, p. 2948, 2022.

[139] E. C. V. Boas, R. Mittra, and A. C. Sodre, "A low-profile high-gain slotted waveguide antenna array with grooved structures," *IEEE Antennas and Wireless Propagation Letters*, vol. 19, no. 12, pp. 2107–2111, 2020.

[140] R. Meng, Y. Xia, Y. Guo, and Q. Zhu, "An X-band 48-way leaky waveguide antenna with high aperture efficiency and high power capacity," *IEEE Transactions on Antennas and Propagation*, vol. 66, no. 12, pp. 6799–6809, 2018.

[141] G. A. Deschamps, "Ray techniques in electromagnetics," *Proceedings of the IEEE*, vol. 60, no. 9, pp. 1022–1035, 1972.

[142] S.-W. Lee, M. Sheshadri, V. Jamnejad, and R. Mittra, "Wave transmission through a spherical dielectric shell," *IEEE Transactions on Antennas and Propagation*, vol. 30, no. 3, pp. 373–380, 1982.

[143] G. Montisci, Z. Jin, M. Li, H. Yang, G. A. Casula, G. Mazzarella, and A. Fanti, "Design of multi-layer dielectric cover to enhance gain and efficiency of slot arrays," *International Journal of Antennas and Propagation*, vol. 2013, 2013.

[144] T. Djerafi, A. Patrovsky, K. Wu, and S. O. Tatu, "Recombinant waveguide power divider," *IEEE transactions on microwave theory and techniques*, vol. 61, no. 11, pp. 3884–3891, 2013.

[145] R. Meng, H. Zhang, B. Muneer, and Q. Zhu, "The design of a 48-way high power capacity sectorial waveguide power divider," in *2014 IEEE Antennas and Propagation Society International Symposium (APSURSI)*. IEEE, 2014, pp. 643–644.

[146] X. He, M. Hou, J.-R. Zhang, and Y.-L. Chi, "Development of four kinds of waveguide power divider for S-band," *arXiv preprint arXiv:1607.02816*, 2016.

[147] X. Zhao, C. Yuan, L. Liu, S. Peng, Q. Zhang, L. Yu, and Y. Sun, "All-metal beam steering lens antenna for high power microwave applications," *IEEE Transactions on Antennas and Propagation*, vol. 65, no. 12, pp. 7340–7344, 2017.

[148] Y.-W. Wu, Z.-C. Hao, Z.-W. Miao, W. Hong, and J.-S. Hong, "A 140 GHz high-efficiency slotted waveguide antenna using a low-loss feeding network," *IEEE Antennas and Wireless Propagation Letters*, vol. 19, no. 1, pp. 94–98, 2019.

[149] X. Pan, C. G. Christodoulou, J. Lawrance, J. McConaha, and M. Landavazo, "Cold & hot tests of an S-band antenna for high power microwave systems," in *2017 IEEE International Symposium on Antennas and Propagation & USNC/URSI National Radio Science Meeting*. IEEE, 2017, pp. 627–628.

[150] S. I. Alhuwaimel and K.-F. Tong, "Stacked S-band slotted waveguide array antenna with very low sidelobes," in *2017 International Workshop on Electromagnetics: Applications and Student Innovation Competition*. IEEE, 2017, pp. 116–118.